Study of collective cell durotaxis as an active wetting phenomenon

Macià Esteve Pallares Pallares

STUDY OF COLLECTIVE CELL DUROTAXIS AS AN ACTIVE WETTING PHENOMENON

Macià Esteve Pallares Pallares
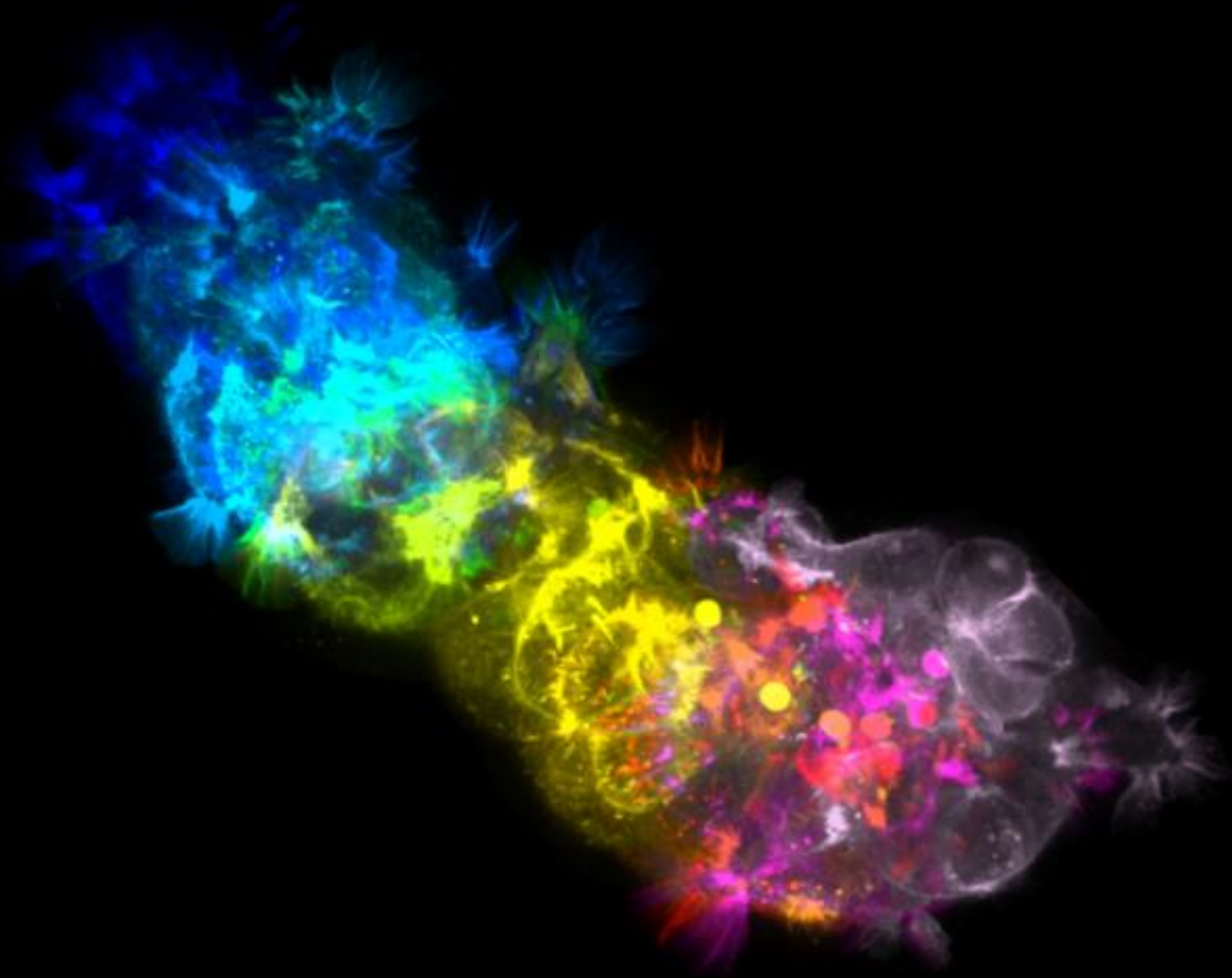
Barcelona, December 2021

Study of collective cell durotaxis
as an active wetting phenomenon

Memòria per optar al grau de Doctor en el Programa de Doctorat en Biomedicina

Institut de Bioenginyeria de Catalunya (IBEC)

Universitat de Barcelona (UB)

Desembre de 2021

Presentada per:

Supervisada per:

Macià Esteve Pallares Pallares
(Autor)

Dr. Xavier Trepat Guixer
(Co-director i tutor)

Dr. Raimon Sunyer Borrell
(Co-director)

A la meva mare i al meu pare,

per a qui la meva educació sempre ha sigut una prioritat

Agraïments

Sou molts els que m'heu ajudat en algun moment durant aquests durs 5 anys de doctorat: alguns m'heu ensenyat tècniques experimentals que no dominava, d'altres m'heu explicat conceptes que no entenia o inclús m'heu dotat d'uns mínims de coneixements en programació. A banda de l'expertesa i saviesa que m'emporto, el suport emocional que tots m'heu donat ha estat clau per no haver tirat la tovallola ni en els moments més difícils. Moltes gràcies de tot cor a tots, i disculpeu-me si no us incloc explícitament, ja que sou molts els que m'heu ajudat.

Xavi, això no hauria estat possible si no m'haguessis convidat a sol·licitar una beca doctoral al teu grup després d'haver-me donat el millor dels seminaris del màster. T'estaré eternament agraït per l'oportunitat que em vas oferir. També us estic molt agraït que, juntament amb en Raimon, m'hagueu sabut guiar per aquest camí tan fosc que és la recerca. Sense els vostres enraonaments i consells hauria estat molt més difícil de trobar-hi la llum. Moltes gràcies de tot cor a tots dos. Pere, alguns dels millors moments del doctorat els he passat impartint classes de problemes i pràctiques de laboratori sota la teva supervisió a la UB. Moltes gràcies per haver confiat en mi, i també per totes les discussions i el feedback associat al projecte. Finalmente, esta tesis no hubiese sido posible sin la ayuda de Valeria Grazú y Bea Martínez, quienes me enseñaron a funcionalizar superficies carboxiladas con E-cadherina en el laboratorio de Jesús Martínez de la Fuente. Muchas gracias a todos!

Pare, mare, ja he acabat! Ho sento molt si en algun moment he estat desagradable degut a la frustració fruit d'aquesta etapa, o si he estat reaci a parlar-ne. El mateix et dic a tu, Guillem: perdona'm per haver-te fet suportar algun més d'un vespre de malhumor relacionat amb la tesi. Dit això, moltes gràcies per donar-me tot el suport incondicional, us estimo molt!

Gràcies també a tots els que em vau ensenyar com utilitzar els microscopis, com el Manu, l'Ariadna, el Raimon, l'Anna, l'Ernest, el Leone i la Amy. Gràcies a tots els que em vau ensenyar tècniques experimentals com el Juanfra, l'Annabel-Lise, la Natalia, la Xarxa, el Victor, el Carlos, i molts més. Irina, gràcies per haver-me explicat tan bé el model que tu, el Ricard i el Jaume heu desenvolupat, i per haver redactat l'annex 2 d'aquesta tesi. Isabela, thanks so much for taking care of the experiments studying the effect of increasing contractility. You are super efficient! I finalment, gràcies a tots per tots els cafès de discussió o de mer descans que eren clarament reparadors. Ariadna, tu has estat el meu pilar fonamental al laboratori a nivell emocional! Mil gràcies per aconsellar-me, ajudar-me i inclús renyar-me quan tocava! M'emporto una gran amistat.

Contents

1. **Introduction**

1. Preface

Cell migration is essential to many biological processes. In adult organisms, it is crucial for wound healing, homeostasis, and immune response, whereas aberrant cell migration potentially leads to pathology. For example, the onset of cell migration in cancer cells can lead to metastasis, where cancer cells escape from the primary tumour confinement, intravasate the blood vessels and circulate through the bloodstream to ultimately extravasate and colonize distant organs. In the context of development, processes such as morphogenesis and organogenesis occur because of cell migration: for an embryo to become an adult organism, cells migrate either as single cells or epithelial sheets to give rise to functional organs and recurrent tissue shapes in a very well-orchestrated and reproducible manner both in time and space. Given its relevance, the regulation mechanisms underlying cell locomotion are highly controlled both at a transcriptional, protein localization and functional level.

The study of cell migration from a biological perspective provided scientists with knowledge on key molecules, effector proteins and signalling pathways that play a crucial role during this process. However, with the emergence of the field of mechanobiology, the fact that physical parameters were no longer neglected shed light on the mechanics behind cell locomotion and enabled us to convey a more accurate idea of this extremely complex process. That is mainly because no matter which signalling cascade is triggered by whatever myriad of protein-ligand interaction driving cell migration, the end-result is a cell or a collective of cells translocating their bulk to a position different than the original one. Therefore, the simplest consideration of cell migration is a physical phenomenon where cells must be subjected to the most basic laws of physics. Consequently, to fully understand the complexities of cell migration, its study must be tackled both from the molecular biology and physical point of view.

In the introduction of this thesis, I will cover the mechanisms regulating cell migration from the molecular to the tissue level, focusing on collective cell migration and durotaxis, the ability of single cells and groups to follow mechanical cues. Next, I will review previous work tackling tissue spreading and migration as a wetting phenomenon, emphasizing on the active gel theory. Finally, although cell migration has been primarily studied when mediated by focal adhesions at the extracellular matrix (ECM) interface, important migratory processes during development or metastasis take place in contexts lacking ECM. Recent studies suggest that E-cadherin, a cell-cell adhesion protein essential to maintain tissue integrity, promote coordination and establish cell polarity, could govern cell migration in ECM-depleted environments. In the last section of this thesis, I will comment on the scarce cadherin-dependent cell migration events published to date, discussing the emerging role of E-cadherin in mediating cell migration.

2. Single cell migration

Individual cells migrate to specific locations within our bodies through a process called single cell migration. Cells integrate physical[1], chemical[2], or electrical external stimuli[3] to set a front-rear polarity that will ultimately define the direction of motion. In the absence of external clues, polarity arises randomly[4] and can either be maintained in highly persistent cell types[5] or change stochastically at short timescales in cell types displaying low persistence[6].

Essentially, two general types of single cell migration have been characterized: mesenchymal and ameboid migration[4,7]. The interplay between cell morphology, the tractions they exert and the adhesive interactions with their respective microenvironments dictates whether cells undergo one or the other characteristic migratory behaviour[8]. Despite the different migration mechanisms adopted by cells in motion, some general requirements need to be met: cell polarization, dynamic cytoskeletal reorganizations enabling adhesion to the substrate, and traction forces powered by cytoskeletal contractions represent the minimum ingredients for cell migration to effectively take place[8]. In all migratory events, the cytoskeleton is the ultimate cellular structure responsible for providing the cells with the ability to exert traction forces on the substrate to propel themselves. In the next section, I will review how the different cytoskeletal structures are able to regulate the motion of cells.

2.1 The cell cytoskeleton

The cell cytoskeleton is a complex 3D network composed of three different types of protein filaments: microtubules, actin filaments and intermediate filaments (Figure 1-1). The growth of cytoskeleton filaments is powered by the repetitive non-covalent assembly of small subunits of the different filaments stored in a cytoplasmic pool. The assembly and disassembly of cytoskeleton filaments is tightly regulated by a plethora of accessory proteins that not only bind the cytoskeleton filaments to specific cell components, but also bind them to one another, making the cytoskeleton a very adaptable and highly regulated structure at the global scale[9].

The cell cytoskeleton is crucial for many cellular processes such as cell division[10], organelle rearrangement within cells[11] and cell migration[12]. In this chapter, I will summarize the role of the cytoskeleton filaments in the context of cell migration.
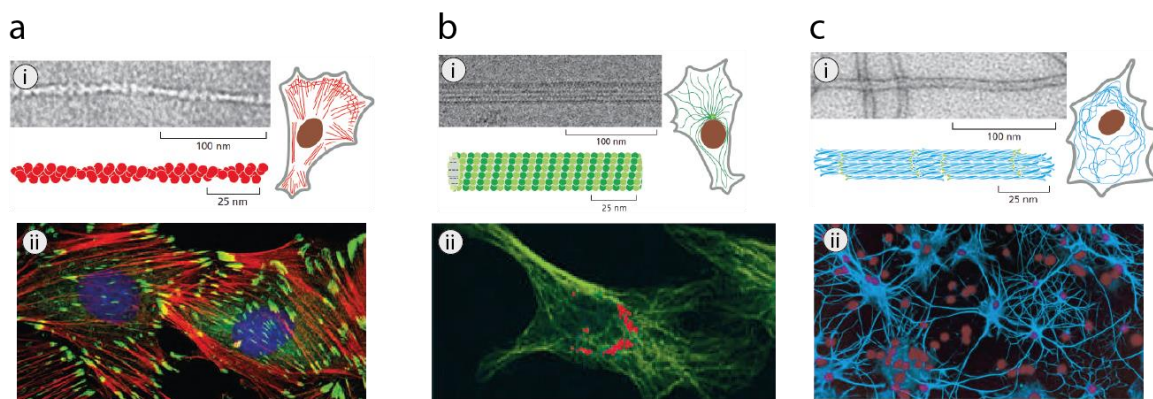
Figure 1-1. The cytoskeleton is composed by actin filaments, microtubules and intermediate filaments. (a) Monomers of G-actin polymerize into polar, helical actin filaments of 8 nm in diameter that organize into linear filaments (i), 2D networks or 3D gels formed beneath the plasma membrane, specializing in different functions. Stress fibers are contractile 1D actin bundles labelled in red in (ii). (b) Monomers of tubulin polymerize into long, hollow cylinders of an outer diameter of ~25nm (i) often with one end attached to a microtubule-organizing centre (MTOC). Microtubules (labelled in green in (ii)) display a radial organization within the cell. Organelles are labelled in red. (c) Intermediate filaments are built by the lateral assembly of octamers that organize forming rope-like filaments constituting the intermediate filament network (i). Intermediate filaments network in neurons is shown in (ii). Adapted from Alberts et al.[4]

Microtubules are structures made of α- and β-tubulin subunits that assemble into 13 parallel protofilaments forming hollow, cylindrical structures presenting a polarity, with the negative end of the filament anchored to the microtubules organization centre (MTOC), typically located near the cell nucleus. Microtubules constitute the tracks for long-distance intracellular transport of cargos carrying e.g. new membrane components, adhesion proteins and signalling molecules to the leading edge of a migrating cell, thus representing a crucial component for the establishment and maintenance of cell polarity[13]. The dynamics of assembly and disassembly of microtubules is controlled by Rho GTPases, which also control actin polymerization, myosin contractility and the local turnover of cellular adhesions, directly affecting cell polarity and thus their migratory outcome[14].

Intermediate filaments are rope-like structures forming a helical array built up by the lateral packing of octamers of intermediate filaments monomers. They present strain-hardening, meaning that they become stiffer with increasing strains[4], thus potentially providing cells with the required mechanical and structural support to bear the usually high strains built up in migrating cells. Intermediate filaments are responsible for regulating the formation of actin stress fibers and membrane protrusions mediated by p38[15] (a protein of the MAPK family). Five different types of intermediate filaments exist, each of which specialized in a different function and cellular localization. For example, lamins represent a type V intermediate filament and form a filamentous support inside the inner nuclear membrane, whereas keratins represent a type I-II intermediate filament and form junctions that either hold cells together at the desmosomes or anchor cells to the ECM through hemidesmosomes[16].

Actin monomers (G-actin) are soluble proteins stored in a cytoplasmic pool, whereas its ATP-dependent polymerization results in the formation of actin filaments (F-actin). Its diameter is approximately 8 nm, and they are composed of helical polymers formed by an ordered array of actin monomers assembled head-to-tail[4]. Because of their assembly dynamics, actin filaments are polarized and capable of generating force[17]. Even though their location is ubiquitous across the whole cytoplasm, there is an enrichment in actin filaments beneath the cell membrane, whose association with actin binding proteins (ABPs) and molecular motors constitutes the cell cortex[17].

On the one hand, ABPs modulate the dynamics of the cell cortex in many ways: different specialized ABPs induce actin polymerization, depolymerization, capping or branching. On the other hand, molecular motors such as myosin bind different actin filaments in the cell cortex and promote the sliding of filaments in an ATP-dependent manner, hence generating contractile stresses within the cell cortex[17].

Actin filaments are not found isolated within cells, but the complex regulation of actin filaments by ABPs and molecular motors allows for the formation of different supra-organization actin structures within the cytoplasm specialized in different mechanical functions (Figure 1-2). On the one hand, the 1D bundling of actin filaments gives rise to either stress fibers or filopodia; stress fibers are contractile due to their association with myosin motors and subjected to mechanical tension, whereas filopodia arise from a spike-like plasma membrane projection that cells use to probe and explore their surroundings[4,17]. On the other hand, a high degree of actin filament cross-linking gives rise to a gel-like network constituting the cell cortex, providing cells with the ability to mechanically adapt their components to exert forces modulating cell adhesion, changes in cell shape and cell migration[18]. Due to the contractile nature of actomyosin, a constant pulling force on actin filaments is exerted from the edge towards the centre of the cell, resulting in the typical actin retrograde flow[17,19]. This process

constitutes one of the minimum ingredients for cell migration to take place, as it allows for the generation of the traction forces that will ultimately propel cell migration.

Importantly, actin filaments play a fundamental role in mechanically coupling the actomyosin cytoskeleton both to other cells' cytoskeletons through cell-cell junctions, and to the extracellular matrix (ECM) through focal adhesion complexes[12] (FA).
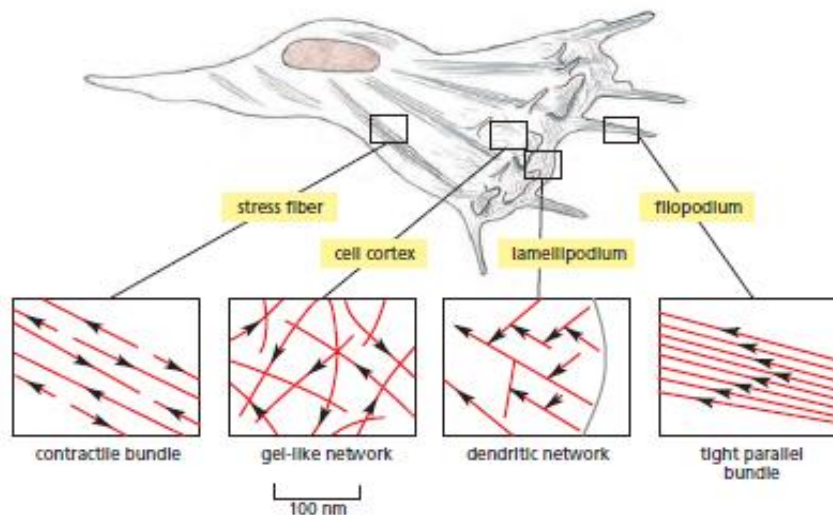
Figure 1-2. Actin structures during fibroblast crawling. Enlarged areas show different actin organization structures (actin is shown in red, where arrowheads point towards the minus end of the filament) that emerge during fibroblast migration. Stress fibers are contractile due to their association with myosin motors and are under tension. The cell cortex constitutes a gel-like or dendritic network that allows for the formation of specific membrane protrusions such as the lamellipodia. Filopodia allow cells to explore their environments through the formation of tight, parallel actin bundles. Adapted from Alberts et al.[4]

2.2. Cell-ECM adhesions

The pulling force resulting from the interplay between actin polymerization and myosin motors is transmitted to the extracellular environment through tension across stress fibers tethered to the attachment sites. This in turn promotes the maturation of those anchoring sites into focal adhesions (FA), which are very dynamic protein complexes whose main function is to mechanically couple the actin cytoskeleton of the cell to the ECM[20]. Focal adhesions are formed by heterodimers of α and β subunits of a family of transmembrane proteins called integrins, whose combination allows for adhesion on different ECM protein compositions[21]. Paxillin, talin and vinculin are part of the myriad of the so-called adaptor proteins that interact with the cytoplasmic domain of the integrin subunits, constituting FA complexes and thus allowing for the transmission of force from the cytoskeleton to the ECM. Therefore, adaptor proteins are under tension, which arises from the contractile forces exerted by the actomyosin cytoskeleton[22,23].

Mechanical signals found in the extracellular environment are integrated at the FA complexes and translated into biochemical intracellular signals, such as phosphorylation events that trigger the onset of signalling cascades or conformational changes that allow for additional protein interactions[24]. For example, the phosphorylation of the Y-118 tyrosine residue of paxillin in nascent adhesions generates interaction sites for the binding of SH2 domain-containing signalling proteins such as CRK, which in turn regulate paxillin localization to FA complexes in a feedback loop, thus promoting adhesion[25,26]. The integration of mechanical signals in cells is referred to as mechanosensing, whereas the term mechanotransduction refers to the activation of intracellular processes as a response to mechanical signals[27].
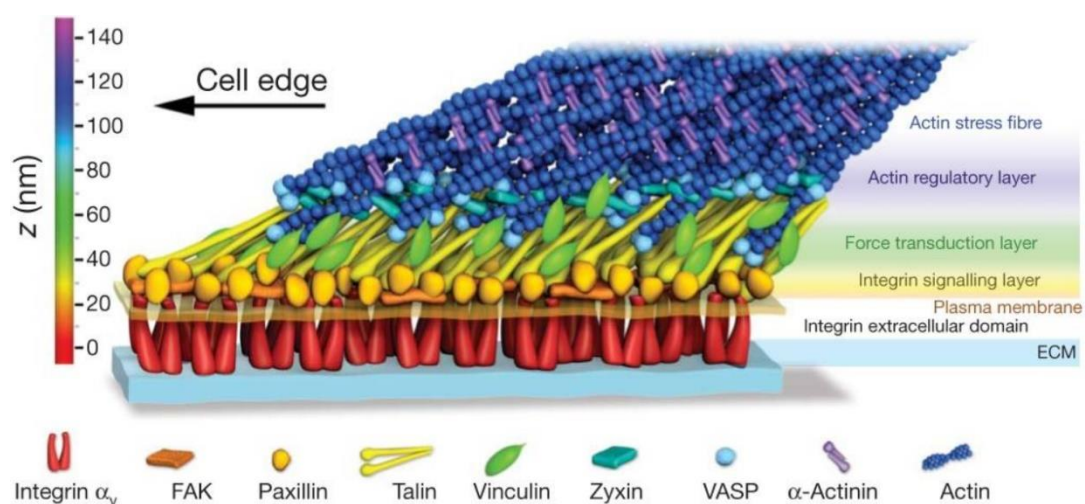
Figure 1-3. Cartoon illustrating the interactions between the ECM, integrins, adaptor proteins and actomyosin. ECM's resistance to deform results in the built-up of tension transmitted to actomyosin through mechanosensory adaptor proteins such as talin, which undergoes conformational changes enabling the recruitment of vinculin, triggering the further recruitment of additional actin filaments to FA complexes. Adapted from Kanchanawong et al.[28]

Some adaptor proteins at the FA complexes have been reported to display mechanosensitive features. Take talin as example: above a given tension threshold, talin undergoes conformational changes that result in the presentation of a previously cryptic vinculin binding site (VBS). Hence, above such tension threshold, an increased number of vinculin molecules are able to bind talin, and this in turn allows for an increased recruitment of actin filaments[22] (Figure 1-3). Other adaptor proteins at the cell-ECM interface have also been reported to play a role during cell mechanosensing; some include vinculin[29], zyxin[30,31], p130Cas[32], and actinin[23].

The phosphorylation and conformational changes experienced by mechanosensitive proteins at the FA complexes often enable the recruitment of additional proteins to the complexes, which in turn reinforces the adhesions and allows for the transmission of force generated by the actomyosin cytoskeleton to the ECM[22].

The dynamics of integrin adhesion to the ECM, ECM ligand density and substrate stiffness dictate the traction forces cells exert[33]. Different theoretical approaches have emerged to model cellular traction forces as a function of all the aforementioned parameters, which can be easily tuned to predict the evolution of traction forces in different environments for different cell lines and ECM ligands[34]. An example of such theoretical approaches is the molecular clutch model, which excels at predicting cell traction forces for different substrate stiffnesses and ligand spacings[22,33,35]. Below, I will briefly explain the generation of traction forces at the FA complexes according to the clutch model.

The molecular clutch model relies on a series of clutches that constantly engage and disengage the ECM at the FA complexes. As the actin cytoskeleton pulls on FA complexes with a given actin retrograde flow, integrins dynamically bind and unbind to ECM ligands with a certain K_{on}/K_{off} binding dynamics. The molecular clutch model predicts that FA complexes will cause large ECM deformations at low substrate stiffnesses that will not allow for fast force loading rates, as most of the integrin dimers (modelled as clutches) detach before significant forces are built up[22], resulting in the generation of low traction forces on low stiffness substrates. In contrast, FA complexes will yield very fast force loading rates at high stiffness substrates, leading to catastrophic FA disengagement events that will not allow cells to exert high tractions if talin unfolding is not considered. However, traction forces have been reported to increase with increasing substrate stiffness (Figure 1-4 a, b). This behaviour is explained by the clutch model by means of a reinforcement event triggered by talin unfolding, resulting in the maturation of FA, which is discussed below[35].

Firstly, integrin-ligand bindings form a catch bond whose stability increases with tensile force[36].
Secondly, FA complexes display mechanosensitive abilities that trigger mechanotransduction events:
as stated before, talin unfolds above a certain tension threshold, which is reached above a given
substrate stiffness value, resulting in the presentation of a previously cryptic Vinculin binding site
(VBS). This confers vinculin an increased affinity for FA complexes, ultimately triggering signalling
cascades that result in an increased recruitment of integrins, adaptor proteins and actin fibers at the
FA complexes. Therefore, talin unfolding enables a reinforcement of the cell-ECM adhesions, which
not only affects the size of the adhesions, but also enables the generation of larger traction forces
with increasing substrate stiffness[22] (Figure 1-4 c,d). Interestingly, abrogation of talin unfolding
resulted in the traction forces presenting a biphasic relationship with substrate stiffness, as predicted
by the molecular clutch model (Figure 1-4 a, b).

Figure 1-4. Talin unfolds upon a stiffness threshold increases force transmission, adhesion maturation and YAP nuclear translocation. (a) Cell traction showed a biphasic relationship with stiffness in Talin 2 shRNA or Talin 1 Head L325R conditions. Traction forces exerted by control cells increase with stiffness as a result of talin unfolding, which triggers the reinforcement of the adhesions. (b) Color-coded traction force maps showing the low generation of traction forces under Talin 2 shRNA or Talin 1 Head L325R conditions in 29 kPa gels. (c) Focal adhesion length increases in control cells above a stiffness threshold. (d) Representative examples of vinculin immunostainings in cells plated on 5 and 29 kPa under the different experimental conditions. (e) Nuclear/cytoplasmic YAP ratio increases in control cells above a stiffness threshold. (f) Representative examples of YAP immunostaining showing YAP nuclear translocation in control conditions on 29 kPa stiffness substrates. Adapted from Elosegui-Artola et al.[22]

In all, talin unfolding enables cell-ECM adhesions to bear fast force loading rates that would otherwise
result in the collapse of FA at high stiffness, ultimately explaining the increase of traction forces with
increasing substrate stiffness.

A recent study has unveiled the importance of ligand density on the generation of traction forces. On
substrates displaying large ligand spacings, individual FA must bear much higher traction forces than
for smaller ligand spacing due to a limited number of available ligands. Therefore, a third regime for
traction force generation was described, which is characterized by the collapse of FA on high stiffness

substrate and high ligand spacings, as the active reinforcement of FA is prevented by the inaccessibility of new integrin subunits to the ligands[33].

The study of the localization of YAP, a transcription factor involved in cell proliferation and apoptosis, has been historically used as a reporter of the reinforcement at the FA complexes. Briefly, the build-up of tension upon reinforcement at the FA complexes is transmitted to the nucleopores via the cell cytoskeleton[37]. As a response, the nucleopores undergo conformational changes that enable YAP to translocate form the cell cytoplasm to the cell nucleus. Therefore, a high nuclear to cytoplasmic ratio of YAP indicates reinforcement of the FA complexes[37] (Figure 1-4 e,f).

Besides explaining the generation of traction forces by single cells in varying ECM-coated substrate stiffness, the molecular clutch model can also model processes such as cell spreading or cell migration [38,39].
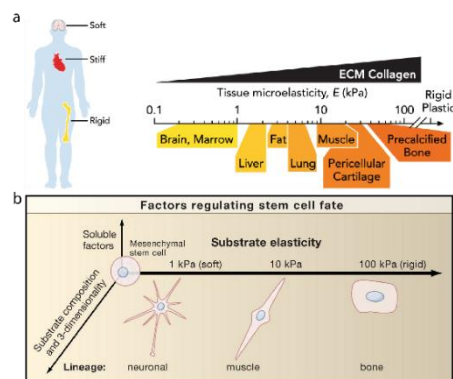
Figure 1-5. iPSC differentiation in response to substrate stiffness. (a) The physiological values of stiffness range from less than 0.5 kPa in brain tissues to over 60kPa in bones. (b) iPSC cultured on soft substrates differentiated into neurons, whereas differentiation to osteoblasts was promoted in rigid substrates. Thus, iPSC differentiated according to their native environment's stiffness. Adapted from R Smith et al.[43] and Even-Ram et al.[44]

Remarkably, cell migration did not necessarily require the generation of high traction forces or the establishment of strong cell-ECM adhesions in *in vitro* 2D research studies [40]. Thus, an important fraction of the total tractions exerted by cells is essential to maintain homeostasis and normal function by probing the mechanical properties of the surrounding tissues as well as integrating them in the FA complexes in order to modulate specific cellular outcomes. For example, ECM stiffness and thus traction force generation were found to be sufficient to impact on the fate of mesenchymal stem cells (MSCs). Interestingly, MSCs cultured on soft substrates (whose stiffness resembled physiological stiffness values of brain tissue) differentiated into brain cells, while MSCs cultured on rigid substrates (whose stiffness resembled that of osseous tissues) differentiated into osteoblasts[41] (Figure 1-5). Moreover, an increase in ECM stiffness was shown to be sufficient to trigger a malignant transformation in the breast[42].

Summing up, the mechanical properties found in the ECM represent cues of paramount importance for a very wide range of cellular processes. Importantly, cellular traction forces constitute the cornerstone of cell migration, arising from the interplay between actin polymerization, adhesion dynamics and cell contractility. This matter will be addressed in the next section.

2.3 Actin polymerization, adhesion dynamics and cell contractility regulate cell migration

As introduced in the previous section, cell migration arises from the interplay between actin polymerization, cell-ECM adhesion dynamics and cell contractility[45,46]. Together with myosin contractility, the cell membrane opposes to actin polymerization, prompting the generation of an actin retrograde flow from the cell periphery towards the cell body[19]. Under circumstances that do not allow for high adhesiveness such as soft or poorly coated substrates where cell-substrate force transmission is minimal, actin retrograde flow is fast. In contrast, on adhesive surfaces such as stiff or densely coated substrates, force transmission through FA slows down actin's retrograde flow[47]. The reduction in actin's retrograde flow, paralleled by further actin polymerization and branching promoted by ABPs, favours the formation of actin structures such as the lamellipodia and filopodia at the leading edge of cells[48]. Hence, slow actin retrograde flows result in the fast growth of actin protrusions, and consequently, actin retrograde flow and cell speed are inversely correlated[45]. Remarkably , the net actin polymerization is equivalent to the effective translocation of the cell body towards the leading edge.

The role of contractility in cell speed varies greatly depending on the adhesiveness of the substrate. On the one hand, myosin contractility enables traction force generation and thus favours integrin reinforcement and cell motility, but an excessive increase in contractility could result in the collapse of FAs and would be counterproductive for cell migration, as predicted by the molecular clutch model[35]. On the other hand, and also in line with the molecular clutch model predictions, below the stiffness threshold required for integrin reinforcement (and thus for virtually non-adhesive substrates), reducing contractility would result on a slower actin retrograde flow, providing the cells with the ability to exert higher force loading rates and thus ultimately favouring cell migration on those soft substrates[49]. Therefore, a tight interplay between cell contractility, actin polymerization and cell-substrate adhesion dynamics dictates the outcome of cell migration.

2.4 Directed cell migration

During single cell migration, cells acquire a front-rear polarity that can either arise randomly or be established by the presence of external gradients. The acquisition of a front-rear polarity is crucial to trigger the onset of migration in a wide range of biological processes including development[50–53] and homeostasis[54]. In front-rear polarized cells, a lamellipodia can generally be observed in the leading edge where nascent FA are formed, resulting in a decrease in the retrograde flow of actin, permitting the growth of membrane protrusions[55,56]. Behind the lamellipodia, long and stable stress fibers connect the front with the trailing edge. Consequently, the trailing edge is submitted to high tension, which favours cell retraction through the disassembly of FAs[55,56]. In all, the architecture of the cell cytoskeleton is different in both leading and trailing edges in polarized cells. Microtubules serve as railways through which cargos containing different proteins are transported across a cell ensuring the availability of those proteins in the target locations[4]. For example, cargos carrying membrane components and proteins involved in cell adhesion are brought to the leading edge. Therefore, microtubules ensure the maintenance of cell polarity by transcytosis events where "incorrectly"-localized membrane proteins are re-located to their "correct" position[14].

In the absence of external cues, cell migration generally follows a random pattern. Polarity is randomly acquired, and after some time, cells spontaneously re-polarize and the direction of migration changes[57]. Therefore, cells do not display a preferential migratory direction. The parameter "persistence" can be estimated experimentally in order to assess the directionality of cell migration, and it is defined as the quotient of the Euclidean distance into the total distance a cell migrates within a given time interval. Hence, it ranges from 0 to 1, where the closest to 1, the more directed motion cells exhibit[58]. While some cell types such as fish keratocytes tend to display a more directed motion over time and thus a higher persistence[5], other cell types such as fibroblasts re-polarize in multiple occasions at very short time scales in the absence of external gradients[6].

Alternatively, when external gradients are presented to cells, migration follows a directed motion towards or against such gradients. Many types of gradients have been found to be used as external cues to establish polarity, and thus to direct cell migration. Chemotaxis is a kind of directed cell migration event where cells follow external soluble biochemical gradients[2]; haptotaxis occurs when cells direct migrate in response to immobilized ligand density gradients[59]; the ability to direct migration towards or against an electric field is referred to as electrotaxis[3], whereas durotaxis refers to the preferential migration towards stiff regions in the presence of a gradient of stiffness[1], which will be reviewed in the next section.

2.5 Single cell durotaxis

In our work, we focus on the ability of cells to polarize and direct their migration following mechanical gradients. As mentioned above, this phenomenon is called durotaxis, which was named after the latin word *durus* (translated as "hard") and the Greek word *taxis*[60] (meaning "logical arrangement"). It was first used in the literature at the start of the 21st century by Lo et al.[61], after early studies demonstrated that mechanical stimuli could influence cell elongation[62], cell polarization[63] and cell migration[61]. Studies spanning the last 2 decades contributed to a better understanding of durotaxis *in vitro*[1,39,64,65], whereas recent research studies put *in vivo* durotaxis in the spotlight, suggesting that mechanical cues also guide cell migration during development[52,66,67], fibrosis[68] and cancer[42,69]. Whereas I will further discuss on relevant durotaxis examples in the following sections of the thesis, in this chapter I will focus on the proposed cellular mechanisms behind durotaxis.

Most knowledge on the mechanisms that drive durotaxis derives both from *in vitro* and *in silico* approaches[1,38,39,64,65,70]. Experimentally, the use of hydrogels coated with different ECM proteins provided scientists with the first notions on durotaxis. For example, fibroblasts seeded on gradients of stiffness presented durotaxis when the gradients were coated with fibronectin, but this phenomenology was abrogated in laminin-coated stiffness gradients[64], suggesting that fibronectin-mediated migration triggers mechanosensing mechanisms hindered during laminin-mediated migration. Therefore, the nature of the ligand affects the migratory outcome of cells.

Historically, the kind of hydrogels that were initially used to characterize durotaxis displayed isotropic mechanical properties, whereas the latter development of microfabrication and microfluidics techniques enabled the generation of anisotropic hydrogels displaying a stiffness gradient[39,65,71]. Both isotropic and anisotropic hydrogels provided insights into the rationale behind durotaxis, and to date, the mechanisms through which cells integrate mechanical stimuli to trigger a directed migratory behaviour have not been fully elucidated, and thus there are several proposed hypotheses to explain durotaxis. While some propose that the mechanical signal that triggers durotaxis is the absolute value of stiffness[63,72], others state that it is the slope of the gradient of stiffness[64,65,70,73]. To better understand these assumptions, it is important to focus on the experiments both carried out on uniform stiffness and on stiffness gradient hydrogels.
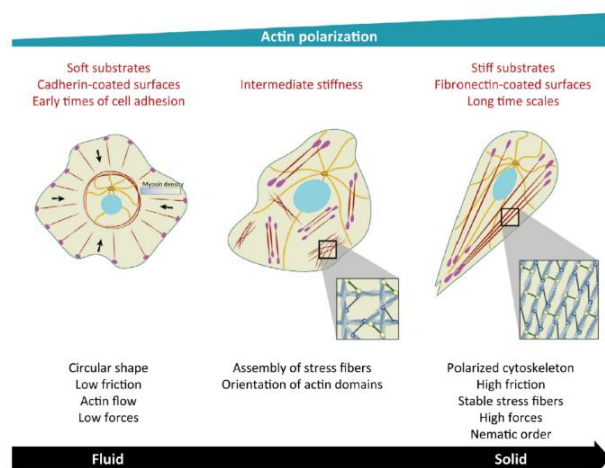
Figure 1-6. The cell rheology changes from a fluid-like to a solid-like with increasing stiffness as a consequence of a higher actin orientational order. Cells seeded on non-adhesive substrates display a circular shape with circumferential actin retrograde flow, displaying hallmarks of fluids. Cells seeded on intermediate stiffness substrates display stress fibers, whereas an orientational order of actin domains appear. Cells seeded on very adhesive substrates show a highly polarized actin cytoskeleton with stable stress fibers, displaying the hallmarks of a nematic order. Adapted from Ladoux et al.[56]

On the one hand, experiments performed on uniform stiffness gels showed that cells on stiff substrates of physiological ranges displayed increased velocity[74] and spreading area[75,76], compared to cells seeded on softer hydrogels. Additionally, it was also shown that the rheology of the cell cytoskeleton changes from fluid-like to solid-like with increasing stiffness[77], where an orientational order in the actin cytoskeleton emerges on stiff gels (Figure 1-6). Therefore, some scientists hypothesize that the absolute value of stiffness alone is enough to drive durotaxis, as migration of cells on a theoretical stiffness gradient would be biased towards the stiff edge by the increased speed and higher actin orientational order cells exhibit on stiffer gels[72,78].

On the other hand, work carried out on stiffness gradients showed that the slope of the gradient dictates to what extent cells durotax, yielding increased durotactic behaviours in steep stiffness gradients[39,64,65,70,73]. Mechanistically, the authors propose that the difference in stiffness between both cell edges (the absolute stiffness value on the soft edge versus the one on the stiff edge) is integrated by the cell cytoskeleton to promote tissue polarity towards the stiff edge. Such a polarity induction would be driven by an asymmetry on actin protrusion and FAs stability in both cell edges. On the stiff edge, higher force loading rates would result in higher FA stability, yielding slower actin retrograde flow and thus allowing for the formation of lamellipodial structures[47]. In contrast, the same traction forces exerted at the cell's soft edge would result in higher substrate deformations, favouring the collapse and decreased stability of FA, as well as faster actin retrograde flows[35,38]. This hypothesis was validated by Sunyer et al., whose work reported that cell monolayers covering higher differences in stiffness than single cells displayed an increased durotactic behaviour[39]. However, those experiments implied an additional degree of complexity, as they proved that the integration of mechanical signals during the migration of an epithelia happens at the supracellular level rather than at the cell level. In this case, a new kind of migratory behaviour typically referred to as collective cell migration (CCM) emerges, constituting the main subject of study of this thesis.

3. Collective cell migration

The collective migration of a group of cells is referred to as collective cell migration (CCM). Like single cells, collectives of cells guide their migration by sensing gradients of different types of cues such as electrical[79], chemical[80] or mechanical[39]. Interestingly, directed collective migration events are far more efficient than the migration of their isolated constituents[39], indicating that gradient sensing is enhanced during CCM[39]. Collective cell migration events are of paramount importance in many biological processes including homeostasis, pathology and development.

For example, homeostatic processes such as wound healing are enabled by an orchestrated collective migration of cells: epithelial tissue injury results in a discontinuity in the cell monolayer, triggering the cells on the edge to polarize towards the centre of the wound and collectively migrate towards it, ultimately terminating the discontinuity in the cell monolayer[81,82] (Figure 1-8).
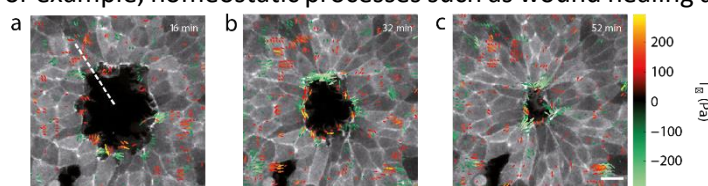
Figure 1-8. Traction forces during wound healing, where cells migrate collectively towards the centre of the wound. In order to illustrate the process of wound closure, three timepoints were represented (a,b,c). Adapted from Brugués et al.[81]

In pathological contexts such as cancer, metastasis occurs as a result of cancer cells escaping the confinement of the primary tumour, intravasating and extravasating the blood vessels to finally migrate towards a distant body tissue and colonize it[83] (Figure 1-7). Recent research on cancer biology concluded that, compared to single cancer cells infiltrating the blood vessels, infiltrated clusters of cancer cells display at least a 23-fold metastatic

Figure 1-7. A model for the multistep metastatic process. Briefly, cancer cells that escape the confinement of the primary tumor intravasate to blood vessels and flow within the bloodstream. Eventually, cancer cells extravasate, potentially resulting in a metastatic colonization in a distant organ. Adapted from Crownbio, Bourré[86].

potential[84,85], and thus generally represent a major threat compared to isolated migrating cancer cells.

More importantly, collective cell migration constitutes the cornerstone of development[87]. In order to give rise to a correct shape and function during morphogenesis and organogenesis, cells must undergo very drastic and well-orchestrated tissue rearrangements both in time and space within the embryo. For example, the lateral line primordium formation in zebrafish relies on the posterior caudal migration of a group of approximately 140 cells that are to give rise to neuromasts, which constitute sensory elements to detect water flow in fish and aquatic amphibians[88] (Figure 1-10). Another example of the paramount importance of CCM in development is in *D. melanogaster* oogenesis, during which a group of cells (named border cells) migrates from anterior to posterior of the egg to give rise to a functional oocyte[50].
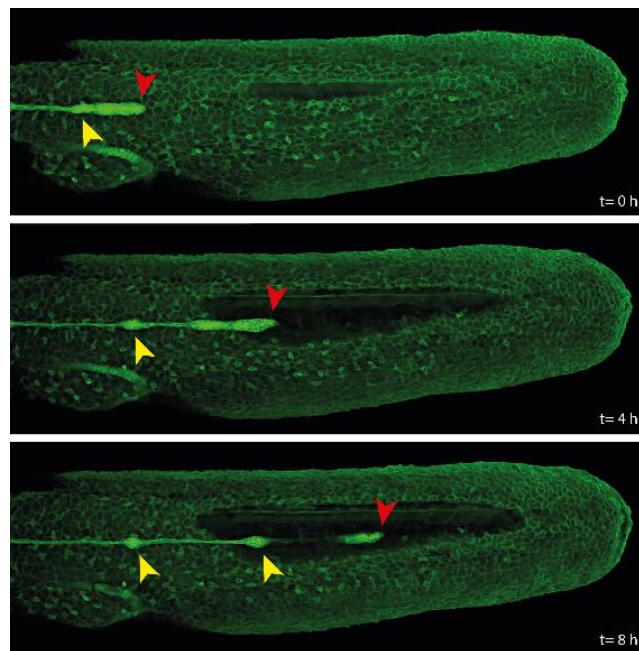
Figure 1-10. Lateral view with anterior to the left and ventral down of Zebrafish lateral line primordium migration. *The migrating lateral line primordium (red arrows) leaves behind clusters of cells that differentiate into neuromasts, constituting a crucial sensory element in fish and amphibians. Claudin B-GFP fusion protein represents cell membranes. Adapted from The Company of Biologists[89].*

As noted in the previous section, CCM entails an additional degree of complexity compared to single cell migration, since the integration of signals and the migratory outcome occurs at the supracellular level rather than the single cell level[39,90]. Therefore, collective migratory events require a tight coordination at the tissue level as well as the maintenance of tissue integrity, which are ultimately enabled by cell-cell junctions. In the next chapter, I will give an overview on the different types of cell-cell junctions focusing on the role of E-cadherin, a key component of adherens junctions, in the context of cell migration.

3.1 Cell-cell junctions

The appearance of a primitive version of the currently known E-cadherin protein occurred over 600 million years ago and enabled the emergence of multicellularity in metazoans[91]. Later on, around 525 million years ago, the origin of vertebrates was paralleled by a large increase in the number of genes encoding cadherins and other cadherin-interacting proteins[91]. Primitive versions of such proteins were submitted to evolutionary pressure and consequently evolved into the current variety of more than 100 cadherin and cadherin-related genes participating in different types of cell-cell junctions[92], each of which specialized in different processes (Figure 1-11).

For example, tight junctions are found in endothelia and epithelia and are crucial to separate different tissue compartments within multicellular organisms, behaving as selective gates controlling paracellular diffusion of ions and solutes[4,93]. Gap junctions are found quite ubiquitously throughout our bodies and act structurally like channels through which molecules, ions and electrical impulses pass, allowing for functions such as metabolical and electrical coupling between adjacent cells[4,94]. Desmosomes constitute one of the strongest types of structures at cell-cell junctions. Consequently, they are mostly found in tissues submitted to high mechanical stresses such as cardiac, bladder, and epithelial tissues[95], and their role is to mechanically couple the intermediate filament network of neighbouring cells through E-cadherin and desmoplakin[4,95].
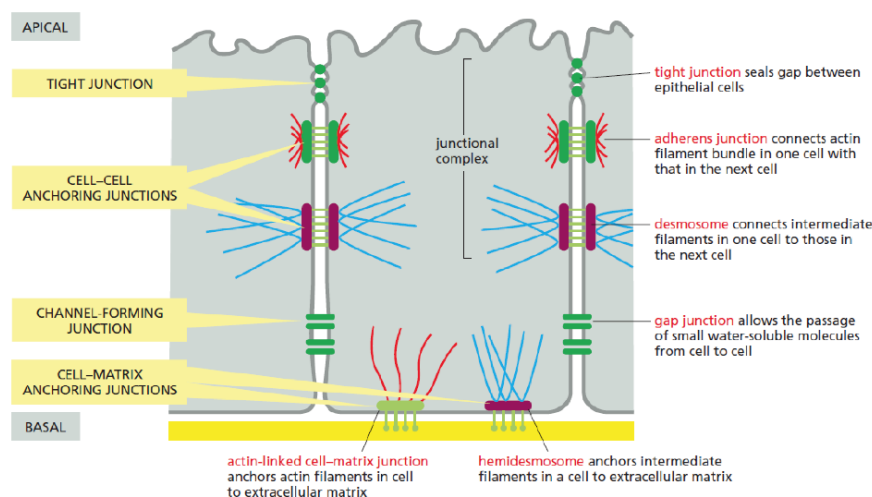
Figure 1-11. Cartoon depicting a summary of the various cell junctions found in a vertebrate epithelial cell. Typically, tight junctions localize apically. Below, adherens junctions connect the actomyosin cytoskeletons of neighboring cells, whereas desmosomes connect intermediate filaments of neighboring cells at medial positions. Gap junctions typically occupy basal positions in epithelial cells and act as channels that metabolically and electrically couple adjacent cells. Adapted from Alberts et al.[4]

Finally, adherens junctions are protein complexes formed by the interaction of E-cadherin molecules of adjacent cells that are in turn bound to the actin cytoskeleton through adaptor proteins[96], whose main function is thought to be related to the maintenance of tissue integrity[97]. Different structures of adherens junctions have been reported, which will be discussed below (Figure 1-12).

The term focal adherens junctions was proposed by Huveneers et al.[98], serving to describe nascent adherens junctions in epithelia and endothelia. Upon cell-cell contact, E-cadherin molecules in adjacent cells form a punctate pattern and align perpendicularly with radial actin filaments, mechanically coupling both cells' cytoskeletons. Force transmission is thought to stabilize focal adherens junctions by recruiting regulatory proteins such as vinculin and members of the Arp2/3 complex proteins. Remarkably, the activation of Rho-associated protein kinase (ROCK) is crucial for the formation of focal adherens junctions[98].

Next, during focal adherens junction maturation, an expansion of the cell-cell contact area is paralleled with the formation of membrane protrusions and lateral rearrangement of E-cadherin, resulting in the formation of linear adherens junctions[99]. Myosin-II-generated force is thought to enable the maturation of focal adherens junctions into linear adherens junction, as its activity is maximal near both cells' adhesion sites. In these junctions, actin bundles align in parallel to the membrane, albeit their interaction with linear adherens junctions and downstream effects are to date still unclear. EPLIN, a protein that binds α-catenin- and F-actin, is required for the maintenance of linear adherens junctions[99]. Finally, a higher order of structure of adherens junctions appears in apico-basally polarized epithelia, where cells grow in height and form zonula adherens junctions in the apical region, typically localized below tight junctions[99,100]. Thick, myosin-II-dependent actin bundles align with zonula adherens junctions together with actin linkers such as α-catenin, EPLIN and vinculin[99].

Beyond maintaining tissue cohesiveness, E-cadherin has been reported to be involved in a wide range of mechanical processes at different levels[50,101–104]. In the next sections I will molecularly dissect E-cadherin interactions, focusing on their role in regulating both internal and external forces to which cells within tissues are subjected.
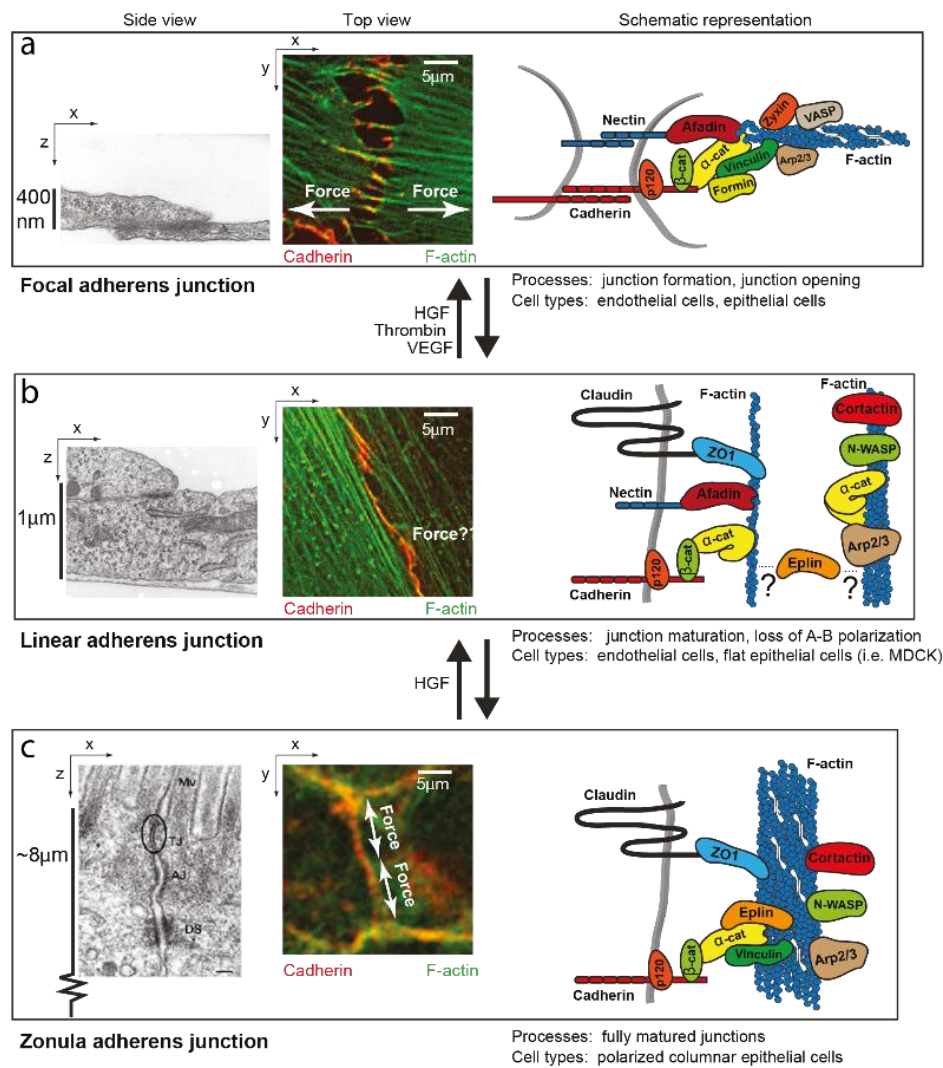
Figure 1-12. Adherens junction structures associated with the actomyosin cytoskeleton. *Adherens junctions display different structures depending on the maturity of the junction, epithelia polarity or junction remodelling mediated by hormones. (a) Focal adherens junctions are found during the formation of junctions. Remarkably, its punctate morphology is reminiscent of the architecture of nascent focal adhesions. In focal adherens junctions, cadherin adhesions are typically pulled by perpendicular actomyosin bundles, likely triggering the presentation of α-catenin VBS concomitant with vinculin recruitment to the forming junctions. (b) Focal adherens junctions mature into linear adherens junctions, where cadherin localization adopts a linear rather than punctate morphology. Actomyosin bundles align in parallel to cell-cell contacts, although they do not co-localize. Vinculin typically lacks in linear adherens junctions, suggesting that these structures are not under tension. (c) In polarized epithelia, linear adherens junctions mature into zonula adherens junctions, where actomyosin bundles co-localize with cadherin. The formation of zonula adherens depends on the recruitment of vinculin and Eplin to the junctions, evidencing that those junctions transmit intracellular tension across epithelia. Adapted from Huveneers et al.[99]*

3.1.1 E cadherin: structure and adhesion dynamics

E-cadherin is a transmembrane protein bearing an extracellular N-terminal domain that contains 5 similar ectodomains named from EC1 to EC5, whose interaction with other E-cadherin ectodomains presented by adjacent cells allows for the formation of adherens junctions in a calcium-dependent manner[105,106]. E-cadherin's c-terminal is cytosolic, whereas its interaction with the so-called adaptor proteins enables for cytoskeleton coupling between neighbouring cells[4,107,108].

The cadherin familiy includes a number of proteins whose role is to participate in the formation of different types of cell-cell junctions[4]. In this thesis, we focus on a "classical" cadherin, specifically E-cadherin. The type of bond cadherins form is important to understand their mechanosensory role, and although they werewere historically thought to interact homophilically, recent research showed that they also mediate heterophilic interactions[109], whose tensile strengths and force generation spectrum is very similar to that of homophilic interactions, as experimentally reported in[109,110].

The conformational state of classical cadherins is very dynamic and changes between the X-dimer and the strand-swap dimer conformation both stochastically and according to external mechanical stimuli (Figure 1-13). The X-dimer cadherin conformation behaves as a catch bond, and thus its lifetime increases with increasing tensile forces. In contrast, the strand-swap dimer conformation acts as a slip bond, which becomes short-lived with increasing tension[111].
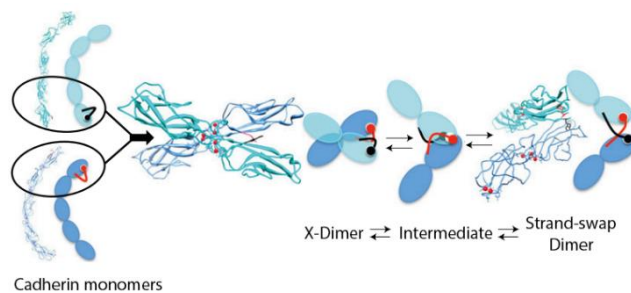
Figure 1-13. Cadherin-based conformational bindings. *In their closed configuration, cadherin monomers present a tryptophan residue in their respective pockets. Upon cadherin-based interactions, the EC1-2 domains of adjacent cadherins interact constituting the X-dimer conformation, behaving as a catch bond. The X-dimer configuration stochastically changes to the strand-swap dimer conformation, where the aforementioned tryptophan residue is inserted into the pocket of its adhesive partner, behaving as a slip bond. Finally, during the transition from X- to strand-swap dimer, an intermediate conformation behaving as an ideal bond is adopted, providing cells with mechanical insensitivity during very short time periods. Adapted from Rakshit et al.[112]*

A third type of E-cadherin binding conformation was described, during which the bond becomes insensitive to force[111,112]. Therefore, besides forming typical catch and slip bonds, E-cadherin conformational interactions also form ideal bonds. The latter are developed while cadherins undergo an X- to strand-swap dimer conformational change, and despite their lifetime being at the order of centiseconds[112], they could potentially provide cells with the required mechanical insensitivity to temporarily accommodate large tissue deformations.

Besides the aforementioned conformational bindings a pair of E-cadherin form, cells also form *cis*- and *trans*- interactions with their own and their neighbours' EC1-5, respectively, thus entailing a higher level of cell-cell contact regulation[113] (Figure 1-14).

At the cytosolic domain, cadherins interact with cell cytoskeleton filaments through adaptor proteins, as previously noted. The protein family responsible to mechanically and biochemically couple the extracellular environment with the cells' inner protein networks in a cadherin-dependent manner is referred to as the cadherin adhesome[105]. Of all the myriad of adaptor proteins that constitute the cadherin adhesome, the ones belonging to the catenin family play a crucial and very well-described role in E-cadherin interactions[107].
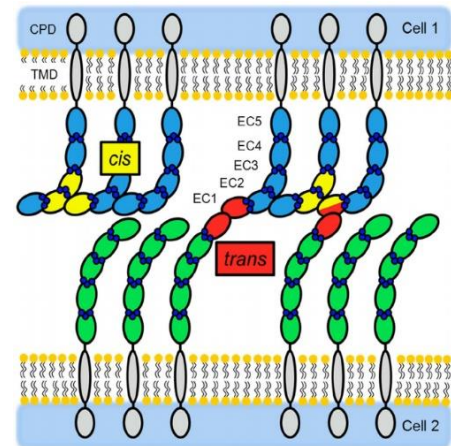
Figure 1-14. Schematic cartoon of cis and trans interactions between E-cadherin ectodomains. *Lateral cis interactions (yellow) occur between adjacent E-cadherin ectodomain expressed in the same cell. Trans interactions (red) occur between E-cadherin ectodomains expressed in neighbouring cells. A combination of cis and trans interactions is also depicted on the right, where an E-cadherin ectodomain of a cell interact with a neighbour cell's ectodomain that is undergoing cis interactions. Adapted from Fichtner et al.[113]*

For example, E-cadherin endocytosis is impaired by the binding of catenin p-120 to its juxtamembrane domain, resulting in a decreased turnover and thus an increased binding lifetime[114]. Catenin p-120 is also involved in cytoskeletal filaments remodelling near the E-cadherin interactions, where it recruits microtubules to promote junction maturation in parallel to regulating the activity of Rho GTPases ultimately modulating the actin cytoskeleton dynamics[114].

β-catenin constitutes another example of the outstanding role of the catenin family in the context of adherens junctions. Briefly, E-cadherin cytoplasmic domain interacts with β-catenin, which in turn binds α-catenin, ultimately allowing for coupling between E-cadherin molecules and the actin cytoskeleton[107]. α-catenin constitutes a mechanosensitive protein at the cell-cell adhesion complex, whose role will be discussed in the next section.

Summing up, the cadherin-catenin complex is found in interactions involving all classical cadherins and represents the minimal functional protein complex to allow for cadherin adhesions[107]. Recruitment of additional proteins results in different interacting cadherin adhesomes, providing the cells with further complexity in adhesion structures as well as the ability to carry out different functions[99,105].

3.1.2 E-cadherin regulates cell contractility

During recent years, an important number of research studies have shed light on the mechanics of cadherin adhesion. Namely, Buckley et al. made use of an *in vitro* optical trap-based assay to study the binding dynamics of the E-cadherin/α-catenin complexes with F-actin[107]. Briefly, tension was applied to the complexes by means of an oscillatory movement of the stage in the direction parallel to the orientation of F-actin filaments. Interestingly, the E-cadherin/α-catenin complex was reported to form a catch bond with F-actin whose lifetime displayed at least a 20-fold increase in the presence of tension, compared to a condition where the stage was immobile and thus tension was not applied. Therefore, overcoming a minimum force threshold is required for α-catenin to bind F-actin, indicating that the transmission of force is necessary for the formation and stability of cadherin-based cell-cell junctions[107].

In vivo, force enabling E-cadherin and F-actin coupling is conferred by the actomyosin cytoskeleton. Research studies showed that an enrichment of E-cadherin at the adherens junctions is paralleled with a local increase in RhoA activity triggered by a conformational activation of α-catenin[115], resulting in the local recruitment and activation of myosin II motors specifically at the cell-cell junctions[116] (Figure 1-15).

Whereas three myosin II isoforms are expressed in mammals, only myosin IIA and myosin IIB are found at the cell-cell junctions[100]. Recruitment of myosin IIA and myosin IIB at those junctions is mediated by signalling cascades and feedback loops involving ROCK-1 and Rap1, respectively[100]. Remarkably, a decrease in cell contractility by inhibiting myosin light-chain kinase (MLCK) either by addition of Blebbistatin or ML-7 resulted in a decreased cell-cell adhesiveness as a consequence of an impaired ability of the cells to locally concentrate E-cadherin at the cell junctions (Figure 1-15 b). Additionally, removal of either myosin-II or E-cadherin from the cell-cell junctions resulted in an impaired localization of the other, suggesting that both myosin-II (and thus a local increase in contractility) and E-cadherin are crucial for the generation and maintenance of cadherin-based cell junctions[100] (Figure 1-15).

In the same line, a direct correlation between E-cadherin expression levels and cell contractility was found in a recently published work: Pérez-González et al. used an experimental set-up where a dexamethasone-inducible increase in E-cadherin expression resulted in a three-fold increase in the di-phosphorylated myosin light chain (ppMLC), resulting in 2D epithelial cell monolayers eventually rounding up and detaching from the experimental substrates[117]. Therefore, an increase in E-cadherin expression is paralleled by an increase in ppMLC and thus increased cell contractility. Taken together,

these results indicate that E-cadherin ultimately mediates the generation of forces at the cell-cell interface through regulating cell contractility.
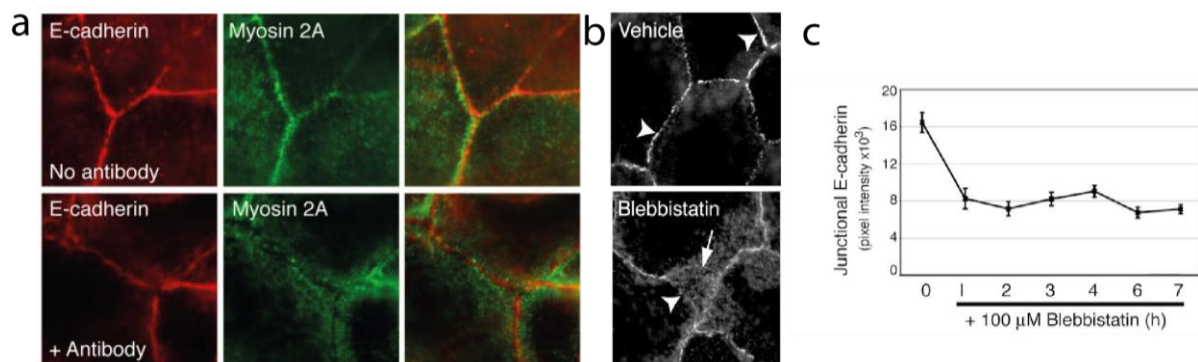
Figure 1-16. E-cadherin and Myosin IIA are mutually required for the formation and stability of E-cadherin-based junctions. (a) Upon addition of E-cadherin-blocking antibody, both E-cadherin and Myosin IIA show an impaired localization at the cell-cell junctions. (b) E-cadherin immunostaining in controls and blebbistatin-treated cells. Upon treatment with a light myosin chain inhibitor (Blebbistatin), E-cadherin localization at the cell-cell junction is impaired. (c) Junctional E-cadherin decreases with time upon treatment with Blebbistatin. Adapted from Shewan et al.[116]

Finally, a FRET-based experimental set-up carried out by Borghi et al. showed that myosin II is constitutively active near the cell membrane both in bound and unbound E-cadherin molecules, and thus membranal E-cadherin is under constitutive actomyosin-generated tension regardless of its binding with E-cadherin molecules presented by adjacent cells[118]. This could possibly confer an additional role for E-cadherin in the transduction of mechanical forces between the actomyosin cytoskeleton and the plasma membrane. Moreover, stretch experiments showed that tension was further increased at bound E-cadherin localized to cell-cell junctions compared to unbound E-cadherin[118], indicating that cells sense other cells' mechanical properties through cadherin-based interactions and adapt to the force they exert accordingly. Therefore, through the tight control of the regulation of internal force generation mediated by myosin II activation, cadherins constitute a mechanosensitive complex to sense and adapt to extracellular forces[118,119]. This point will be addressed in the next section, where we will review the molecular mechanisms behind E-cadherin-mediated force generation, sensing and adaptation in response to extracellular mechanical stimuli.

3.1.3 E-cadherin at the tissue level: maintenance of tissue cohesiveness and mechanosensing to adapt to extracellular forces

As introduced in the previous chapters, E-cadherin plays a crucial role in the maintenance of tissue integrity during collective cell migration. In this section, I will focus on the molecular mechanisms that enable the coordination of tissues and the maintenance of their cohesivity.
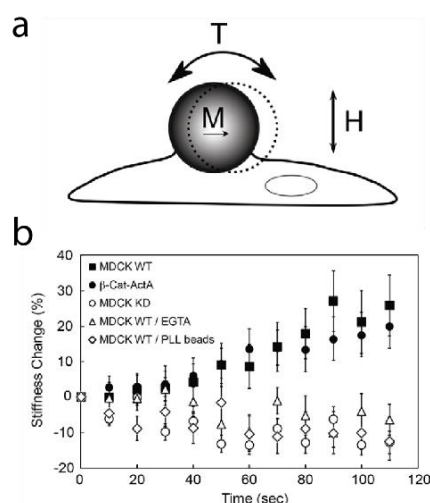
Figure 1-18. α-catenin is needed during E-cadherin-dependent mechanotransduction. (a) Cartoon depicting a magnetic twisting cytometry experiment. (b) Stiffness change mediated by E-cadherin during the magnetic twisting cytometry experiment. In contrast to α-catenin KD MDCK cells, wild-type cells underwent a cell stiffening event in response to force applied through an E-cadherin-coated magnetic bead. This phenomenology was abrogated in PLL-coated magnetic beads or EGTA treatment. Adapted from Barry et al.[108]

Prior to Buckley et al.'s finding on the catch bond formed between the E-cadherin/α-catenin complex and F-actin discussed in the previous section[107], Leduc et al. made use of an experimental set-up based on magnetic beads aiming to unravel the mechanosensitive role of α-catenin[101]. Briefly, magnetic beads were embedded on top of cells, which were next placed under a magnetic field. The amplitude of the oscillation of E-cadherin-coated magnetic beads decreased with time compared to that of pLL-coated beads, indicating that a local cell stiffening event occurred upon the transmission of force at E-cadherin junctions. Even though the underlying mechanisms were then unknown, vinculin was reported to be required for the E-cadherin-mediated cell stiffening event[101]. Two years later, Rangarajan et al reported for the first time a crystal structure of α-catenin's vinculin binding site (VBS) with a unique unfurled conformation when bound to vinculin[120].

In the same line, Barry et al. showed that MDCK cells carrying a deletion in α-catenin's VBS failed to actuate the force-dependent reinforcement of cadherin junctions[108], suggesting that vinculin binding to the unfurled conformation of α-catenin allows for a local stiffening event driven by local actin recruitment in response to external forces applied on E-cadherin-based cell-cell adhesions. Thus, in a similar way to what happens to talin at the cell-ECM interface[22], stretched molecules of α-catenin at cell-cell junction complexes undergo a conformational change over a tensional

Figure 1-17. α-catenin unfolds upon tension transmission in E-cadherin-based junctions, presenting a previously cryptic VBS and allowing for vinculin recruitment concomitant with actin bundles recruitment to the cell junctions. Adapted from Alberts et al.[4]

threshold where a previously cryptic VBS domain is then accessible to vinculin[120] (Figure 1-17). In all, Barry et al.'s results further corroborated the important role of the cadherin-catenin complex in allowing for mechanosensing events at the cell-cell interface.

Another striking example of the role of the adherens junctions in the transmission of force across tissues was provided by Sunyer et al.[39]. In an experimental set-up enabling the measurement of cellular traction forces, E-cadherin was reported to allow for the long-range transmission of force across an epithelial cell monolayer during its asymmetric expansion on a gradient of stiffness coated with fibronectin, evidencing that cadherin-based junctions enable the mechanical coupling across tissues. Remarkably, either deletion of α-catenin or inhibition of myosin-II resulted in a compromised tissue integrity and an impaired outcome in their associated CCM[39] (Figure 1-19). Taken together, these results indicate that the α-catenin mechanosensor plays a crucial role in the context of CCM, providing cells with the ability to adapt to extracellular forces derived from cadherin-based adhesions to ultimately maintain tissue integrity and ensure coordination during CCM events.
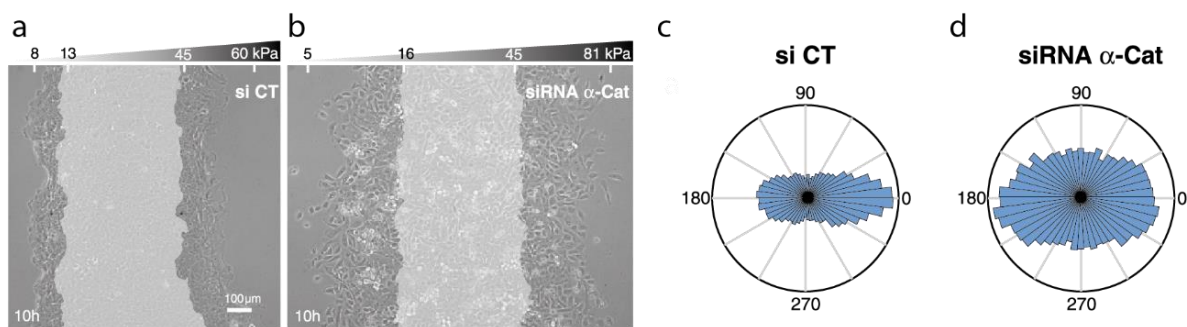
Figure 1-19. Tissue cohesivity and collective durotaxis are impaired upon silencing of α-catenin. Whereas control MCF10-A cells expanded asymmetrically (a,c) on a gradient of stiffness, a symmetric expansion was observed upon silencing α-catenin (b,d), paralleled with the loss of tissue integrity. Adapted from Sunyer et al.[39]

In analogy with the previously discussed increase in traction forces with increasing stiffness reported on ECM-coated substrates[22,34], the development of *in vitro* techniques to coat hydrogels of varying stiffness with E-cadherin[119,121–124] provided researchers with further evidence of E-cadherin-mediated mechanosensing. However, unlike substrate functionalization with ECM proteins, substrate functionalization with E-cadherin extracellular domains (EC1-5) needs to contemplate their orientation. In elastic hydrogels coated with oriented EC1-5 using different approaches, traction forces were systematically higher in stiff gels compared to soft gels[108,125] (Figure 1-20). Interestingly, Collins et al. reported that gels displaying a stiffness below 30kPa did not support MDCK cell adhesion or spreading[119], attributing this phenomenology to the physiological stiffness value reported for an MDCK cell monolayer, which is in the range of 33kPa[126].

Whereas most of the published techniques to coat hydrogels with oriented cadherins make use of a chimeric molecule consisting of the EC1-5 with a C-terminal fused to a human IgG-Fc tag[119,124,127], whether the IgG domain conforming the Fc/E-cadherin chimera undergoes conformational changes potentially hindering the readout traction forces under cadherin-transmitted tension has not been studied. A minor number of research studies coated either glass surfaces[122,128] or hydrogels[121] with oriented EC1-5 fused to a histidine tag (Histidine-tagged EC1-5) by means of a double bivalent ion chelation through N-alpha,N-alpha-Bis(Carboxymethil)-L-Lysine (NTA) and Histidine-tagged EC1-5, where the Fc tag is lacking and thus no unfolding of the IgG domain potentially alters the readout of traction force generation.
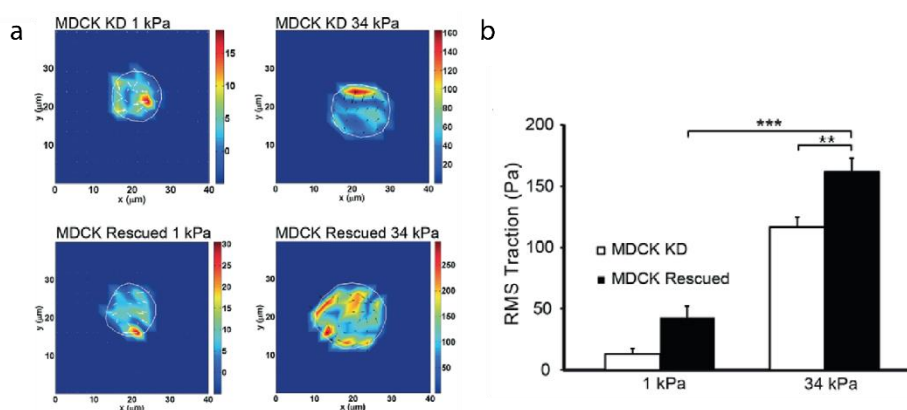
Figure 1-20. Traction forces exerted by cells seeded in E-cadherin-coated hydrogels increase with substrate stiffness. (a) Color-coded traction force maps of MDCK α-catenin KD and MDCK rescued cells on 1 kPa and 34 kPa stiffness gels. (b) E-cadherin-generated cell tractions increase with substrate stiffness in an α-catenin-dependent manner. Adapted from Barry et al.[108]

In all, a significant number of research studies indicate that E-cadherin ultimately provides cells with the ability to mechanically sense other cells' forces and respond to them by internally modulating their force generation spectrum to equal the forces generated by their neighbours. However, cells *in vivo* are usually surrounded by other cells as well as ECM. Therefore, cells typically establish both cell-cell and cell-ECM adhesions at the same time, triggering different signalling pathways that share common protein effectors such as vinculin[101,129], necessarily implying a biochemical crosstalk between cell-cell and cell-ECM adhesions. Finally, cell-ECM traction forces were reported to modulate endogenous tension at cell-cell contacts[130], implying that a mechanical crosstalk between those adhesions also exists likely due to the similarities in their architecture, as both types of adhesions are regulated by the cell cytoskeleton[96].

3.2 Collective cell migration mechanics

The mechanics of collective cell migration have been increasingly studied during the last years. Previous research showed that CCM arises from the interplay between cell-cell adhesion, cell-substrate adhesion and cell contractility[131]. Whereas cell-substrate adhesions provide new anchoring points for migrating groups of cells at the leading edge, myosin-II-driven contraction of actin filaments anchored to those newly-formed cell-substrate adhesions drives the generation of traction forces in a stiffness-dependent manner that results in the build-up of intracellular tension[131]. In this scenario, cell-cell adhesions enable the formation and mechanical coupling of front-to-rear supracellular actin filaments that transmit tension intercellularly across the whole migrating cohort(38). Manipulation of cell-cell adhesions or inhibition of myosin-II activity leads to the abrogation of intercellular coordination and thus impaired CCM[39,131] (Figure 1-19), indicating that tension transmission throughout a migrating cohort is mediated by the coupling of contractile forces between neighbouring cells[39]. Therefore, the mechanical properties of substrates are integrated at the cell-substrate interface in an interplay with cell-cell adhesion dynamics and cell contractility ultimately regulating CCM.

In order to migrate with a certain direction to ultimately reach their target location, collectively migrating cohorts must establish a front-rear polarity[132], just as explained for migrating single cells. In migrating cell collectives, cells at the edges constitute the so-called leader cells, whereas cells occupying central regions in the cell collectives represent the follower cells[133]. To advance, leader cells set the direction of migration by polarizing and extending lamellipodia towards spaces devoid of other cells. Similarly, follower cells protrude frontal cryptic lamellipodia (c-lamellipodia) below anterior cells that not only result in traction forces generation but also increases cell-cell contact area, hence strengthening cell-cell adhesion[134]. Despite leader cells exert higher traction forces than follower cells likely due to their marked polarization, collective cell migration requires the active mechanical contribution of both leader and follower cells[90,135].

Tissue polarity is set along the whole cell monolayer through the establishment of gradients of Rho-GTPase activity from the front to the rear of the collective, triggered by leader cells' initial polarization[136]. Together with tissue cohesivity, this is achieved through intercellular junctions that enable the transmission of tension from the front to the rear of a migrating cohort through emerging actin supracellular organization structures that obviously lack in single cell migration[137,138]. As a consequence, in contrast to single cell migration, traction forces are not balanced within cells undergoing CCM, where normal tractions (tractions perpendicular to the leading front) become systematically lower from the edge of the cohort to the centre, whereas intercellularly transmitted

tension follows the opposite trend[39] (Figure 1-21). Therefore, the force balance occurs globally at the supracellular scale rather than at the single cell scale during CCM.
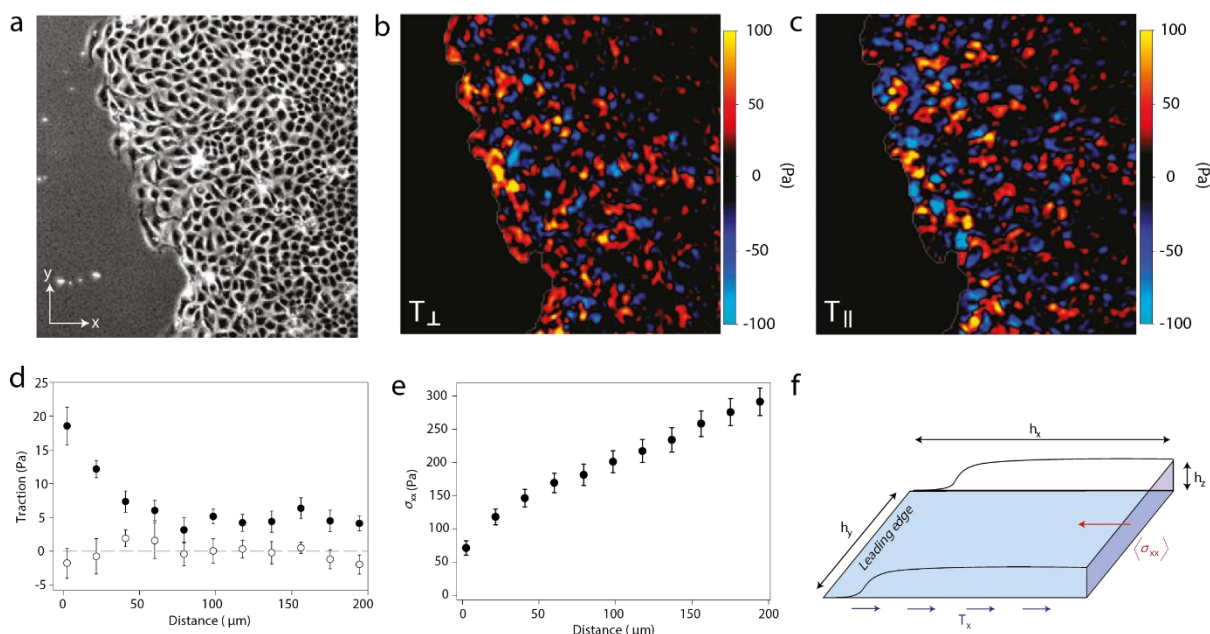
Figure 1-21. Traction forces generated by a collectively migrating sheet. (a) Phase contrast image with the leading edge of the monolayer to the left. (b) Tractions normal to the leading edge. (c) Tractions parallel to the leading edge. (d) Quantification of normal (black) and parallel (white) tractions to the leading edge as a function of distance from the leading edge. (e) Quantification of stress within the migrating monolayer as a function of distance from the leading edge. (f) Cartoon depicting the quantification of stress within the advancing cell monolayer. The average stress parallel to the leading edge (σ_{xx}) was calculated by integrating tractions T_x along h_x. Adapted from Trepat et al.[90]

Besides ensuring tissue cohesivity and coordination, the transmission of tension at the cell-cell junctions opposes to CCM: high intracellular tension transmission results in fast actin retrograde flows with a concomitant decreased actin net polymerization at the leading edges, thus slowing CCM. In line with this, P. Hoj et al.[139] showed that MDCK monolayers treated with HGF underwent cell scattering caused by the rupture of intercellular junctions when seeded on stiff substrates, whereas the cohesivity of the monolayers remained unaltered on soft substrates. pMLC levels were reported to decrease dramatically upon HGF treatment, paralleled with an increase in integrin-mediated adhesions. Strikingly, pMLC levels recovered after 2 h, concomitant with intercellular junction disruption only in MDCK monolayers on stiff substrates[139]. The fact that MDCK monolayers treated with HGF and seeded on soft substrates did not undergo cell scattering indicates that the interplay between the tension transmitted at the cell-cell junctions with the stiffness-dependent forces generated at cell-substrate adhesions dictates the outcome of CCM. Sunyer et al.[39] provided further evidence of this, as monolayers of epithelial MCF10A cells seeded on gradients of stiffness expanded asymmetrically on the stiff and soft edge. This work represented the first evidence of collective durotaxis, which will be reviewed in the next section.

3.3 Collective durotaxis

Collective durotaxis refers to the migration of a group of cells towards stiffer regions when presented to a gradient of stiffness. In their work, Sunyer et al.[39] reported that the expansion of epithelial monolayers of MCF10A cells occurred asymmetrically on gradients of stiffness coated with fibronectin, whereas single MCF10A cells displayed a random migratory behaviour when presented to the same experimental substrates. Therefore, similarly to chemotaxis[80,140] and electrotaxis[79], collective durotaxis is far more efficient than single cell durotaxis[39]. The underlying mechanisms for single cell durotaxis previously explained in this thesis also apply to collective durotaxis, albeit signal integration occurs at the supracellular level rather than the single cell level. According to Sunyer et al.'s work[39], collective durotaxis emerged as a result of the integration of a higher difference in stiffness comprised between the soft and stiff edge in MCF10A monolayers compared to single MCF10A cells.
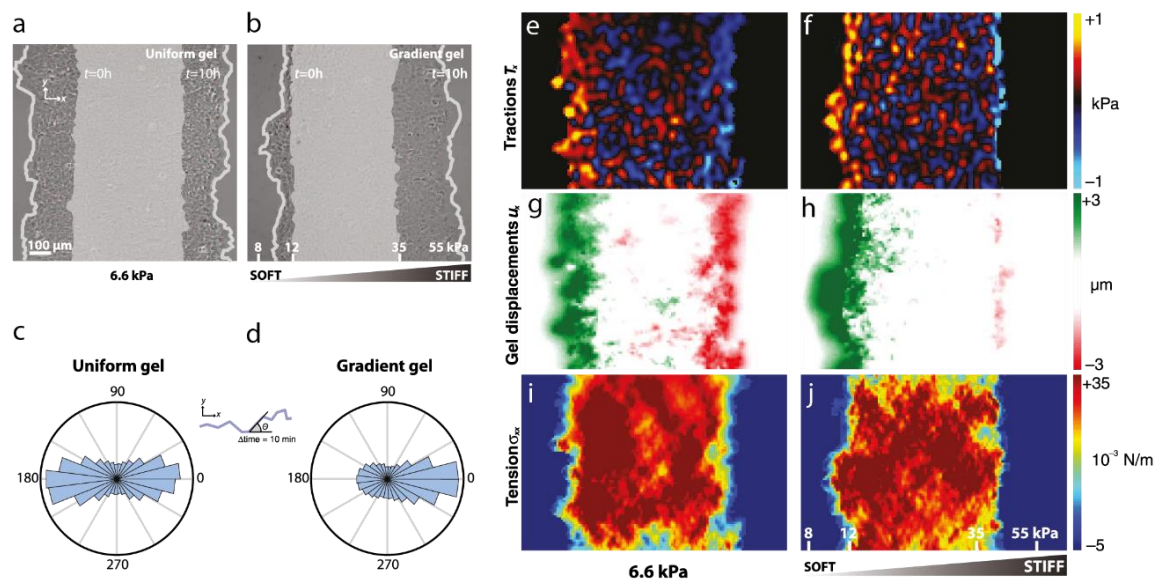
Figure 1-22. MCF10A epithelial cell monolayers undergo collective durotaxis by asymmetrically expanding on a gradient of stiffness coated with fibronectin. *(a) Symmetric expansion of a monolayer on a uniform stiffness gel. (b) Asymmetric expansion of a monolayer on a gradient of stiffness. (c,d) Angular distributions of cell trajectories for experiments shown in (a) and (b), respectively, show that monolayers durotax on gradients of stiffness. (e, f) Maps of the Traction component T_x for experiments shown in (a) and (b), respectively. (g) As a result of the global balance in tractions, gel deformations are equal in both edges of an expanding monolayer on a uniform stiffness. (h) Gel deformations are higher in the soft edge of a monolayer expanding on a gradient of stiffness. (i,j) Maps of the intercellular tension component σ_{xx} for experiments shown in (a) and (b), respectively. Adapted from Sunyer et al.[39]*

The asymmetric expansion of MCF10A cell monolayers occurred as a consequence of the global traction balance within the monolayer, resulting in higher substrate deformations at the soft edge of a monolayer expanding on a gradient of stiffness coated with fibronectin, compared to the stiff edge[39] (Figure 1-22 g,h). This phenomenology was abrogated both upon disruption of cell-cell contacts either by genetically manipulating α-catenin, through the addition of blebbistatin (a myosin-II specific

inhibitor) (Figure 1-19), or by laser-ablating cell-cell adhesions, evidencing the pivotal role of intercellular junctions during collective cell migratory processes such as collective durotaxis[39].

Interestingly, a cell monolayer expanding asymmetrically on a gradient of stiffness can be modelled as a one-dimensional contractile unit exerting forces on its underlying deformable substrate through discrete focal adhesions and viscous friction, where a generalized clutch model predicts the observed durotactic phenomenology. Briefly, each FA is modelled as a single clutch where traction is exerted. In order to maintain force balance throughout the expanding cell monolayer, substrate deformations at the soft edge are larger than at the stiff edge, ultimately driving an asymmetric expansion of the monolayer towards stiffer regions when seeded on a gradient of stiffness due to the higher stability of the FA formed in the stiff edge[39].

In all, Sunyer et al.'s work unveiled that collective durotaxis emerges from long-range intercellular force transmission within an expanding cell monolayer seeded on a gradient of stiffness[39]. However, the observed durotactic behaviour was an asymmetric expansion rather than the net translocation of cell collectives, likely due to the high spreading displayed by epithelial cell monolayers on ECM-coated substrates.

Recent research studies suggested that durotaxis might play a crucial role during development. For example, Zhu et al. reported that a gradient of stiffness appears concomitantly with the limb bud formation during mouse development[67]. Also, Barriga et al. found that the head mesoderm underlying the cephalic neural crest in *Xenopus* stiffens during morphogenesis, concomitant with the onset in the migration of neural crest cells[141] (NC). Briefly, by grafting pre-migratory NC onto the head mesoderm of non-migratory stage embryos and vice-versa, Barriga et al.[141] reported that the *in vivo* gradient of stiffness generated at the head mesoderm is necessary and sufficient to trigger the directed migration of NC. Even though there was no evidence of *in vivo* collective durotaxis up to recently, these studies suggested that collective durotaxis could represent a potential candidate to explain biological processes involving the collective migration of cells whose drivers remain largely unknown. In fact, Shellard and Mayor extended Barriga et al.'s work[141] and reported the first evidence of *in vivo* durotaxis during the NC migration in *Xenopus laevis*[52]. By combining *in vitro* and *in vivo* approaches, Shellard and Mayor reported that the NC self-generates a gradient of stiffness in the adjacent placodal tissue, which is then used as a mechanical cue to guide their migration together with a chemotactic gradient of Sdf1 secreted by cranial placoids, where both types of gradients synergistically define the migratory direction. Finally, rear actomyosin contraction was reported to be required for this

phenomenology[52] (Figure 1-23 e), further indicating that the interplay between cell contraction and cellular tractions dictates the outcome of collective cell migration.
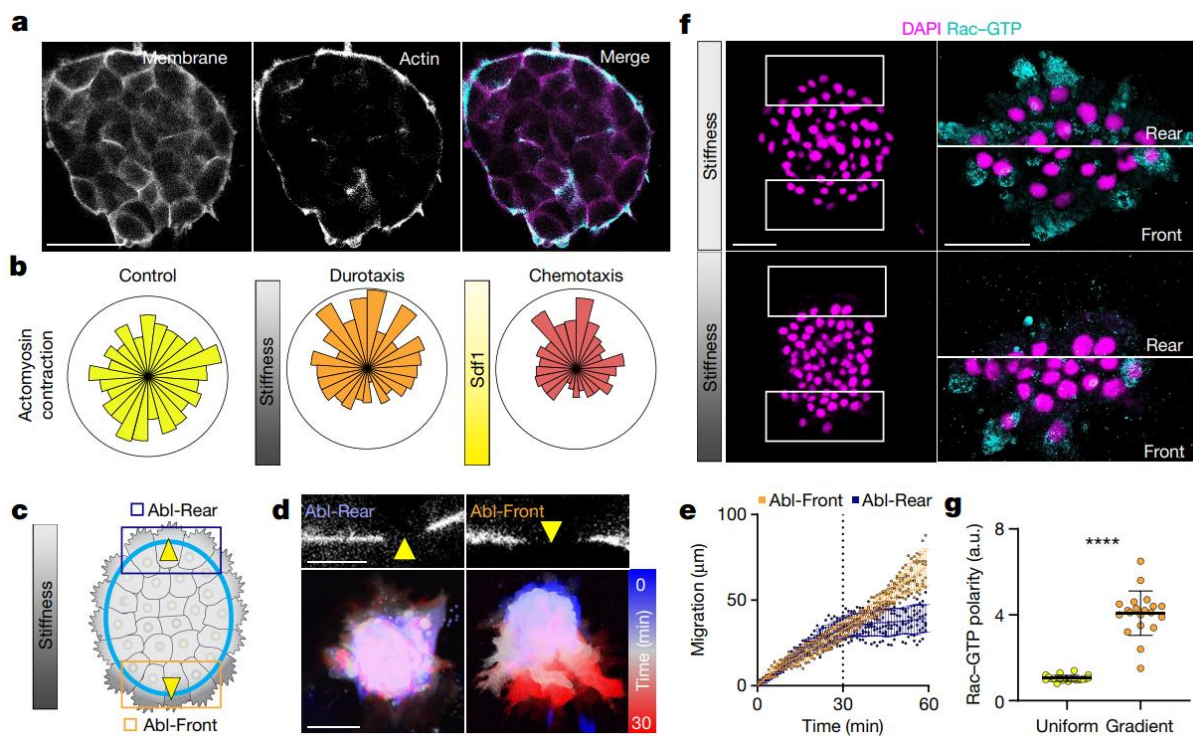
Figure 1-23. Polarized actomyosin contraction enables the synergistic durotactic/chemotactic migration of the developing neural crest. *(a) Neural crest expressing fluorescently tagged LifeAct and a membrane marker (Scale bar is 50 µm), showing a supracellular actin organization. (b) Actomyosin contraction is enhanced at the rear of the cohort during the in vitro migration of the neural crest. (c) Scheme depicting actomyosin cable ablation (yellow arrowheads). (d) Lifeact images of the ablation in the actomyosin cable (top) at the rear (Abl-Rear) and front (Abl-Front) of neural crest clusters on a gradient of stiffness (Scale bar is 10 µm). Time-coded projection of clusters (bottom) is shown for each condition (Scale bar is 100 µm). (e) Quantification of migration, which halts upon the ablation of rear actomyosin cables. Dashed line indicates the timepoint of the ablation. (f) Immunostaining of Rac-GTP (cyan) and DAPI (magenta) in neural crest clusters on a polyacrylamide substrate of uniform stiffness (top) or a stiffness gradient (bottom) (Scale bar is 50 µm). (g) Quantification of Rac-GTP polarity, indicating an increase in the contraction at the rear of a migrating neural crest cluster. Adapted from Shellard et al.[52]*

Remarkably, migrating NC adopted a shape reminiscent to that of a drop of water expanding on a surface (Figure 1-23 a). In this line, computational and active gels-based approaches modelling collective cell durotaxis within the framework of active wetting have been proposed[142,143,70,144,145]. In the following section of this thesis, I will introduce active gels and comment on active gels-based models that tackle collective cell migration as an active wetting process, in analogy with the physics of active polar fluids.

4. Active matter to model the living

Historically, the study of collectively migrating cells dates back to the early twentieth century, when scientists initially proposed pressure[146,147] or the pulling forces generated by cells at the edges of tissues[147] as the drivers of CCM. Therefore, the initially proposed mechanisms of cell migration were largely physical, whereas relevant biological aspects were mostly ignored. With the discovery of genes and proteins during the twentieth century, the subject of study changed towards individual molecules rather than the tissue level, causing a halt in the study of CCM from a physical point of view. Nevertheless, recent conceptual advances as well as the development of cutting-edge experimental techniques have motivated scientists worldwide to re-tackle the study of CCM from a physical perspective: the study of traction forces, velocimetry fields and strain tensors is now more accessible than ever, and computational calculations have become extremely effective. Such technological advances were paralleled by the proposal of the theory of active matter, constituting an ideal framework to study different biological processes that reside in an out-of-equilibrium state spanning all the scales of the living[56]. For example, active matter theories can capture the flocking motion of birds[148], as well as out-of-equilibrium subcellular elements such as the cell cytoskeleton[149].

4.1 Active gels

The rheology of the cell cytoskeleton changes from fluid-like to solid-like with increasing stiffness[77]. Whereas a typical circumferential actin retrograde flow is observed in cells seeded on soft substrates, actin stress fibers anchored to FA are formed in cells on stiff substrates[77]. This change in the rheology of cells emerges as a consequence of the higher orientational order of actin filaments on stiff substrates, highly resembling phase transitions occurring in passive materials such as liquid crystals[56] (Figure 1-24).
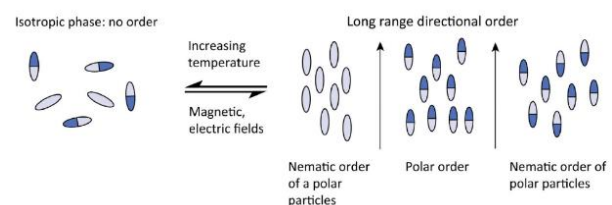
Figure 1-24. Cartoon depicting isotropic-to-nematic phase transitions in liquid crystals. In their isotropic phase, liquid crystals orientation is random. However, upon externally supplied energy, an isotropic-to-nematic phase transition occurs, where different orientational orders depending on the nature of the liquid crystals emerge. Adapted from Ladoux et al.[56]

Liquid crystals undergo phase transitions upon the application of an external stimuli. In a context providing insufficient energy, liquid crystals are in an isotropic phase, where individual particles show no preferential order. However, upon the input of energy in the form of temperature, magnetic or electric fields, liquid crystal's individual constituents align and adopt a long-range directional order[56]. Depending on the polarity of liquid crystals and the nature of the external stimuli, particles align in a

nematic or polar order. Due to the polarity of actin filaments and the orientation of filaments with increasing substrate stiffness, the change in cell rheology can be modelled as an analogy of an isotropic-to-nematic phase transition experienced by liquid crystals. In this line, Gupta et al.[77] showed that with increasing substrate stiffness, actin filament density increased up to a critical value above which a nematic order emerged, resulting in an anisotropy in the stress. This phenomenology directly affects intracellular polarization, as the orientational order of actin filaments in cells allows for a cooperative effect of pulling forces generated by the molecular motors along the same direction. Therefore, the actomyosin cortex itself is mechanosensitive as a result of the higher nematic orientational order of actomyosin cables in stiffer substrates[56]. This in turn affects cell polarization, with cells generating anisotropic stresses when seeded on a gradient of stiffness and thus potentially triggering durotactic responses. In these contexts, cells move along the lines where tension is maximal in a process called plithotaxis[56].

Originally, active polar gel models were motivated to describe the behaviour of the actin cytoskeleton[150–152], but recently, they have also succeeded in describing cell monolayers in motion. Despite the maintenance and adaptation of intercellular junctions, migrating groups of epithelial cells undergo cell rearrangements resulting in changes in their relative position within the migrating tissue. As a result, hydrodynamic patterns in cell rearrangements such as cell swirling, swarming, motion correlation between subgroups of cells or the propagation of waves arise over long time periods[153]. Therefore, CCM entails the emergence of fluid-like behaviours in migrating groups of cells over time scales of several hours or days, presenting a high resemblance to the motion of two-dimensional complex fluids. However, in contrast to the dynamics of inert fluids, cells proliferate and require energy to propel themselves, obtained from ATP hydrolysis and transduced into mechanical work, constituting a hallmark of active matter[154].

As opposed to other approaches to model CCM at the molecular level, the study of living matter in terms of active fluids integrates the intrinsic molecular effects of subcellular elements through a coarse-grained approach. In such, migrating groups of cells are modelled as an active fluid whose shape is determined by a tight interplay between the tissue's active properties and tissue-substrate adhesion[154]. For example, Pérez-González et al.[117] recently proposed a theoretical framework based in active matter to explain tissue expansion and retraction as the interplay between intercellular contractility and cell tractions within the framework of active wetting. Whereas this model understood tissue spreading as an active wetting process, in the next section I will summarize the literature on tissue spreading studied from the classical wetting paradigm approach.

4.2 Tissue spreading as a wetting process

As previously stated, tissues behave like fluids at long timescales, where hydrodynamic patterns in cell rearrangements such as cell swirling, swarming, motion correlation between subgroups of cells or the propagation of waves arise[153,155]. The fluid-like behaviour of tissues led researchers to understand the spreading and migration of collectives of cells as a wetting process, in analogy with the spreading of a passive fluid droplet on a surface.

Initial models of tissue wetting relied on theories where interfacial free energy minimization was the driving force of tissue spreading, leading to the development of the "*Differential adhesion hypothesis*"[156]. The experiments that led to this hypothesis were based on the mixture of embryonic cells of different amphibian species with different adhesion strengths, which spontaneously reaggregated to form germ layers in their developmentally correct positions[156], highly resembling the separation of immiscible liquids. According to the differential adhesion hypothesis, cells reorganized to adhere to other cells of similar adhesive strengths aiming to maximize the bonding strength and thus generate more thermodynamically stable structures.

Later studies involving genetic tools (enabling the tuning of the adhesiveness of S-180 cell aggregates -derived from a *Mus musculus* murine sarcoma- by modulating the expression of E-cadherin) as well as fabrication tools (enabling the tuning of the adhesiveness of substrates) provided a more accurate idea of the wettability of tissues[157]. Briefly, according to approaches based in a classical wetting paradigm, the outcome of tissue wetting would be dictated by the interplay between cell-cell and cell-substrate adhesion strengths. In cell aggregates showing high cell-cell adhesion and low cell-substrate adhesion, tissue wetting would be hindered by the low cell-substrate adhesion strength, resulting in the formation of spherical cell aggregates resembling a spherical droplet of water on a hydrophobic surface. Conversely, cell aggregates presenting low cell-cell adhesion and high cell-substrate adhesion would undergo faster and more efficient spreading events, in analogy with a droplet of water expanding on a hydrophilic surface. By observing the process of wetting of cell aggregates displaying different cell-cell adhesion strength on surfaces of varying adhesiveness, Douezan et al.[158] proposed the spreading parameter (*S*) to predict the wetting state of a cell aggregate, which is defined as:

$$S = W_{CS} - W_{CC},$$

where W_{CS} and W_{CC} refer to the cell-substrate and cell-cell adhesion energies per unit area, respectively. If cell-substrate adhesion energy is higher than cell-cell adhesion energy ($W_{CS} > W_{CC}$), the spreading parameter will be positive ($S > 0$) and thus cell aggregates will wet the substrate. In contrast,

if the cell-substrate adhesion energy per unit area is lower than that of cell-cell adhesion ($W_{CS} < W_{CC}$), the spreading parameter will be negative (S < 0) and thus cell aggregates will tend to either dewet or partially wet the substrates, resulting in spherical-shaped cell aggregates[158].

Douezan et al. suggested that S-180 cell aggregates spread like a viscoelastic drop at short timescales, whereas a precursor film from the aggregate appeared at longer timescales in adhesive clusters seeded on adhesive substrates[157] (Figure 1-25 a,b), highly resembling a "liquid phase" state of cells. Conversely, cell aggregates expressing low levels of E-cadherin seeded on adhesive substrates underwent cell scattering (Figure 1-25 c), highly resembling a "gaseous phase" state of cells. Besides dictating the adhesiveness of clusters, the expression levels of E-cadherin dictate the viscosity of cell aggregates: E-cadherin contributes to increasing the friction experienced between cells, and thus high expression levels of E-cadherin oppose to the wetting process of cell aggregates[158].
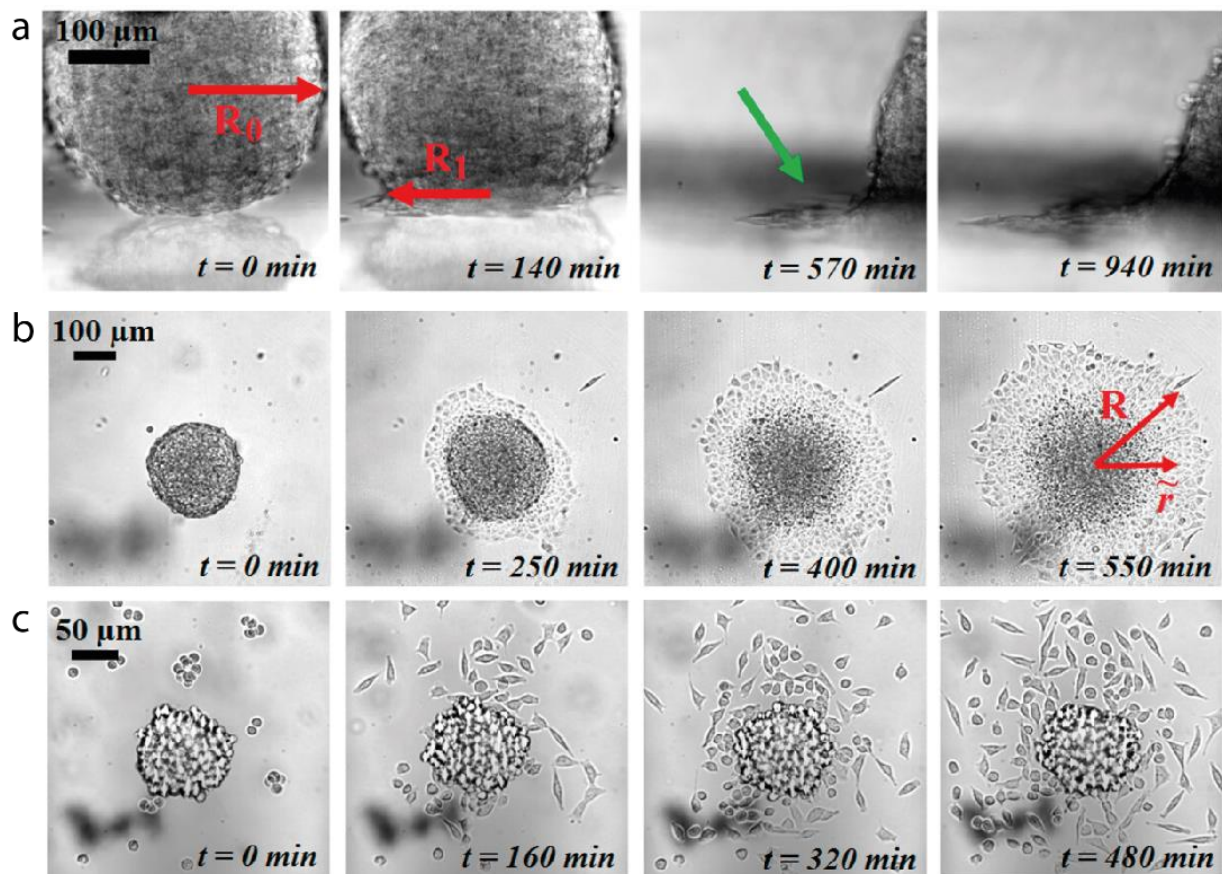
Figure 1-25. Tissue spreading on a surface in analogy with a wetting transition. *(a) Lateral phase contrast view of adhesive S-180 cell clusters spreading on an adhesive substrate show the formation of a film precursor of cells expanding from the cell aggregates (green arrow). (b) Top phase contrast view of adhesive S-180 cell clusters spreading on an adhesive substrate highly resembling a drop of water wetting a hydrophilic surface, featuring liquid-like state of matter. (c) Top phase contrast view of non-adhesive S-180 cell clusters spreading on an adhesive substrate, where cell scattering is observed, featuring gas-like state of matter. Adapted from Douezan et al.[157]*

The adhesiveness of substrates can be modulated by tuning either ligand density or substrate stiffness[56,117]. In line with the previous discussed study, Beaune et al. reported that varying substrate stiffness impacted on the wetting state of cell aggregates as well as their migratory outcome[143]. Indeed, murine sarcoma E-cad cell clusters were seeded on substrates of different stiffness (Figure 1-26). Cell clusters seeded on soft substrates (2-10 kPa) were not able to fully wet, whereas a net translocation of the partially dewet cluster was observed paralleled with single cell scattering. Cell clusters seeded on intermediate stiffness substrates (10-16 kPa) displayed a partially wet state, where a precursor film of cells started forming. With time, the dewetting of the precursor film started stochastically on one side of the cell clusters and they translocated by either adopting a penguin or giant keratocyte shape. Conversely, cell clusters seeded on stiff substrates (40 kPa) underwent full spreading with an initial precursor film of cells ultimately wetting the substrates[143] (Figure 1-26). Therefore, cluster migration showed a biphasic relationship with substrate stiffness, where the migration of clusters was optimal at intermediate stiffness values, correlating with a partial wetting state of cell clusters (Figure 1-26).
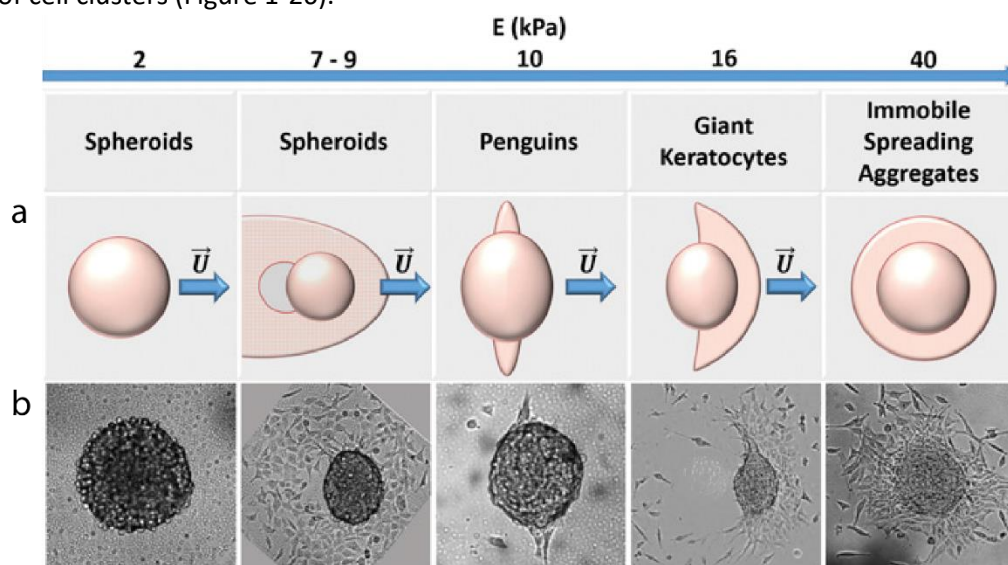
Figure 1-26. Substrate stiffness impacts on the wetting state and the migratory outcome of murine sarcoma cell clusters expressing E-cadherin. (a) Scheme showing the different migratory modes as a function of substrate stiffness. (b) Phase contrast images of murine sarcoma cell clusters expressing E-cadherin on substrates of different stiffness. Adapted from Beaune et al.[143]

In all, the research studies presented above suggest that tissue spreading and migration can be understood by means of a classical wetting paradigm approach. However, these processes require the supply of energy and thus tissues reside in an out-of-equilibrium state, where the active source of tissue contractility and traction forces is not recapitulated explicitly in the cell-substrate adhesion energies of passive wetting processes. In the next section, I will give an overview on a recently proposed theoretical framework to explain tissue expansion and retraction within the newly proposed framework of active wetting.

4.3 Tissue spreading as an active wetting process

As mentioned in the previous section, the cell-substrate and cell-cell interface adhesion energies in theoretical models within the classical framework of wetting do not explicitly incorporate the contribution of the active properties of living tissues. However, the contribution of active parameters such as tractions and contractility can be inferred from experimental data aiming to develop more accurate models of tissue wetting based on active matter.

By combining experimental data with theoretical approaches, Pérez-González et al. reported that tissue expansion and retraction could be modelled using a coarse-grained approach from an active matter perspective, describing the monolayers as 2D active polar fluids, with cells at the periphery polarized outwards. In this polarized region there were two sources of activity: a contractile stress (due to cell-cell pulling forces), which promoted tissue retraction, and a traction force (due to cell-substrate pulling), which promoted tissue spreading. The competition between these two forces gives rise to the active wetting transition, where monolayers larger than a critical size spread or wet, whereas smaller clusters retract or dewet the substrate[117]. Passive cell-cell and cell-substrate adhesion forces were encoded in an effective fluid viscosity and tissue-ECM friction respectively. Remarkably, substrate stiffness is important in determining all the substrate-dependent parameters.

In this study, MDA-MB-231 cells presenting low-expression levels of E-cadherin were transfected with a dexamethasone-inducible vector containing the human E-cadherin coding sequence. Cells were then seeded on size-tunable confined circles functionalized with different concentrations of collagen. The endogenous expression of E-cadherin increased linearly upon the addition of dexamethasone during 24h and reached then a plateau. The increase in E-cadherin expression was paralleled by a 3-fold raise in the di-phosphorylated myosin light chain (ppMLC), resulting in an increase in the overall cell contractility hence enabling tension transmission from the cell-ECM interface to the rest of the tissue through E-cadherin-based junctions.

Cells within the monolayer polarized and aligned radially, whereas traction and tension increased in parallel with the increase in E-cadherin expression. During the experiments, the increase in cell contractility eventually triggered tissue dewetting events by causing a random symmetry breaking in the tractions generated by radially spreading circle-shaped tissues. As predicted by the model, increased substrate stiffness, cell-ECM adhesiveness and tissue size were experimentally reported to favour tissue wetting, whereas increased tissue contractility favoured tissue dewetting[117] (Figure 1-27).
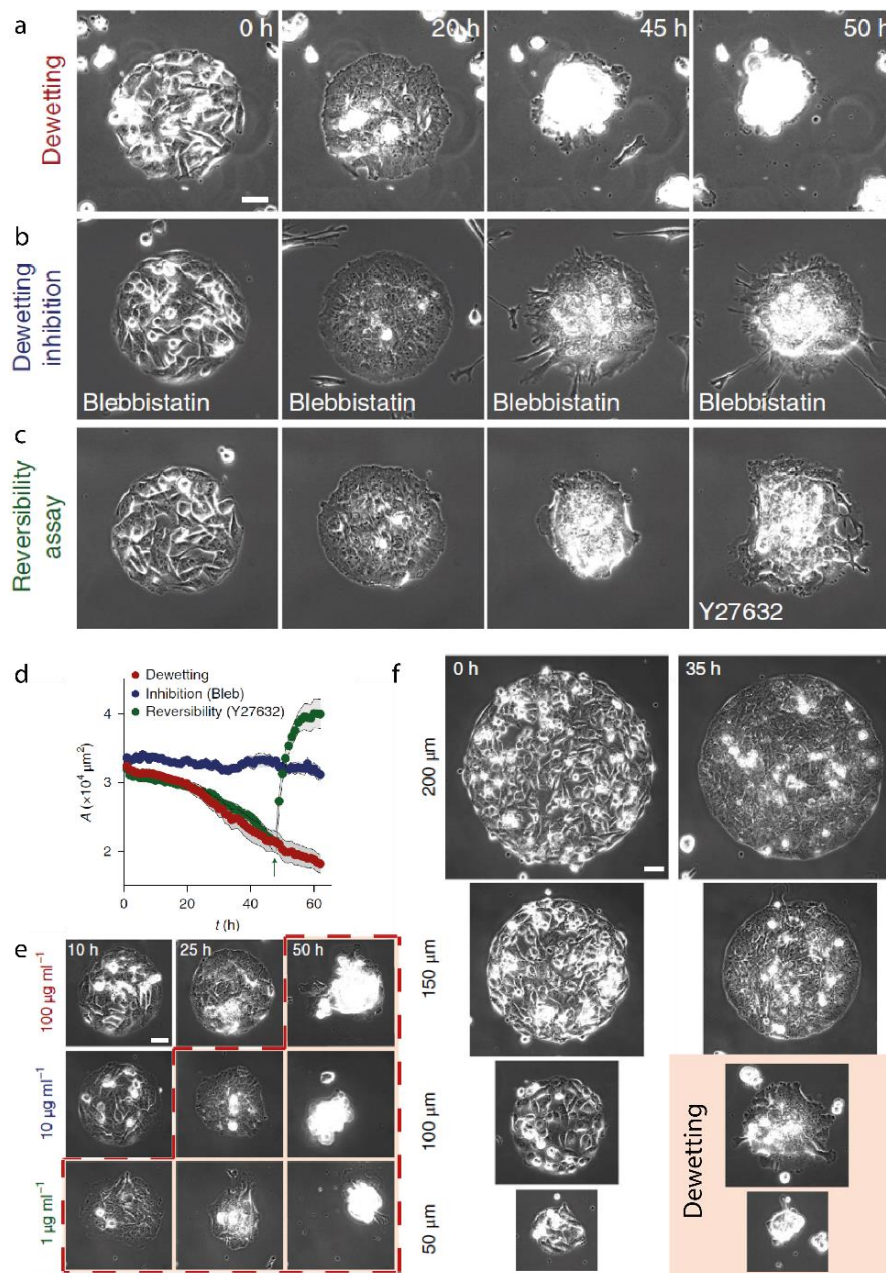
Figure 1-27. Tissue spreading as a function of cell contractility, substrate adhesiveness and tissue size. *(a) A monolayer of MDA-MB-231 cells undergoes an active dewetting event, which is inhibited in the presence of Blebbistatin (b) and can be reversed upon addition of Y-27632 (c). (d) Quantification of monolayer area, which decreases in controls (red, remains constant in the presence of Blebbistatin (blue) and increases upon addition of Y-27632 (green). (e) Active dewetting occurs earlier in non-adhesive substrates. (f) Active dewetting occurs earlier in smaller clusters. Dewetting events are marked in an orange background colour in (e) and (f). Adapted from Pérez-González et al.[117]*

In their work, Pérez-González et al. unveiled fundamental features of tissue wetting that differed qualitatively from the classical wetting paradigm, specifically attributing the wetting properties of tissues to the generation of active cellular forces. Even though other studies modelled tissue expansion in analogy with a fluid wetting its underlying substrate using a framework of adhesion

energies[157,158], this research study constitutes the first subject of work where tissue expansion is explicitly modelled as an active wetting event of a polar fluid[117] (Figure 1-28).
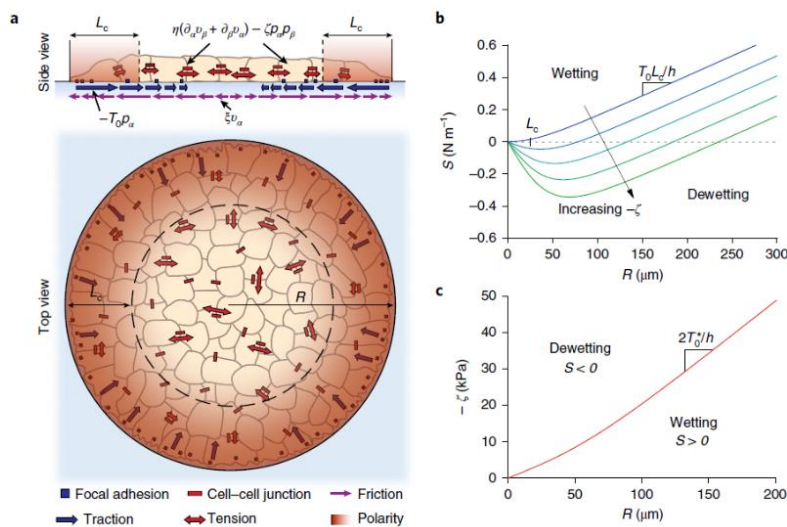
Figure 1-28. Active polar fluid model of tissue wetting. (a) scheme of the model. Traction generated at the monolayer edges as a result of a radially acquired polarity determining a nematic length is transmitted as tension throughout the whole cell monolayer by means of cell-cell junctions. (b) The spreading parameter of a monolayer (S) as a function of tissue size with increasing cell contractility (blue to green), predicted by the model. The point at which S=0 represents the critical radius for tissue wetting on 12 kPa uniform stiffness gels. (c) Predicted critical contractility for the wetting transition as a function of monolayer radius. Adapted from Pérez-González et al.[117]

Additionally, Alert et al. recently published an *in silico* model based in active polar fluids to study the role of substrate stiffness on CCM. Interestingly, their model was adapted to predict collective cell migration on gradients of stiffness, identifying three possible scenarios depending on the intercellular contractility magnitude(60): for small contractility, both edges of the tissue spread but the stiff edge moves faster, resulting in an asymmetric expansion of the tissue; if contractility increases, spreading and retraction can occur simultaneously at the stiff and soft edge respectively, resulting in a net translocation of the tissue; finally, for a sufficiently large contractility, the retraction of both edges takes place with the soft edge moving faster, resulting in the rounding-up and detachment of the tissue. Not only contractility is a key parameter, but also the viscous transmission of forces across the tissue would ultimately drag the soft edge of the cohort of cells towards stiffer regions even if no intercellular contractility is assumed, thus moving against its spreading tendency. In all, the centre of mass of the monolayer is predicted to be always directed towards regions of increasing stiffness[70,145].

The detailed study of durotaxis as a cohort of cells translocating its bulk to a stiffer position than the original has been likely hindered by the high wetting characteristics undergone by tissues in relatively low stiffness migrating on ECM-coated substrates. Interestingly, research studies based on cadherin-coated hydrogels showed that cell spreading was not supported in gels below 30 kPa in stiffness[119]. This finding, together with the fact that E-cadherin regulates cell contractility, made us hypothesize that cell clusters presented with cadherin-coated substrates would experience an active wetting transition at higher stiffness values compared to ECM-coated substrates. Thus, the seeding of clusters on cadherin-coated substrates could potentially enable a detailed study of the active wetting transitions of cellular aggregates. Given the lack of research groups studying cadherin-on-cadherin-

based cell migration, the role of E-cadherin in guiding cell migration besides enabling cell-cell junctions has been largely ignored. In the latter section of this thesis, I present an overview on E-cadherin-mediated cell collective migration events, ultimately raising controversy in proposing stiffness sensing through E-cadherin (possibly in cooperation with other types of cues) as a guiding cue in mechanistically ignored collective migratory processes.

5. E-cadherin-mediated collective cell migration

To date, only a few physiological examples where E-cadherin drives collective cell migration events in environments depleted of ECM have been reported. Most studies featuring collective cell migration have been performed in adult tissues, where cells exhibit both cell-cell and cell-ECM adhesions. The reason behind this experimental bias relies on the technical difficulties related to studying collective cell migration events in contexts lacking ECM, that mainly take place during the early stages of development. Those experiments represent a challenge for scientists, as they imply a higher degree of complexity both in manipulation and measuring techniques, given the size of developing embryos and the few techniques available for *in vivo* force measurements in embryos[67]. Interestingly, E-cadherin has been recently brought to the spotlight as the key protein potentially mediating cell migration in some contexts during development and cancer metastasis[50,53,84,88,103,159–161]. In this section, I will present physiological examples where E-cadherin guides collective cell migration events.

During the early stages of development in *Zebrafish*, ECM is virtually inexistent, whereas the enveloping layer (EVL) and the yolk syncytial layer (YSL) undergo a series of orchestrated cell migration events resulting in the onset of the epiboly[53]. E-cadherin mutation resulting in a hypomorphic allel (thus, partial loss in E-cadherin function due to cdh1[rk3] mutation) led to epiboly arrest in deep cells (DC), a group of cells positioned in between YSL and EVL[162,163]. However, the mechanisms through which E-cadherin enables the collective migration of DC to undergo epiboly are still to be elucidated.
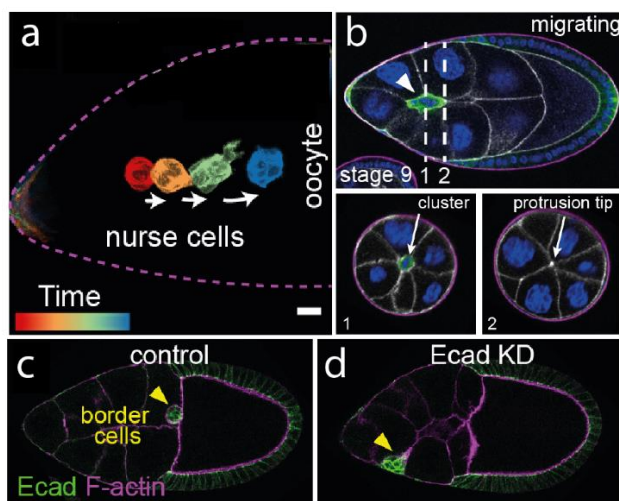
Figure 1-29. Border cell migration in Drosophila melanogaster is E-cadherin-dependent. (a) Temporal color-coded image of border cells migrating in between nurse cells within D. melanogaster oocytes. (b) The chosen path is where multiple nurse cells junctions meet (sectional cut 1), through which border cells extend protrusions (sectional cut 2). (c,d) Border cell migration in controls (c) and E-cadherin KD nurse cells (d) shows that E-cadherin is dependent for border cell migration. Adapted from Dai et al.[161]

Border cell migration in *Drosophila melanogaster* represents another example of E-cadherin-mediated collective cell migration. During *Drosophila melanogaster* oogenesis, a group of cells called border cells delaminate from the follicular epithelium monolayer at the anterior part of the egg chamber and squeeze in between nurse cells in a context lacking ECM[50]. As they delaminate, border cells experience drastic morphology transitions and migrate as a cohesive cluster towards the posterior part of the egg to give rise to a functional oocyte (Figure 1-29). Further research studies found that border cells guide their migration by establishing E-cadherin interactions

at junctures where multiple nurse cells meet, in which tiny openings prior to border cell migration pre-exist. Thus, border cell migration is energetically favoured towards those junctures, minimizing the number of nurse cell adhesions to break during border cell migration[161]. E-cadherin abrogation in either border cells or nurse cells resulted in an impaired migration (Figure 1-29), indicating that E-cadherin plays a role in guiding the migration of border cells[50].

Similarly, E-cadherin has also been reported to be crucial during zebrafish primordial germ cell (PGCs) migration. PGCs migrate through embryonic tissues towards the region where the gonad develops. Although PGCs migrate as single cells guided by chemotactic cues, inhibition of E-cadherin results in a less effective migratory behaviour[160]. Moreover, PGCs migration is impaired upon E-cadherin depletion in the cells that surround the PGCs[160], evidencing that E-cadherin-based adhesions play a role in guiding the migration of PGCs.

To sum up, above are listed known migratory processes where E-cadherin potentially mediates collective cell migration. However, many other early occurring developmental processes involving cell migration might rely on E-cadherin, as differential expression of cadherins leads to embryonic cell segregation[164].

Besides participating in developmental collective cell migration events such as the ones aforementioned, E-cadherin also plays a fundamental role in the context of cancer metastasis, during which single cancer cells and/or clusters of cancer cells that manage to escape the tumour confinement potentially intravasate and later extravasate the bloodstream to ultimately colonize a target organ[83]. Even though E-cadherin is thought to behave as a tumour suppressor protein[165], Padmanaban et al. reported that breast cancers expressing E-cadherin display increased cell proliferation and survival, circulating tumour cell (CTC) number, seeding of cancer cells in distant organs and metastasis outgrowth, compared to genetically modified non-expressing E-cadherin tumours[103] (Figure 1-30). Despite the survival role of E-cadherin in breast cancer metastasis is clear, the mechanisms behind this phenomenology are still to be deciphered. However, given the abundance of different cancer types and their intrinsic heterogeneity, one cannot find a general rule for the role of E-cadherin in cancer metastasis.
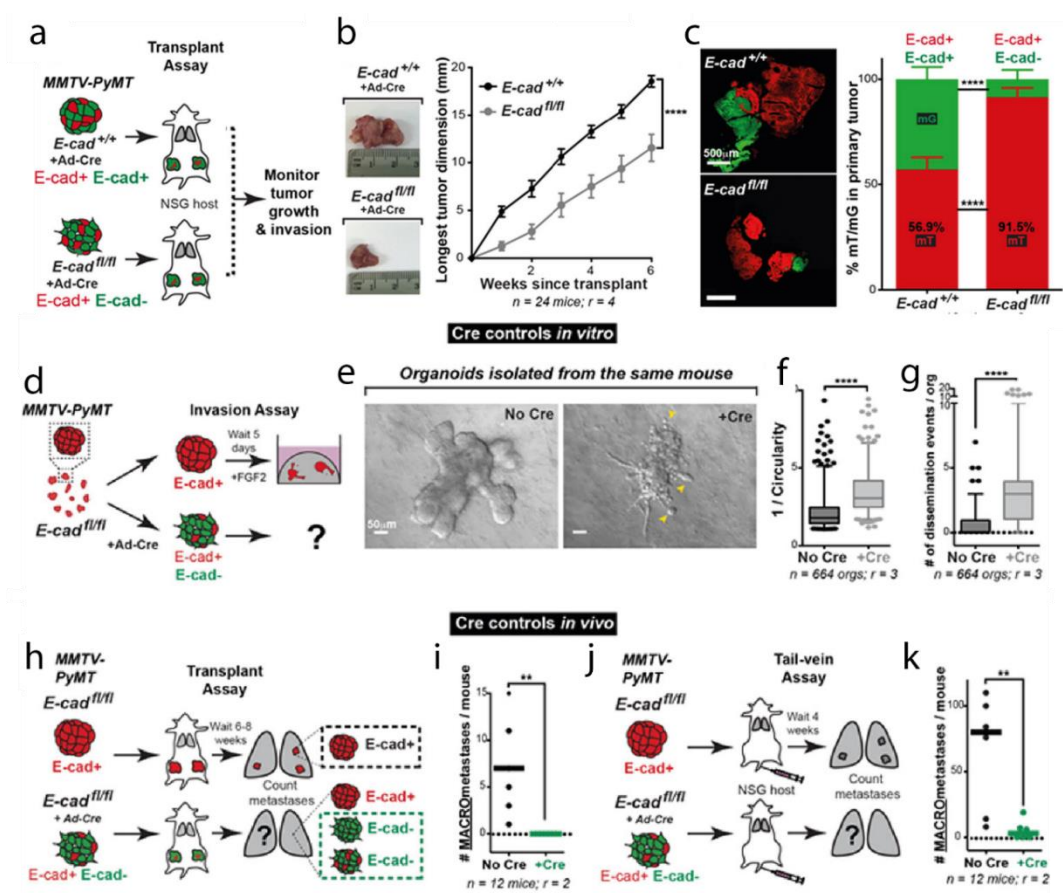
Figure 1-30. E-cadherin plays a crucial role in the contexts of cancer and metastasis. (a) Cartoon illustrating the transplant of either E-cad+/+ or a mosaic of E-cad+/+ / E-cad-/- tumoroids in mice. Tumor growth and invasion were monitored, where the transplanted mosaic tumoroids display smaller sizes than E-cad+/+ tumoroids (b). (c) Tumours in mice transplanted with mosaic tumoroids show a decrease in E-cad-/- cells compared to tumours in E-cad+/+ -transplanted mice. (d) Cartoon depicting the formation of mosaic tumours for its in vitro study. (e) E-cad+/+ tumoroids show a conserved morphology without invadopode-like structures (No Cre), in contrast to mosaic tumoroids (+Cre). (f) Circularity quantification of E-cad+/+ and mosaic tumoroids shows that E-cad+/+ tumoroids are more circular. (g) Mosaic tumoroids display more dissemination events than E-cad+/+ tumoroids. (h) Cartoon depicting E-cad+/+ or mosaic tumoroids transplantation to mice's kidneys. Mice were monitored and potential macrometastases in the lung were quantified. (i) Mice bearing mosaic tumours developed less macrometastases, compared to mice bearing E-cad+/+ tumours. (j) Cartoon depicting E-cad+/+ or mosaic tumoroids transplantation into mice's tails. Mice were monitored as in (h). (k) Mice bearing mosaic tumours developed less macrometastases, compared to mice bearing E-cad+/+ tumours. Adapted from Padmanaban et al.[103]

In all, whereas the examples mentioned above highlight the requirement of E-cadherin for the successful migration and coordination of cohorts of cells during development as well as their survival and metastatic potential in the context of cancer, the mechanisms behind E-cadherin-mediated cell migration remain unclear. One limitation of these studies is that the mechanical properties of ECM-depleted environments are not well characterized. On the one hand, tumours constitute extremely complex and de-regulated contexts featuring high heterogeneity as to adhesome expression, matrix deposition and activated signalling pathways[166]. On the other hand, the mechanical properties of developing embryos, potentially constituting the other scenario where E-cadherin could mediate migration, have been scarcely studied. This problem has recently been overcome with the emergence

of *in vivo* stiffness measuring techniques in embryos(128,153), which could potentially shed light on migratory processes during development whose driver is largely unknown.

In this line, Zhu et al. developed a magnetic device to perform 3D stiffness mapping in embryos that enabled them to report the presence of a stiffness gradient paralleled with the emergence of the mouse limb bud in a fibronectin-dependent manner(128), indicating that gradients of stiffness could be the drivers of cell migration even during early stages of development. This assumption is consistent with a recently published study showing that *in vivo* durotaxis allows for the correct migration of the neural crest during *Zebrafish* development[52].

In summary, the current knowledge on cadherin-based cell-cell adhesions is robust enough for us to hypothesize that cadherin-mediated stiffness sensing might be key to some developmental and pathological processes. In this thesis, we show that E-cadherin mediates the collective durotaxis of A431 cell clusters in an active wetting transition-dependent manner. Importantly, we propose a theoretical framework based in active gels to explain collective cell durotaxis as a function of cell contractility, traction forces, local stiffness, surface tension, tissue viscosity and friction, whose interplay directly affects the wetting state of migrating epithelial cell clusters. Finally, we report that this phenomenology also arises in epithelial cell clusters migrating on fibronectin-coated gradients of stiffness, suggesting a general mechanism where stiffness sensing becomes optimal for clusters in the vicinity of an active wetting transition.

2. **Aims**

1. To functionalize mechanically tuneable polyacrylamide gels with oriented E-cadherin

   1.1. To validate the functionalization protocol

   1.2. To assess the specificity of cell adhesion on E-cadherin-coated gels

2. To characterize the dynamics of A431 cell clusters seeded on uniform stiffness E-cadherin gels

   2.1. To study the collective migration of A431 clusters seeded on E-cadherin gels of different stiffness

   2.2. To quantify the contact angle θ and the 3D shape of A431 clusters seeded on E-cadherin gels of different stiffness

   2.3. To study the generation of traction forces by A431 clusters seeded on E-cadherin gels

3. To adapt the E-cadherin-coating protocol developed in the Aim 1 to functionalize polyacrylamide stiffness gradients

   3.1. To characterize how gel stiffness and slope depend on the fabrication parameters

   3.2. To quantify the variation of protein incorporation in regions of different stiffness

4. To study durotaxis of A431 clusters migrating on E-cadherin-coated gels with stiffness gradients

   4.1. To study the effect of stiffness, cluster size, stiffness slope and cell contractility on cluster durotaxis

5. To explain the migratory behaviour of A431 clusters within the novel framework of active 3D wetting

   5.1. To explain the 3D geometry of the clusters using a surface tension parameter

   5.2. To explain the durotaxis of A431 clusters on E-cadherin-coated stiffness gradients

   5.3. To explore if this interpretation could be generalized to migration mediated by other adhesion proteins such as fibronectin

51

3. Materials and Methods

Cell culture techniques

Cell maintenance

A431 cells were cultured in Dulbecco's Modified Eagle's Medium containing high glucose and pyruvate (11995, Thermofisher) supplemented with 10% fetal bovine serum, 100 units·ml^{-1} penicillin and 100 µg·ml^{-1} streptomycin, cultured in a humidified atmosphere containing 5% CO_2 at 37ºC. Cells were starved for 24 hours in starvation media (Dulbecco's Modified Eagle's Medium containing high glucose and pyruvate supplemented with 1% FBS, 100 units·ml^{-1} penicillin and 100 µg·ml^{-1} streptomycin) prior to experiments. Versene (15040066, Gibco) was used to collect cells from flasks as a non-enzymatic cell dissociation reagent aiming to preserve membranal E-cadherin integrity prior to cell seeding on gels functionalized with E-cadherin.

Cell clusters formation

A431 cell clusters were obtained by seeding $5·10^3$ cells/well in Corning Costar Ultra-Low Attachment Multiple Well Plate (CLS3474-24EA) in starvation media. 24 hours later, clusters were mechanically disaggregated into smaller clusters exhibiting heterogeneous sizes by pipetting up and down with a series of pipette tips of different sizes. Cellular debris was discarded by centrifuging disaggregated clusters at 0.3 rpm for 0.5 min.

Cell clusters seeding

Cell clusters were resuspended in media containing 5 µM Rho/ROCK pathway inhibitor (Y-27362) and seeded on stiffness gradients in a total volume of 50 µL to allow for cluster adhesion to the entire surface of the gels, thus covering the whole range of stiffness in a gradient. 45 minutes later, 1 mL of media containing 5µM Rho/ROCK pathway inhibitor (Y-27362) was added to prevent the gels from drying out. 30 min later, Y-27362 was carefully removed by slow aspiration and 1.5mL of fresh starvation media was added. Clusters were imaged 2 hours later after cluster contractility was fully recovered.

Lentiviral transfection for stable Lifeact-mCherry expression

HEK293T cells were transfected as previously described[168] to produce lentiviral particles inducing stable expression of Lifeact-mCherry. A431 wild type cells were infected as previously described[168]. Two weeks later, infected cells were sorted using an ARIA fluorescence-activated cell sorter (BD) aiming to select those cells exhibiting similar fluorescence intensity.

Cell adhesion assay

A431 cells were resuspended at a concentration of 10^6 cells/mL and incubated for 15min in ice-cold starvation media containing either 40 μg/mL α-GFP antibody (A10262, Life technologies; Control) or 40 μg/mL DECMA-1 antibody (U3254, Sigma Aldrich). Cells incubated with control or DECMA-1 antibody were seeded on gels functionalized with E-cadherin. Cell adhesion was allowed for 15min before gently washing three times with 1xPBS containing calcium and magnesium, and the remaining adhered cells were fixed with 4% PFA in 1xPBS containing calcium and magnesium, followed by Hoesch staining for nuclei quantification. An inverted microscope (Nikon Eclipse Ti) equipped with a 2x 0.06NA objective was used to image the entire gel surface. An intensity threshold was set on FiJi software to binarize the images and automatically count the number of adhered cells per condition. The cell density of Control and DECMA-1 groups was compared through non-parametric statistical tests.

Contractility enhancement and inhibition experiments

To study the effect of contractility on cluster migration, 0.5 μM Y-27632 ROCK inhibitor (Merck, 688001) and 1.65 nM human epidermal growth factor (hEGF, Peprotech AF-100-15) were used to inhibit and enhance cell contractility, respectively.

Histidine-tagged GFP and histidine-tagged mCherry production and purification

Histidine-tagged GFP and histidine-tagged mCherry were produced in *Rosetta E. coli* strain and purified using Ni-NTA columns, as previously described[169].

Preparation of polyacrylamide gels

Glass-bottom dish silanization

Glass-bottom dishes (P35-0-20, Mattek) were silanized using a 2:1:80 solution of acetic acid/bind-silane (M6514, Sigma)/ethanol for 30 min. The dishes were washed twice with ethanol and dried by aspiration.

Uniform stiffness polyacrylamide gels

1 mL gel premix solution containing 2% bis-acrylamide and 40% acrylamide (proportions vary according to desired stiffness; see Table 3-1), 15μL irgacure 5% w/v (BASF, Germany), 6 μL acrylic acid

(147230, Sigma Aldrich), 102 µL 1M NaOH and 10 µL 500nm-diameter yellow-green fluorospheres (F8813, Thermofisher) was prepared. A drop of 16 µL of gel premix was added to the center of the previously silanized glass-bottom dish, and an 18-mm diameter glass coverslip treated with Repel Silane (General Electric, USA) was placed on top to distribute the volume evenly and flatten the gel surface. Glass-bottom dishes containing a "sandwich" of gel premix were placed under UV light (lamp XX-15L series, Black Ray 15W, UVP) for 5min to allow for gel polymerization. Next, a solution of 10x PBS was added to facilitate coverslip peel off. Round-tip tweezers were used to separate top coverslips from the gels polymerized on glass-bottom dishes.

Stiffness (kPa)	40% Acrylamide (µL)	2% Bis-acrylamide (µL)
0.2	100	30
1	87	33
6	187	70
24	244	125
200	480	187

Table 3-1. Stiffness and corresponding Acrylamide/Bis-acrylamide concentrations for 1mL gel premix.

Stiffness gradient polyacrylamide gels

A 25µL drop of gel premix containing 15% acrylamide, 1% bis-acrylamide, 0.75 mg·mL^{-1} irgacure, 0.60% acrylic acid (v/v), 100mM NaOH and a dilution of 1:100 from stock of 500nm-diameter fluorescent beads (F8813, Thermofisher) was added to the center of previously silanized glass-bottom dishes and covered with an 18mm-diameter glass coverslip treated with Repel Silane (General Electric, USA). Gradients of stiffness on polyacrylamide gels were obtained as previously described[170,171]. Briefly, making use of an opaque sliding mask during UV-triggered gel polymerization we polymerized gels exhibiting a gradient of stiffness. To obtain "shallow" and "steep" gradients, the opaque mask was moved at rates of 50 µm·s^{-1} and 30 µm·s^{-1}, respectively, and UV-mediated gel polymerization was allowed for 4 min. Finally, 10xPBS was added to facilitate the removal of top coverslips using round-tip tweezers. Gel stiffness was measured with AFM after every experiment.

Gel functionalization with oriented E-cadherin

To functionalize uniform and stiffness gradient gels we used a previously described method involving carbodiimide reactions[172] (See Appendix 1). Briefly, a mix of 20 mM NTA-NH$_2$ and 25 mM CuSO$_4$ in 1xPBS buffer was brought to pH=10.0 and centrifuged at 4500 rpm for 15min. The pellet was discarded while the supernatant (formed by a solution containing NTA-NH$_2$/Cu^{2+}) was brought to pH=7 and filtered using a 0.20 μm diameter filter. In parallel, previously polymerized polyacrylamide gels were incubated with 100mM EDC and 200mM NHS in 20mM Hepes pH=7.0 buffer at 37ºC for 20min. Then, gels were quickly washed twice with 1xPBS and incubated at 37ºC with filtered NTA-NH$_2$/Cu^{2+} solution aiming to bind it covalently to carboxyl groups on the gel surface. Two washes with 1xPBS were performed 45min later, followed by addition of 1M Tris pH=8.0 for 30min to hydrolyze unreacted active carboxyl groups. Next, the gels were washed twice with 1xPBS and incubated at room temperature with a drop of 25μL of 0.01mg·mL^{-1} histidine-tagged E-cadherin (8505-EC-050, R&D Systems) covered with rectangles of parafilm, ensuring an even distribution of the drop across the entire surface of the gel. E-cadherin orientation through ionic bindings on the gel was achieved after 1 hour of incubation, and excess E-cadherin were rinsed with two washes of 1xPBS. Then, gels were incubated with 50mM EDC and 75mM NHS in 20mM pH=7.0 Hepes buffer at 37ºC for 45 min aiming to covalently bind E-cadherin to the gels. Next, the gels were washed twice with 1xPBS and incubated with 1M imidazole/1mM EDTA in PBS for 20min to chelate copper ions and thus rinse non-covalently bound E-cadherin, followed by two 1xPBS washes. Finally, gels were passivated with 0.1 mg·mL^{-1} pLL-g-PEG and used for experimental purposes within 24h after the functionalization process.

Gel functionalization with fibronectin

Polyacrylamide gels were functionalized performing carbodiimide reactions. Briefly, gels were incubated with 100 mM EDC and 200 mM NHS in 20 mM Hepes pH=7.0 buffer at 37ºC for 20 min. Next, gels were quickly washed twice with 1xPBS and incubated at 37ºC with a dilution of 0.1 mg/mL fibronectin (33016015) in 1xPBS for 45 min. Finally, gels were washed twice with 1xPBS and incubated with 1M Tris pH=8.0 for 30 min at RT, followed by two 1xPBS washes. Gels were kept overnight at 4ºC prior to UV-sterilization and cluster seeding.

Protein incorporation quantification in polyacrylamide gels

To study the protocol's functionalization efficiency, histidine-tagged E-cadherin was replaced by Histidine-tagged GFP/mCherry, whose functionalization and orientation are achieved likewise, offering a direct fluorescence readout for the protocol validation. Aiming to provide a realistic idea of

the extent of protein incorporation, their molar concentrations were normalized. Fluorescence images were taken from functionalized gels using an inverted microscope (Nikon Eclipse Ti) equipped with a 10x 0.30 NA objective (for stiffness gradient gels) or a 20x 0.45 NA objective (for uniform stiffness gels). Briefly, 3 images covering approximately the first 3 mm of stiffness gradients from the soft edge were stitched, followed by fluorescence normalization and quantification for every gradient tested.

Imaging techniques

Time lapse microscopy

Multidimensional acquisition routines were performed on automated inverted microscopes (Nikon Eclipse Ti) equipped with thermal, CO_2 and humidity control using MetaMorph, Micromanager and NIS-Elements softwares. Time-lapse experiments started approximately 4h after cell seeding. The image acquisition interval was set to 10 min, and a typical experiment was run for more than 10 h. Images were acquired using a 10x 0.3 NA objective, and an automated stage was used to save 3 overlapping stage positions that covered approximately 3 mm of the stiffness gradients starting from the soft edge.

High-resolution images of cell clusters

An inverted Nikon microscope equipped with a spinning disk confocal module (CSU-WD, Yokogawa) was used to acquire high resolution images of A431 mCherry-Lifeact cell clusters seeded at different stiffness. A z-step equal to 0.2 µm was acquired for every cluster, ensuring to capture whole cell clusters.

Traction force microscopy

Traction forces were computed using Fourier transform based traction microscopy with a finite gel thickness as previously described[173]. Gel displacements experienced between any experimental timepoint and a reference image of the relaxed state of beads after cluster trypsinization were computed using home-made particle imaging velocimetry software[173]. Traction forces in xy were plotted in overlapping fluorescent images, whereas orthogonal traction forces in z were represented by averaging the value of 10 traction pixels along the represented lines within the x and y axis.

Stiffness gradient profile measurement with Atomic Force Microscopy

Stiffness gradients and uniform stiffness gels were mapped individually using a commercial Atomic Force Microscope (AFM) (JPK Nanowizard, Germany) operated as previously described[174,175]. Briefly, a V-shaped cantilever (Bruker) with a triangular tip and a spring constant of k = 0.03 N·m^{-1} was used to indent the gels to ensure the cantilever deflection resulted within the linear detection range of the AFM. The cantilever spring constant was calibrated using a thermal fluctuation method. The relationship between the photodiode signal and cantilever deflection was computed from the slope of the force displacement curve obtained at a region without gel sample. For each sample, 5 force-displacement (F-z) curves (where F= k·d, d being the deflection and z being the piezotranslator position) were acquired by ramping the cantilever forward and backward at a constant speed (5 µm amplitude, 1 Hz and approximately 1 µm of indentation). Each experimental F-z curve was fitted to the four-sided pyramidal indenter model:

$$F = \frac{E \cdot \tan \theta}{2^{1/2} \cdot (1 - v^2)} \cdot \delta^2,$$

where E is the Young's modulus, v is the Poisson's ratio, θ is the semi-included angle of the pyramidal indenter and δ is the indentation depth. Following previous studies[39], the parameter v is assumed to be 0.5, and the indentation depth is calculated as δ = $z - z_0 - d$, where z_0 is the tip-gel contact point. E and z_0 were estimated by least-squares fitting of this equation to the F-z curve recorded on each gel point. Young's modulus was measured every 200 µm along the axis of maximum gel stiffness change.

Analysis techniques

Contact angle measurement

To compute the contact angle θ formed between the substrate and the line tangent to the edge of the cluster (Figure 4-7 a) we acquired high resolution stacks of mCherry-Lifeact A431 cell clusters seeded on 0.2, 1, 6, 24 and 200 kPa E-cadherin-coated polyacrylamide gels (the z-step was 0.26 µm after correcting for the focal plane shift). Figure 3-1 shows the basic strategy used to calculate the contact angle as a function of the cluster radius (R_{sphere}), the contact radius (R) and the cluster height (H). For dewetted clusters, we estimated R_{sphere} from the maximum z projection of all the images (R_{proj}) in the stack and R from the basal plane (Figure 3-2 a). Then, the contact angle was given by $\theta = 180 -$

$asin\left(\dfrac{R}{R_{\text{sphere}}}\right)$. For wetted clusters, we estimated R_{sphere} from the height H and R (Figure 3-2 b). Both

H and R were obtained from the z stack. Then, the contact angle was given by $\theta = asin\left(\dfrac{R}{R_{\text{sphere}}}\right)$.
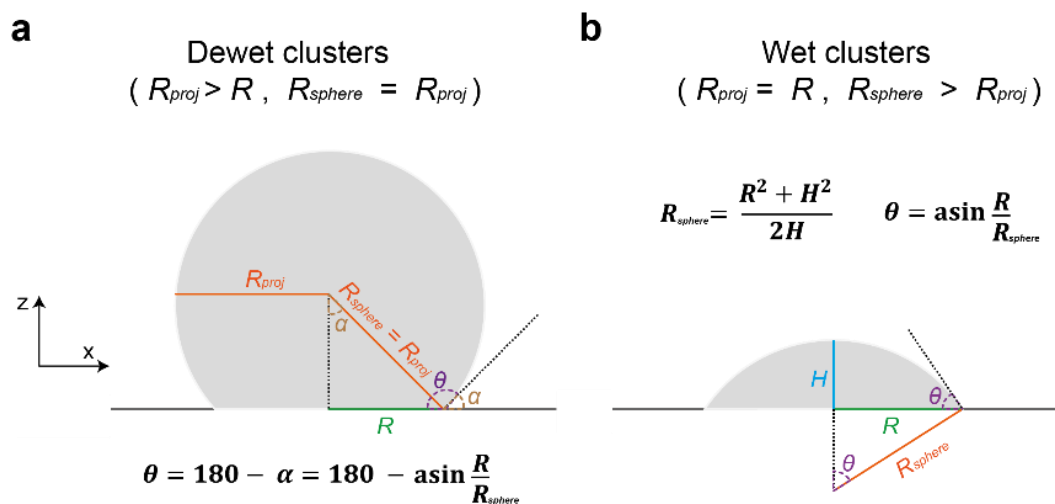
Figure 3-2. Contact angle (θ) measurement as a function of cluster radius (R_{sphere}), contact radius (R) and cluster height (H). *The calculation varied for dewet (a) and wet (b) clusters. All parameters were estimated from high resolution z-stacks of LifeAct-mCherry A431 clusters seeded on E-cadherin substrates.*

Cluster tracking using phase images

Custom-made Matlab scripts combined with "Grid/Collection stitching" plug-in from FiJi software were used aiming to register and stitch three overlapping images covering 3 mm of the stiffness gradients. Briefly, time-lapse images from the green fluorescent channel containing fluorescent beads (F8812, ThermoFisher) were registered using a custom-made Matlab script. "Grid/Collection stitching" plugin from FiJi was used to stitch registered maximum intensity images from fluorescent beads, and a custom-made matlab script was run to stitch phase contrast images using the xy coordinates provided by FiJi.

Stitched phase contrast images were used to segment clusters. Images were treated with gaussian and standard deviation filters to find cluster edges. After applying automatic thresholding and detection algorithms we detected cluster position. Clusters were linked based on proximity, and tracks were generated and labelled with increasing numbers. Segmented images with cluster labels were merged with phase contrast images, and clusters were manually selected using the label number. Inconsistently tracked and incorrectly segmented clusters were discarded for analysis. Clusters whose tracks left the field of view were kept until the timepoint in which their outline merged with the image

boundary, whereas clusters whose tracks interacted were kept until the timepoint in which the interaction took place. Final tracks contained the x and y coordinates for each cluster at the measured timepoints. Noise in trajectories was estimated at 1.5 μm by tracking pieces of immobile debris.

Image processing of high-resolution images of clusters

Acquired images of mCherry-Lifeact A431 cell clusters were processed using Imaris software. A gaussian filter to the images was applied aiming to smoothen the fluorescence signal before generating a surface to visualize the tridimensional shape of clusters.

Statistics

Statistical analyses and plotting were performed using R v 4.0.3 (R Core Team). 95% confidence intervals of medians were estimated using bootstrap intervals of 10,000 resamples. Whenever data followed a non-normal distribution (according to Shapiro-Wilk normality test), analyses were conducted using non-parametric permutation and bootstrapping tests (R-MKinfer library).

4. Results

1. Validation and specificity of E-cadherin coating protocol

First, we adapted a previously published protocol to functionalize glass surfaces with oriented E-cadherin[122] to functionalize polyacrylamide gels. Since carboxyl groups were required for the functionalization protocol, acrylic acid was added to the gel premix prior to gel polymerization, as described in the Materials and Methods chapter.
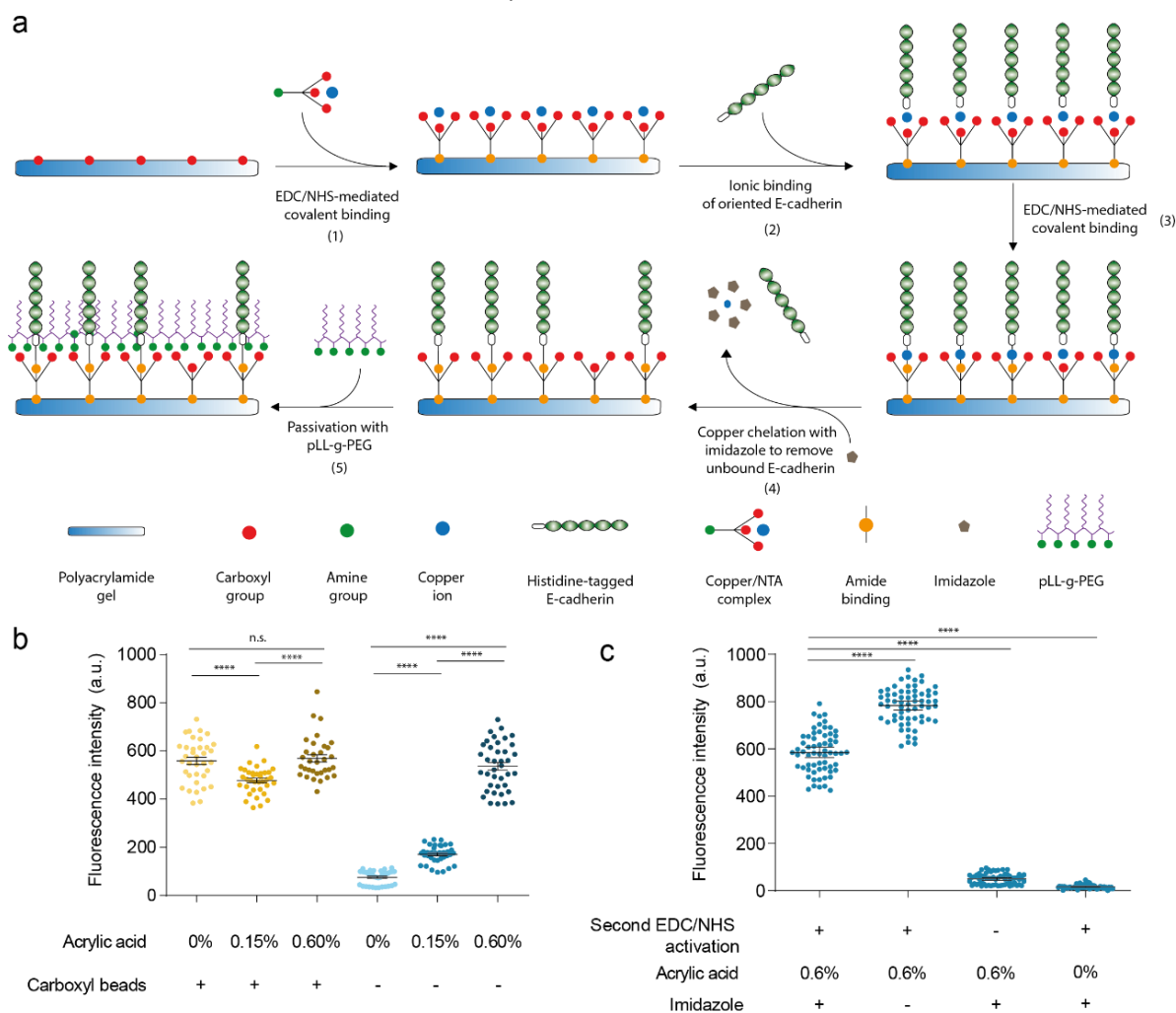
Figure 4-2. Functionalization of polyacrylamide gels with oriented E-cadherin extracellular domains (EC1-5). (a) Scheme showing the protocol to covalently attach E-cadherin fragments on the surface of a polyacrylamide gel. Briefly, polyacrylamide gels containing acrylic acid and thus presenting free carboxyl groups were activated with EDC/NHS and incubated with a solution of NTA/Cu^{2+} complexes (step 1) aiming to form a covalent amide bond between carboxyl groups in the gels and amino groups from NTA/Cu^{2+} complexes. Next, gels were incubated with histidine-tagged E-cadherin extracellular domains EC1-5 (step 2), which spontaneously oriented along NTA/Cu^{2+} complexes through their histidine tag. A covalent amide bond between histidine-tagged E-cadherin extracellular domains EC1-5 and NTA/Cu^{2+} complexes was formed upon a second round of EDC/NHS activation (step 3). Finally, imidazole was used to rinse non-covalently bound histidine-tagged E-cadherin fragments and Cu^{2+} (step 4) prior to gel passivation with pLL-g-PEG (step 5). Histidine-tagged E-cadherin was replaced by histidine-tagged mCherry in (b) and (c) as a direct readout of protein incorporation to assess the yield of the protocol. (b) Fluorescence intensity as a readout of protein incorporation in polyacrylamide gels with varying acrylic acid concentration (row 1) containing (+) or lacking (-) carboxyl beads (row 2). (c) Fluorescence intensity as a readout of protein incorporation in polyacrylamide gels lacking carboxyl beads, including (+) or omitting (−) steps in the protocol. First row indicates whether gels underwent a second EDC/NHS treatment to covalently bind E-cadherin to the gels; second row indicates concentration of acrylic acid; third row indicates whether gels were rinsed with imidazole to remove non-covalently histidine-tagged mCherry. Each point in (b) and (c) represents the fluorescence quantification of one field of view. n ≥ 33 (b), n ≥ 60 (c). Bars in (b) and (c) indicate mean ± 95% CI. Non-parametric Mann Whitney tests were performed (**** indicate p-value < 0.0001).

We functionalized polyacrylamide gels of uniform stiffness with oriented E-cadherin extracellular domains (from now indistinctively referred to as E-cadherin or EC1-5) using a series of bivalent ion chelation and carbodiimide reactions (Figure 1 a). Briefly, we made use of carbodiimide reactions (mediated by EDC/NHS) to functionalize polyacrylamide gels containing acrylic acid with NTA/Cu^{2+}. Next, we incubated the gels with E-cadherin, which oriented spontaneously through a histidine tag-mediated Cu^{2+} chelation, followed by a second EDC/NHS activation to covalently bind E-cadherin to NTA. Then, we incubated the gels with imidazole to rinse Cu^{2+} along with non-covalently-bound E-cadherin. Finally, pLL-g-PEG mediated the passivation of E-cadherin-coated polyacrylamide gels (Figure 4-1 a).

Aiming to obtain a readout of E-cadherin functionalization of polyacrylamide gels, we replaced histidine-tagged E-cadherin by histidine-tagged mCherry, thus providing a direct fluorescence readout of protein incorporation, as the functionalization of substrates with both histidine-tagged E-cadherin and histidine-tagged mCherry rely on the same protocol. Whereas no correlation between protein incorporation and acrylic acid concentration was observed in polyacrylamide gels containing carboxyl groups, protein incorporation in polyacrylamide gels lacking carboxyl beads increased with increasing carboxyl groups provided by varying concentrations of acrylic acid (Figure 4-1 b).

Next, aiming to evaluate the yield of the functionalization with the developed protocol, we functionalized polyacrylamide gels lacking carboxyl beads omitting different steps in the protocol, as shown in (Figure 4-1 c). As expected, protein incorporation was very low either in the absence of acrylic acid or upon imidazole rinse in the absence of a second EDC/NHS activation. These results indicate that carboxyl groups are required for the functionalization of polyacrylamide gels with oriented E-cadherin, whereas the second round of EDC/NHS activation covalently binds oriented histidine-tagged mCherry to polyacrylamide gels. Also, the fact that protein incorporation decreased upon imidazole rinse in the presence of a second EDC/NHS activation indicates that imidazole incubation successfully rinses non-covalently bound histidine-tagged mCherry. In all, here we report that polyacrylamide gels were successfully functionalized with oriented E-cadherin making use of their histidine tag's chelation properties.

Even if substrates are coated with E-cadherin, cells can secrete ECM and form adhesions with it, which could impair a clear interpretation of our results. To assess this potential limitation, we screened four cell types (MDCK, MCF 10A, A431 and C2C12) on either fibronectin or E-cadherin-coated polyacrylamide gels and stained paxillin (Figure 4-3). Across all the cell lines tested, we selected the A431 cell line for further experiments due to the absence of large FA-like complexes on E-cadherin-

coated polyacrylamide gels . To avoid the problem of ECM deposition, we focused our experiments on the shortest possible time window after seeding.
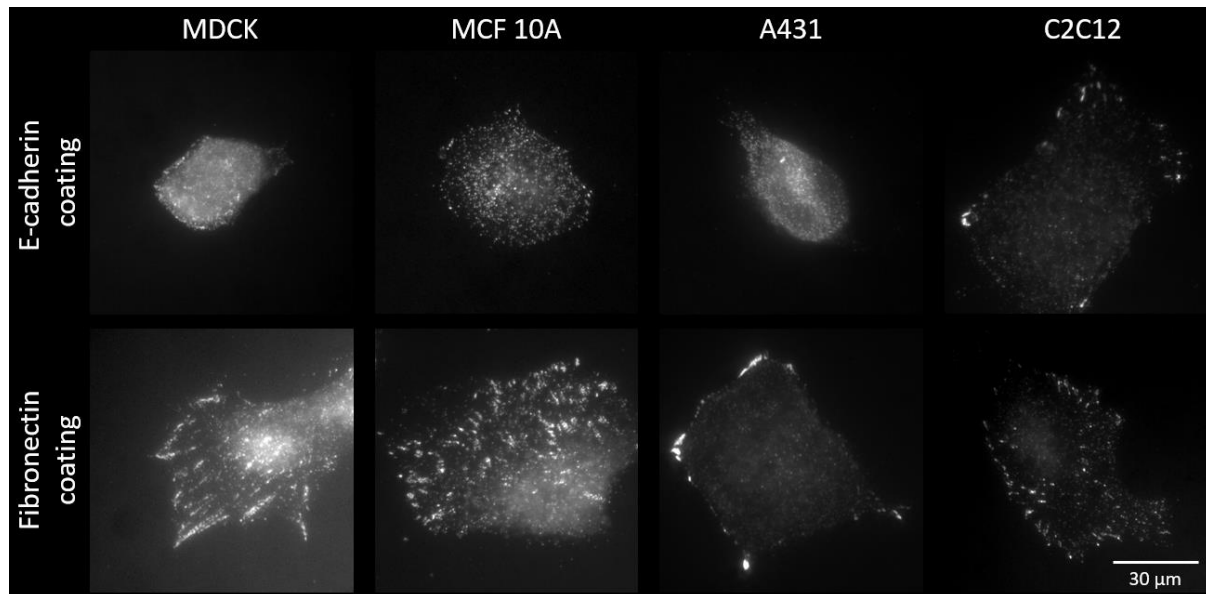
Figure 4-3. Cell lines screening. *MDCK, MCF 10A, A431 and C2C12 cells were seeded on 30 kPa polyacrylamide gels functionalized either with E-cadherin or fibronectin, fixed 24 hours later and stained against phospho-paxillin in a screening aiming to choose the cell line for further experiments.*

Next, aiming to assess the specificity of the adhesions made by A431 cells on E-cadherin-coated polyacrylamide gels, we performed 3 control experiments, as shown in Figure 4-4.

Firstly, we made use of an E-cadherin-blocking antibody (DECMA) aiming to impair the adhesion of A431 cells on E-cadherin-coated substrates, as explained in the Materials and Methods chapter. As shown in Figure 4-4 a, a decreased cell density count was reported in DECMA-treated cells, compared to controls.

Secondly, we performed a morphology assessment in A431 genetically modified cells seeded on E-cadherin-coated gels lacking essential proteins involved in the formation of cadherin-based adhesions. As shown in (Figure 4-4 b), both 5 and 24 hours after A431 cell seeding, wild type cells displayed more membrane protrusions, compared to either alfa-catenin KO or E/P-Cadherin KO A431 cells, which displayed a rounder shape. Additionally, wild type A431 cells formed cell aggregates 24 hours after cell seeding, whereas alfa-catenin and E/P-cadherin KO cells displayed a rounder morphology and didn't form cell aggregates.

Finally, we performed immunostainings as explained in the Materials and Methods chapter aiming to study the type of adhesions formed by A431 cells on E-cadherin-coated substrates. To this end, p-paxilin and E-cadherin were immunostained. Interestingly, we found that focal adhesions only formed

on fibronectin-coated substrates (red arrows, Figure 4-4 c). Also, an accumulation of E-cadherin was observed in the periphery of A431 cells on E-cadherin-coated substrates.
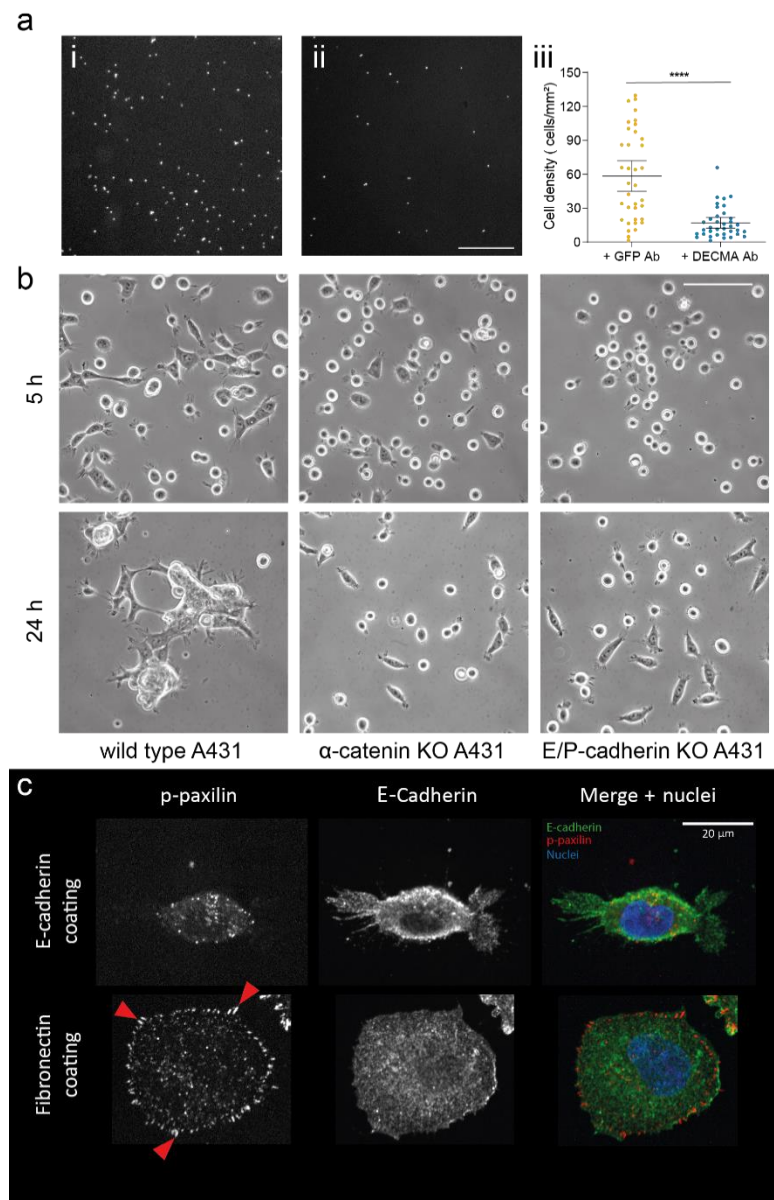
Figure 4-4. The adhesions made by A431 cells on E-cadherin-coated polyacrylamide gels are E-cadherin-dependent. *(a) A431 cells were incubated with DECMA antibody as explained in the Materials and Methods chapter. Representative images of the nuclei (labelled with Hoechst) of cells attached in controls (i) and DECMA-treated cells (ii). (iii) Cell density count in controls and DECMA condition (Each dot represents the cell density in one field of view. n= 36 in each condition (4 fields of view per gel, with a total of 9 gels per condition). Data is mean ± 95% CI). Mann Whitney tests were performed (**** indicate p-value < 0.0001) (b) Representative phase contrast images of wild type, alfa-catenin KO and E/P-Cadherin KO A431 cells seeded on 30 kPa E-cadherin-coated polyacrylamide gels after 5 and 24 h. (c) Representative immunostaning examples performed in single A431 cells seeded either on E-cadherin-coated or fibronectin-coated polyacrylamide gels at t= 10 h. P-paxilin, E-cadherin and the nuclei were stained as explained in the Materials and Methods chapter. Red arrows point at focal adhesions made on fibronectin-coated polyacrylamide gels (Green: E-cadherin; Red: phospho-paxilin. Blue: Nuclei -labeled with Hoechst).*

Taken together, these results indicate that A431 cells form specific E-cadherin-based adhesions with the developed E-cadherin-coated polyacrylamide gels. We next proceeded to study the migration, morphology and traction forces of A431 cell clusters on E-cadherin-coated polyacrylamide gels.

2. A431 cell cluster dynamics, morphology and traction forces on E-cadherin-coated polyacrylamide gels of uniform stiffness

We first studied the spontaneous migration of A431 cell clusters on polyacrylamide gels of uniform stiffness functionalized with oriented E-cadherin (Figure 4-5 a, b). A431 cell clusters were generated as explained in the Materials and Methods chapter, seeded on E-cadherin-coated polyacrylamide gels of uniform stiffness (0.2, 6, 24 and 200 kPa) and tracked with a custom-made algorithm for a minimum of 14 hours at 10 min intervals. The dependence of cluster velocity with stiffness was biphasic (Figure 4-5 d): cluster velocity was minimal at low stiffness (0.2 kPa), peaked at intermediate stiffness (24 kPa) and finally decreased at high stiffness (200 kPa). Cluster persistence followed the same behaviour, peaking at intermediate stiffness (6 and 24 kPa) (Figure 4-5 e).
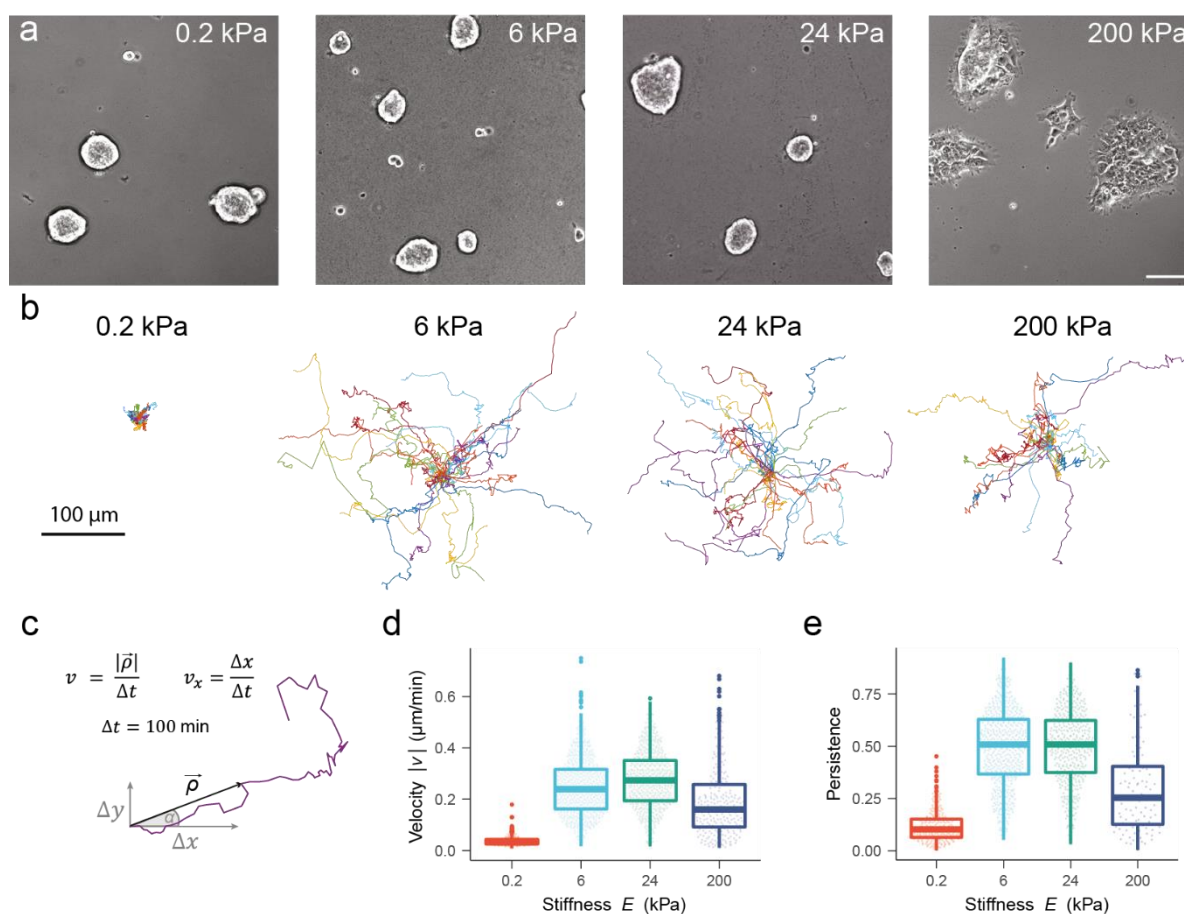
Figure 4-5. A431 cell cluster velocity and persistence show a biphasic dependence with stiffness. *Representative phase contrast images of A431 cell clusters seeded on E-cadherin-coated uniform-stiffness gels of 0.2, 6, 24 and 200 kPa. Scale bar, 100 µm. (b) Representative trajectories of clusters migrating on the E-cadherin-coated gels shown in panel (a). Timepoints were acquired every 10 min. (c) Cartoon representing the workflow to track cluster trajectories, velocity and persistence. Velocity and persistence were computed at 100 min intervals. (d) Cluster velocity at different substrate stiffness. (e) Cluster persistence at different substrate stiffness. Each dot in (d) and (e) represents 1 cluster. For the sake of visualization, points represented are within the percentile 99.5%. n ≥ 266 clusters. Kruskal-Wallis tests were performed, where all groups displayed significant differences in (d). No significant differences were observed between 6 and 24 kPa in (e).*

Since the biphasic behaviour of cluster velocity with stiffness seemed to correlate with different regimes of cluster spreading (Figure 4-5 a), we next acquired high resolution confocal images of A431 cell clusters transfected with LifeAct-mCherry seeded on E-cadherin-coated polyacrylamide gels of varying stiffness to study the wetting state of clusters (Figure 4-6). Cluster spreading increased with stiffness, where clusters displayed a virtually non-spread state on 0.2 kPa and a highly spread state on 200 kPa E-cadherin-coated polyacrylamide gels. We thus interpreted A431 cell cluster spreading within the conceptual framework of active wetting, in line with previously published studies[117].
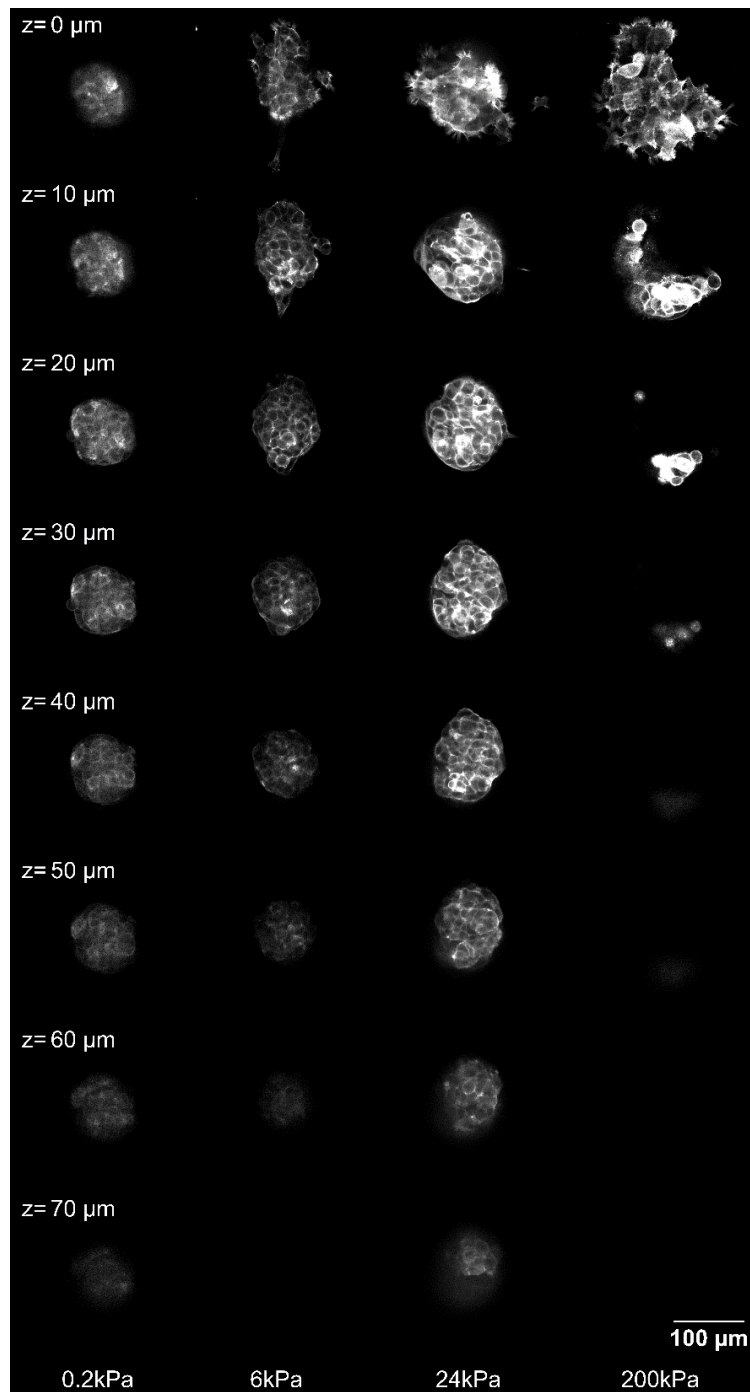
Figure 4-6. 3D cluster profile. *Z-stack of A431 clusters expressing LifeAct-mCherry seeded on 0.2, 6, 24 and 200 kPa uniform stiffness gels coated with E-cadherin. Slices are shown with a z-step size of 10 µm. Basal plane is z = 0.*

We next quantified the contact angle θ formed between the line tangent to the edge of A431 cell clusters and E-cadherin-coated polyacrylamide gels of different stiffness (Figure 4-7) to better characterize the wetting state of clusters, as explained in the Materials and Methods chapter.
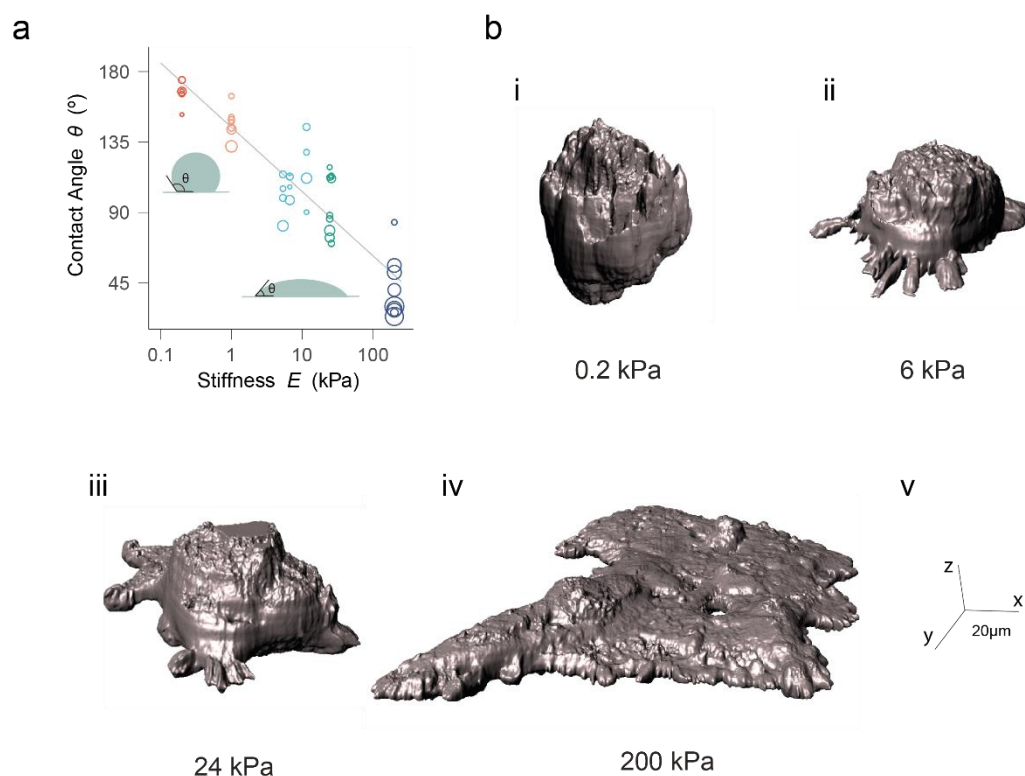
Figure 4-7. A431 cell clusters actively dewet soft and wet stiff E-cadherin-coated gels, respectively. *(a) Measurement of the contact angle formed between the substrate and the line tangent to the edge of clusters on different substrate stiffness (see the Materials and Methods chapter). Each dot is the averaged contact angle for 1 cluster. Circle size is proportional to cluster average diameter. n= 43 clusters. (b) 3D rendering of clusters seeded on different substrate stiffness. (i: 0.2 kPa, ii: 6 kPa, iii: 24 kPa, iv: 200 kPa, v: lines in the reference tridimensional axes represent 20 µm.*

At low stiffness, clusters were nearly spherical and the contact angle θ between the substrate and the line tangent to the edge of the cluster was close to 180º, indicating full dewetting (Figure 4-6, Figure 4-7 a, b-i). By contrast, at high stiffness, clusters spread to form a monolayered epithelium with a low contact angle θ, indicating a high wetting state (Figure 4-6, Figure 4-7 b-iv). At intermediate stiffness, the contact angle θ was close to 90º, and hence the tissue is close to the active wetting transition that was defined in the introduction between monolayer spreading and retraction[117]. In this regime, clusters displayed highly dynamic protrusions (Figure 4-6, Figure 4-7 b-ii/iii, Supplementary video 1, Supplementary video 2). Aiming to better characterize these protrusions, we imaged clusters transfected with actin mCherry-Lifeact at high spatial and temporal resolution. The resulting movies revealed that membrane protrusions were dynamic filopodia (Supplementary video 3), in which actin flowed retrogradely towards the core of the clusters (Supplementary video 4). Taken together, these data suggest that at the proximity of a wetting transition, clusters become motile by rapidly assembling and disassembling actin-rich protrusions with the substrate.

Next, we examined whether these local protrusions generated traction forces. We performed 3D

Traction Force Microscopy (TFM) experiments on clusters seeded on polyacrylamide gels of 1 and 6

kPa in stiffness (Figure 4-8). At higher stiffness, TFM showed insufficient resolution to robustly

measure the three components of tractions. We characterized traction profiles through their radial

component, defined as the component perpendicular to the cluster edge in the xy plane, and through

the normal component to the substrate in the z axis (Figure 4-8 c). Both on 1 kPa and 6 kPa substrates,

radial tractions pointed towards the center of the cluster (Figure 4-8 a,b). Also, radial tractions were

higher on 6 kPa gels and decreased from the cluster edge towards its core (Figure 4-8 d). Normal

tractions were positive near the cluster edges and became negative towards the cluster core in both

stiffnesses (Figure 4-8 e). These data indicate that the cluster surface tension pulls the cluster edge

upwards at the contact line with the substrate. Consistent with this picture, cell protrusions at the

edge often formed acute angles with the substrate (Figure 4-6, Figure 4-7). Upwards traction at the

cluster edge is balanced by a pressure that pushes the cluster core into the substrate. As commonly

seen in single cells seeded on ECM and E-cadherin coated substrates, traction forces increased with

substrate stiffness (Figure 4-8 d,e).
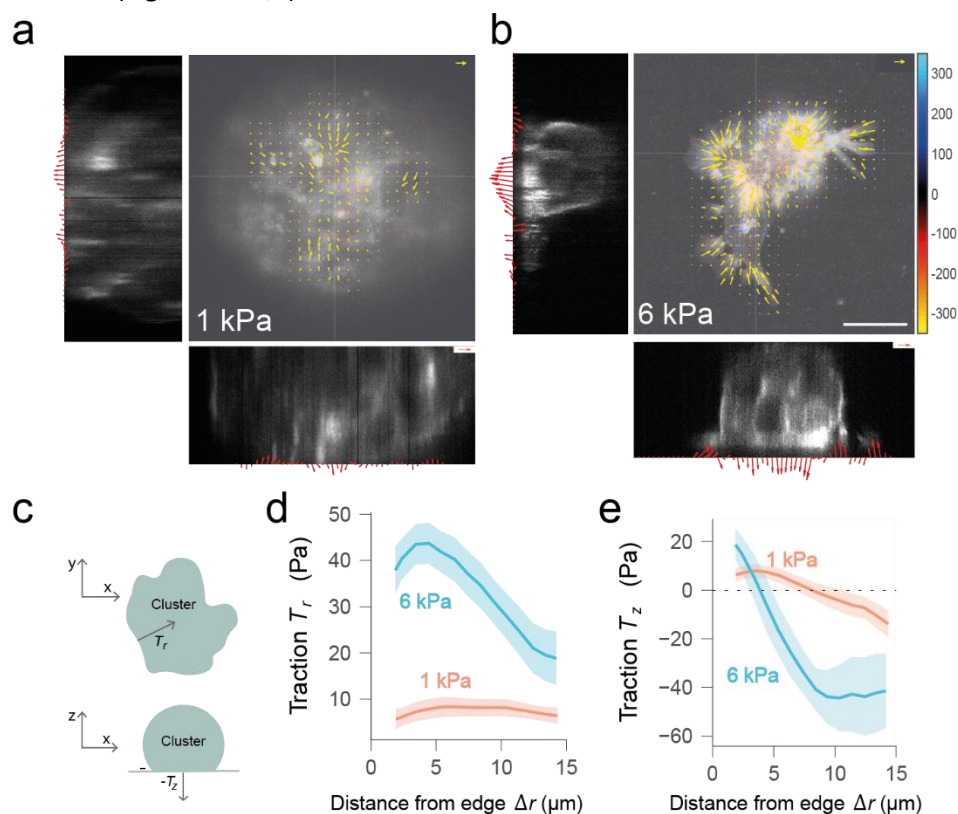
Figure 4-8. Normal and radial traction forces exerted by clusters on E-cadherin-coated uniform stiffness polyacrylamide gels increase with stiffness. (a, b) Traction forces exerted by representative clusters on 1 and 6 kPa E-cadherin-coated gels. Yellow vectors represent traction forces in the xy-plane whereas red vectors represent traction forces projected on the corresponding lateral planes (xz and yz) along the gray lines shown in the central panels (reference vectors are 50 Pa, scale bar is 25 µm). (c) Cartoons depicting radial and normal traction forces. (d) Average of the radial projection of traction forces in the xy-plane for 1 (orange) and 6 kPa (blue) gels as a function of distance from cluster edge. n ≥ 19 clusters. (e) Average of the vertical component of the force for 1 (orange) and 6 kPa gels (blue) as a function of distance from cluster edge. n ≥ 7 clusters.

3. Clusters migrating on E-cadherin-coated substrates display robust durotaxis

The increase in A431 cluster's traction forces with stiffness on E-cadherin-coated gels, together with the highly dynamic state of epithelial clusters close to the active wetting transition led us to hypothesize that they might be particularly responsive to gradients in substrate stiffness.

In order to test this hypothesis, gradients of stiffness with different slope were polymerized and measured by atomic force microscopy (AFM) as described in the Materials and Methods chapter. The resulting gradients of stiffness were functionalized as in (Figure 4-1) with histidine-tagged mCherry to rule out a possible effect of stiffness-dependent protein incorporation (Figure 4-9).
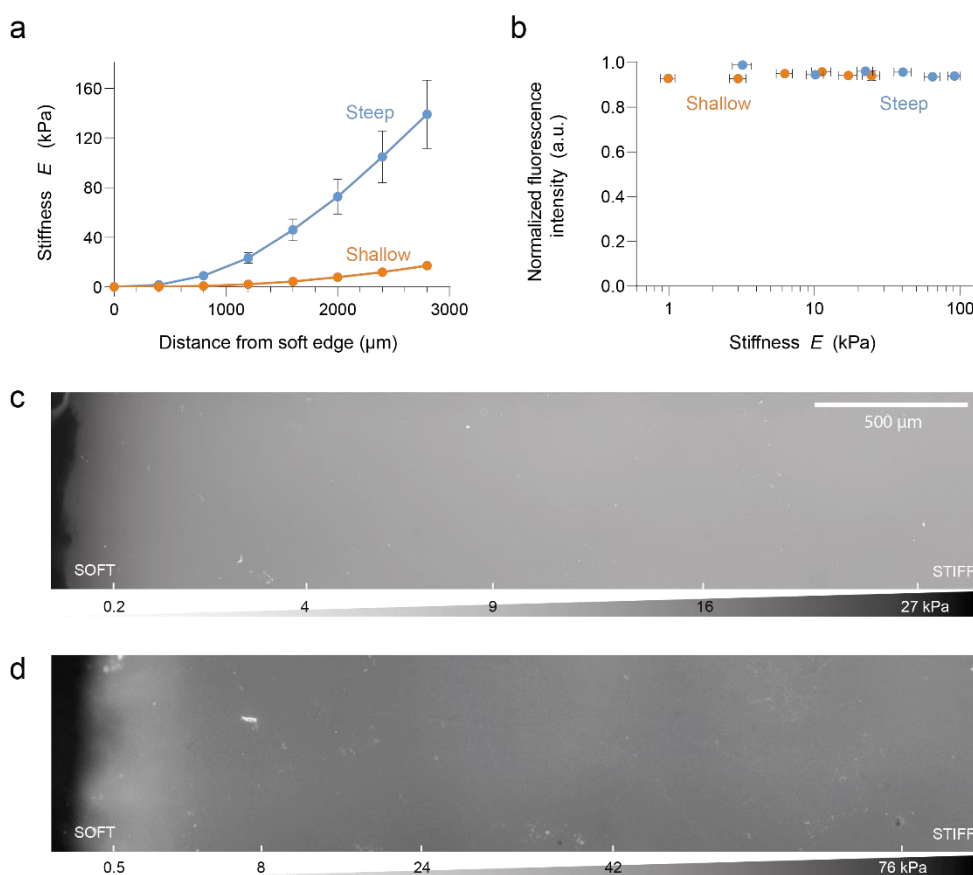
Figure 4-9. Stiffness profile and protein incorporation on shallow and steep gradients of stiffness. (a) Stiffness profiles of steep (n=12, blue) and shallow (n= 13, orange) gradients as a function of distance from soft edge of gradient measured by AFM. (b) Normalized histidine-tagged mCherry intensity signal as readout of protein incorporation as a function of stiffness for shallow (orange) and steep (blue) gradients of stiffness. (c,d) Representative fluorescence images of shallow and steep gradients of stiffness functionalized with histidine-tagged mCherry, respectively. Soft edge is to the left, measured stiffness is indicated below.

Approximately, the first 3 mm of the stiffness gradients starting from the soft edge were imaged and measured by AFM (Figure 4-9 c, d). Within this distance, polyacrylamide gels covered a range of stiffness up to 135 ± 30 kPa and 22 ± 4 kPa in steep and shallow gradients (mean ± SE), respectively

(Figure 4-9 a). We then quantified histidine-tagged mCherry incorporation in steep and shallow gradients of stiffness, which we found to be independent of substrate stiffness (Figure 4-9 b, c, d).

Next, we functionalized steep and shallow gradients of stiffness with oriented E-cadherin, followed by A431 cell cluster seeding to study durotaxis. Clusters were tracked as explained in (Figure 4-5 c) for a minimum of 14 hours at 10 min time intervals (Figure 4-10 a). Using this approach, we built a large dataset matching the local mechanical properties of the substrates with the migratory data for each cluster and time point. In order to estimate cluster durotaxis, we quantified cluster velocity parallel to the gradient of stiffness (v_x), which was not significantly different from 0 for clusters seeded on uniform stiffness E-cadherin-coated gels. In contrast, v_x was higher than 0 for clusters seeded on gradients of stiffness (Figure 4-10 b), indicating that A431 cell clusters displayed robust durotaxis when seeded on E-cadherin-coated gradients of stiffness.
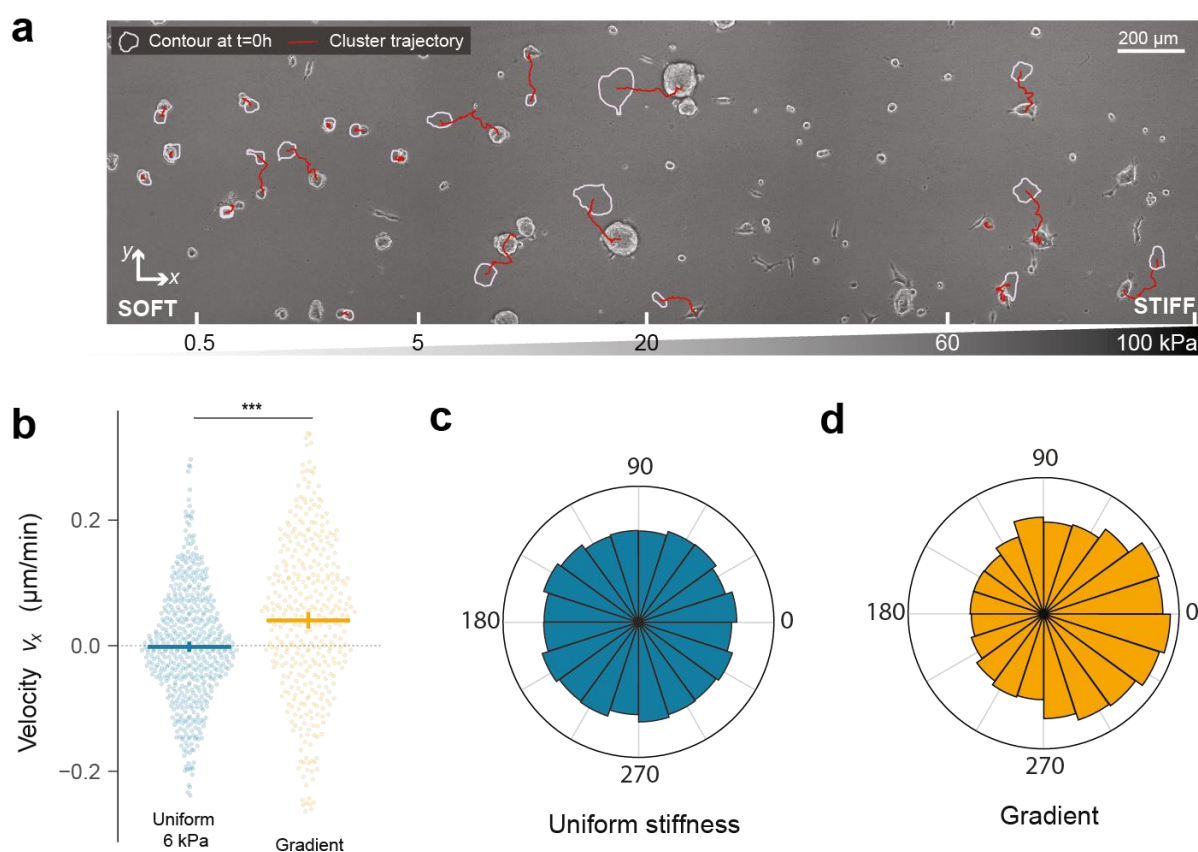
Figure 4-10. Differential active wetting enables collective durotaxis. *(a) Representative phase-contrast image of A431 cell clusters migrating on a stiffness gradient coated with E-cadherin. Image was taken at 10h. The original position (0h) of each cluster is represented by a purple outline. The red line represents the trajectory obtained by time-lapse microscopy. Bottom scale indicates the stiffness at each point of the image. (b) Cluster velocity on uniform and gradient stiffness gels. Horizontal bars represent mean ± 95% CI. Each dot represents a cluster. n ≥ 366 clusters. *** indicates p-value < 0.001 (Permutation tests were performed). (c-d) Distribution of the angle α between the instantaneous velocity vector and the x-axis (see Figure 4-5 c) for uniform stiffness gels (c) and stiffness gradients (d).*

This biased migration was also evident when comparing the angular distribution (depicted in Figure 4-5 c) of cluster trajectories for uniform (Figure 4-10 c) and gradients of stiffness (Figure 4-10 d) coated with E-cadherin. These experiments show that durotaxis is not restricted to integrin mediated migration on ECM substrates. Rather, the cell migration machinery can drive durotactic responses through cadherin receptors.

To characterize durotaxis, we studied the role of local substrate stiffness, cluster size, cell contractility and stiffness slope.

We first explored whether durotaxis depended on local substrate stiffness E. Like for substrates of uniform stiffness, clusters dewetted regions of low stiffness and wetted those of high stiffness (Figure 4-10 a, Supplementary video 5). In these two extreme cases, cluster durotaxis was low (Figure 4-11 a). However, in regions of intermediate stiffness, clusters were found to be close to the wetting transition and durotaxis peaked (Figure 4-11 a, Supplementary video 6). Thus, the stiffness dependence of cell dynamics on substrates of uniform stiffness was recapitulated on stiffness gradients (Figure 4-5), but migration was directed towards regions of higher stiffness rather than following random motions.
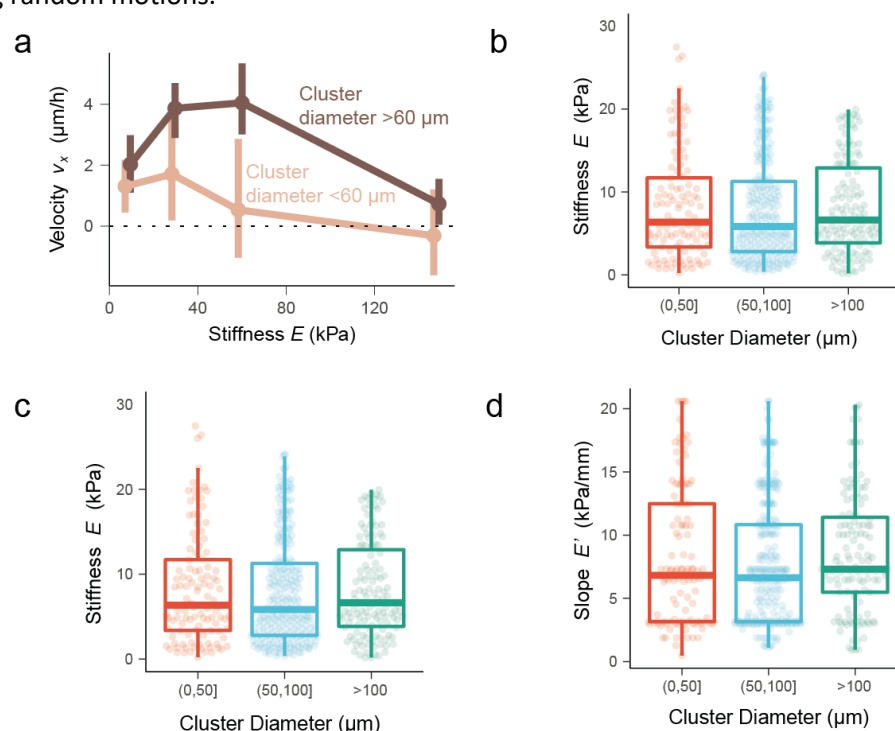
Figure 4-11. Cluster durotaxis depends on local stiffness and cluster size. (a) Cluster durotaxis (assessed by the median velocity along the x-axis obtained from the analysis of individual displacements of clusters seeded on E-cadherin-coated steep gradients of stiffness) as a function of local stiffness and cluster size. Light brown indicates cluster velocity along the x-axis (v_x) for small clusters (diameter < 60 μm), whereas dark brown shows cluster velocity (v_x) for big clusters (diameter > 60 μm). Vertical bars indicate 95% interval confidence. n ≥ 136 cluster displacements per stiffness bin. (b) Cluster velocity v_x as a function of cluster size for clusters seeded on shallow gradients of stiffness coated with oriented E-cadherin. Each point represents a cluster. Vertical bars represent 95% CI. n ≥ 102 clusters per bin. Small sized clusters (<50 μm group) are less durotactic than large sized clusters (>100 μm group, p-value < 0.01, permutation t-test). All these three groups display a similar local stiffness (c) and stiffness slope (d).

73

We next studied the role of cluster size on cluster durotaxis on steep gradients of stiffness functionalized with oriented E-cadherin. We found that durotaxis of clusters depended on the local stiffness, with larger clusters (diameter > 60 µm) durotaxing more efficiently than smaller clusters (Figure 4-11 a). Also, the peak in durotaxis for small clusters (diameter < 60 µm) took place at stiffness below 40 kPa, whereas the durotactic peak of large clusters was higher in magnitude and took place at around 40-80 kPa in stiffness (Figure 4-11 a).

An additional analysis of the effect of cluster size on cluster durotaxis was performed in shallow gradients of stiffness, where clusters did not fully wet the stiff regions. We report that cluster durotaxis on those gradients also increased with cluster size (Figure 4-11 b), with all size groups showing no differences with local stiffness (Figure 4-11 c) or stiffness slope (Figure 4-11 d).

Next, in order to study the role of cell contractility in cluster durotaxis, we treated A431 cell clusters with a low dose of ROCK inhibitor (0.5 µM Y-27632). We found that, in large clusters, a decrease in contractility reduces durotaxis and shifts the durotactic peak to lower stiffness compared to untreated clusters (Figure 4-12 a, Supplementary video 7). Finally, to study whether durotaxis depended on stiffness slope, we segmented our large data set in regions of low, middle, and high steepness. Since durotaxis depends on local stiffness ofset, we measured cell velocity on each gradient substrate for a fixed substrate stiffness (18 ± 5 kPa, Figure 4-12 c). We found that clusters located at larger slopes showed significantly more durotaxis than clusters located on milder slopes (Figure 4-12 b).
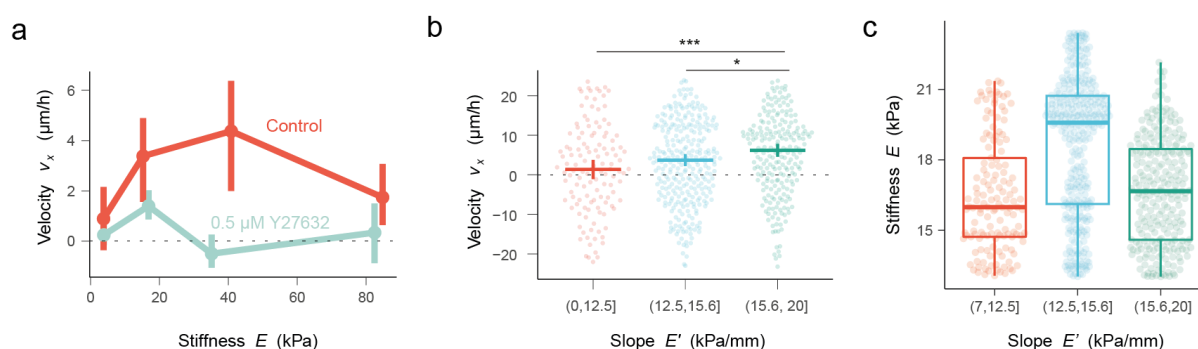
Figure 4-12. Cluster durotaxis depends on cell contractility and stiffness gradient slope. (a) Cluster durotaxis as a function of cell contractility and local stiffness. Data comes from clusters > 60 µm. Vertical bars represent 95% interval confidence. n ≥ 69 cluster displacements per stiffness bin. (b) Velocity along the gradient (v_x) grouping cluster displacements that occurred in different gradient slopes. Each data point represents a cluster displacement. n ≥ 141 cluster displacements. Permutation tests were performed. (c) Corresponding stiffness distribution for each grouped slope in (b).

Taken together, these results establish a mode of durotaxis that is optimal in the vicinity of an active wetting transition and depends on cluster size, contractility, stiffness and stiffness gradient.

4. An active polar fluid model of tissue wetting describes cluster migration and durotaxis

So far, our data has established that the peaks in cluster speed and durotaxis correlate with the wetting state of the cell clusters. To understand how the tissue wetting properties might lead to collective durotaxis, we collaborated with Irina Pi-Jaumà (UB), Ricard Alert (MPI) and Jaume Casademunt (UB) to model clusters as active fluid droplets that partially wet the substrate. Accordingly, we describe a cluster as a spherical cap of radius R_{sphere}, whose contact surface with the substrate is a circular cell monolayer of radius R (**Figure 4-13** a). We assume that the dynamics of the droplet is controlled by the in-plane forces in this basal monolayer, which we model as a 2D active polar fluid, extending previous work [70,117,144,176]. The cells at the periphery of this monolayer are polarized outwards and exert two types of active forces (**Figure 4-13** a, inset): cell-substrate traction with a maximum value ζ_i, which promotes tissue spreading, and cell-cell contractility with magnitude $\zeta < 0$, which promotes tissue retraction. Previous work showed that the competition between traction and contractility in this 2D model gives rise to an active wetting transition between monolayer spreading (wetting) and retraction (dewetting)[70,117,144].

Here, we extend the theory of active wetting to 3D droplets (Appendix 2). We propose that the equilibrium droplet shape, and hence its contact angle θ, are determined by a generalized Young-Dupré force balance between the active forces in the basal cell monolayer and the out-of-plane surface tension γ of the cell cluster (**Figure 4-13** a, Appendix 2). The horizontal component of the surface tension, $-\gamma/R \, \cos\theta$, combines with the monolayer active forces to drive either spreading or retraction, damped by both monolayer viscosity η and substrate friction ξ. For sufficiently large γ, this tissue reaches a state of partial wetting with either high ($\theta < 90º$) or low ($\theta > 90º$) wettability (Appendix 2). Because it lacks a horizontal component of surface tension, the equilibrium state with $\theta=90º$ corresponds to the active wetting transition in the 2D model. In turn, the vertical component of surface tension is balanced by the Young-Laplace pressure $P = 2\gamma/R_{sphere}$ exerted on the contact surface (**Figure 4-13** a). We use this relation to infer the value of γ in our experiments from measured vertical traction forces (**Figure 4-8**), which provide a direct measurement of P (Appendix 2).

To capture collective durotaxis, we take into account that cellular forces depend on substrate stiffness. Following previous work[70,77,177–181], we assume that both the active traction ζ_i and the friction coefficient ξ increase and saturate with the substrate's Young modulus E. This is consistent with our measurements, which show that radial in-plane tractions increase with substrate stiffness (**Figure 4-8**). In addition, our measurements reveal that out-of-plane tractions also increase with stiffness (**Figure**

4-8), implying that the tissue surface tension features an active mechanosensitive response[182,183]. Consistently, we assume that the tension γ, and thus the pressure P, are increasing functions of E, which we take as linear for simplicity. Altogether,

$$\zeta_i(E) = \zeta_i^\infty \frac{E}{E + E^*}, \quad \xi(E) = \xi^\infty \frac{E}{E + E^*}, \quad \gamma(E) = \gamma_0 + \ell_\gamma E,$$

where ζ_i^∞ and ξ^∞ are saturation values, E^* is a characteristic stiffness of force saturation, γ_0 is the bare surface tension, and ℓ_γ is a length associated with its mechanosensitive response.

Irrespective of the wettability of the 3D droplet, the balance of in-plane forces at the basal monolayer yields two basic predictions. First, as predicted by Alert et al.[70], the durotactic velocity v_x increases with the difference between the active traction at the front (stiff edge) and at the rear (soft edge) (Appendix 2). Hence, v_x increases with the stiffness gradient, consistently with our measurements (Figure 4-12). Second, at high stiffness, active traction forces saturate, and friction increases. As a result, the durotactic velocity decreases at high stiffnesses (Figure 4-13 b), which explains our experimental measurements (Figure 4-11). Figure 4-13 b shows that this slowdown at high stiffnesses can arise either at $E > E^*$ due to traction saturation, or at $E < E^*$ due to increased friction.

However, our experiments also show that the durotactic velocity v_x increases at low stiffness, which is not accounted for by the 2D force balance only (Figure 4-11). Using our 3D active wetting theory, we predict that this feature arises from the wettability of the tissue. Consistently with our measurements (Figure 4-7), at low stiffness we find that the tissue has low wettability (θ>90º, Figure 4-13 c). As a result, the contact radius R is small (Figure 4-13 a). This leads to a small active traction difference across the tissue, and hence a small durotactic velocity. Also consistent with experiments (Figure 4-7), wettability increases at higher stiffness, yielding larger contact areas and hence faster durotaxis. This velocity increase at low stiffness is thus controlled by all the forces that determine the contact angle. For example, as it promotes dewetting, higher contractility yields higher contact angles (Figure 4-13 c), and hence slower durotaxis. In contrast, as the contact angle is higher than 90° at low stiffness, surface tension points outward, favouring spreading (Figure 4-13 a left). Therefore, increasing surface tension , for example by increasing stiffness or pressure sensitivity to stiffness, yields smaller contact angles and hence faster durotaxis (Figure 4-13 d). Altogether, the combined effects of three-dimensional active wetting and the saturation of cellular forces at high stiffness explain why the durotactic velocity first increases and then decreases with substrate stiffness (Figure 4-13 b, d), as observed in our experiments (Figure 4-11).
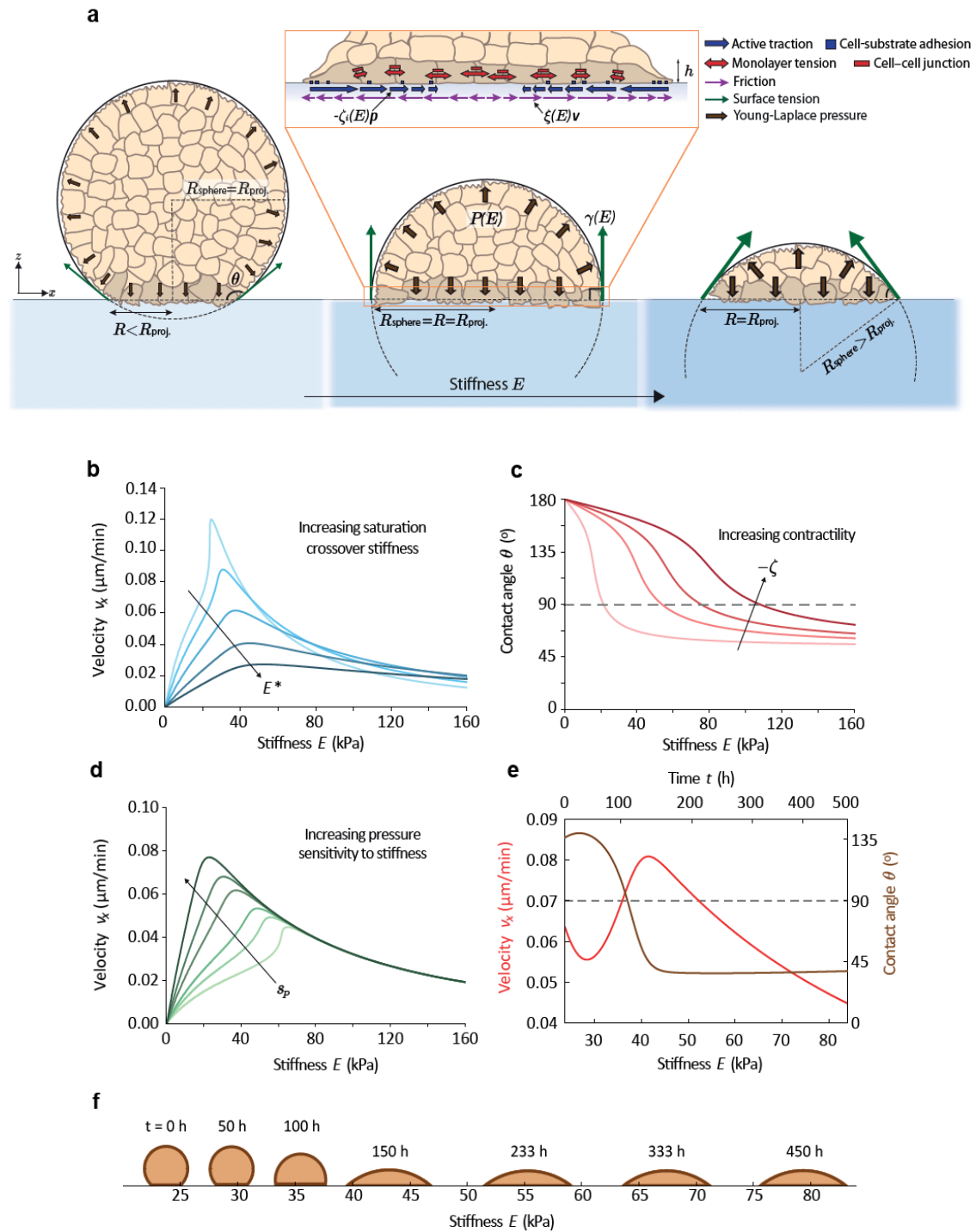
Figure 4-13. A three-dimensional model of active wetting explains non-monotonic tissue durotaxis. *(a) Scheme of the model for a cell cluster with a constant projected radius R_{proj}, placed on different substrate stiffness E. R_{proj} is the experimentally measured size, which coincides with the contact radius only for clusters with low contact angles ($\theta \leq 90^\circ$). (a, inset) Zoom-in of the basal monolayer in contact with the substrate (represented with darker cells for visualization), where the interfacial cell-substrate forces and cell-cell tension are drawn. (b) Non-monotonic behaviour of the durotactic velocity v_x with stiffness, for a constant R_{proj} cluster (see Methods). For large stiffness magnitudes, the decrease is governed by the saturation crossover stiffness E^* (here $E^* = 50,80,140,260,450$ kPa from lighter to darker blue, and $s_P = 4.52 \cdot 10^{-2}$ is fixed). (c) Equilibrium contact angle θ of a fixed-volume droplet on mono-stiffness substrates, from which we vary the stiffness. Different curves show how an increasing contractility maintains the clusters with a higher contact angle for higher stiffness (here $-\zeta = 2,5,7,10$ kPa, from lighter to darker red). (d) Non-monotonic behaviour of the durotactic velocity v_x with stiffness, for a constant R_{proj} cluster. For low stiffness magnitudes, the stiffness response of the pressure controls this increase (here $P' = (0.6,0.8,1.0,1.5,2.0,3.0) \cdot 10^{-3}$ kPa/μm which gives $s_P = (1.81,2.41,3.02,4.52,6.03,9.05) \cdot 10^{-2}$, from lighter to darker green, and $E^* = 140$ kPa is fixed). The surface tension characteristic values are obtained from pressure Eq.(S14-S17) with the R_{sphere} factor, which is not constant for these plots (see Methods). (e,f) Representative example of the velocity and shape dynamics of a migrating cluster with a constant volume, with initial contact radius $R(t = 0) = 20$ μm and height $H(t = 0) = 50$ μm ($R_{sphere}(t = 0) = 29$ μm and so $\theta(t = 0) = 136.4^\circ$), and initial stiffness of $E = 23.7$ kPa. Since the cluster is migrating towards stiffer regions of the substrate, the stiffness axis is also representing the time evolution.*

Other model parameters are: $L_c = 15$ μm, $R_{proj.} = 45$ μm, $\lambda = 424.266$ μm, $\eta = 20$ MPa·s, $E_0 = 0.5$ kPa, $E' = 0.03317$ kPa/μm and $P_0 = 4.2 \cdot 10^{-3}$ kPa. In b-d), $\zeta = -5$ kPa and saturated traction and friction profiles are assumed with $E^* = 140$ kPa, $\zeta_i^\infty = 0.2$ kPa/μm, $\xi^\infty = 0.2$ kPa·s/μm² and $\xi_0 = 0.222$ kPa·s/μm² (summed to the saturated friction to avoid too low values which would give rise to an ill-defined problem). In c,e-f), linear traction, friction and surface tension profiles are taken for simplicity, with $\zeta_i^0 = 6.8 \cdot 10^{-4}$ kPa/μm, $\zeta_i' = 5 \cdot 10^{-5}$ kPa/μm², $\xi_0 = 0.222$ kPa·s/μm², $\xi' = 10^{-4}$ kPa·s/μm³. In e-f) $\zeta = -2$ kPa and $P' = 0.6 \cdot 10^{-3}$ kPa/μm, whereas in c) $P' = 1.5 \cdot 10^{-3}$ kPa/μm.

A representative time evolution of the cluster morphology predicted by the model is illustrated in Figure 4-13 e-f (see also Appendix 2). The cluster starts with a low wettability at a soft region and then it expands and increases its wettability as it advances towards stiffer regions at increasing velocity. Upon reaching stiffer substrates, the tissue slows down when it reaches a high wettability (as friction and force saturation become more important). Therefore, according to the model, a given interplay between cell contractility, cluster size, stiffness, and cell traction forces could position clusters near their wetting transition regime and thus provide them with the sweet spot where cluster durotaxis is maximum, regardless of the coating of the underlying substrate.

In order to validate this prediction, A431 cell clusters were seeded on gradients of stiffness coated with fibronectin and treated with EGF aiming to increase contractility and thus place clusters' wetting state in the vicinity of an active wetting transition where durotaxis was predicted to be optimal.

5. Clusters durotax on ECM ligands close to the wetting transition on fibronectin substrates

According to our theory, the emergence of durotaxis at the wetting transition should be independent of the nature of the adhesion ligand. We thus tested whether a similar phenomenology can be observed on ECM ligands rather than on E-cadherin. Cell clusters were seeded on polyacrylamide gels of 0.2, 6, 24 and 200 kPa functionalized with fibronectin. To push the wetting transition to an intermediate stiffness range, we treated clusters with 10 ng/mL of human Epidermal Growth Factor (EGF). With this treatment, cluster morphology showed a dependence with stiffness similar to that observed on E-cadherin substrates: full dewetting on soft substrates and a wetting transition on intermediate stiffness (Figure 4-14 a,b).

Next, we tracked A431 cell clusters as explained in Figure 4-5 c. Cluster velocity and persistence were maximum at this intermediate regime, displaying a biphasic relationship with stiffness similar to that observed on E-cadherin substrates (Figure 4-5, Figure 4-14 c, d, Supplementary video 8).
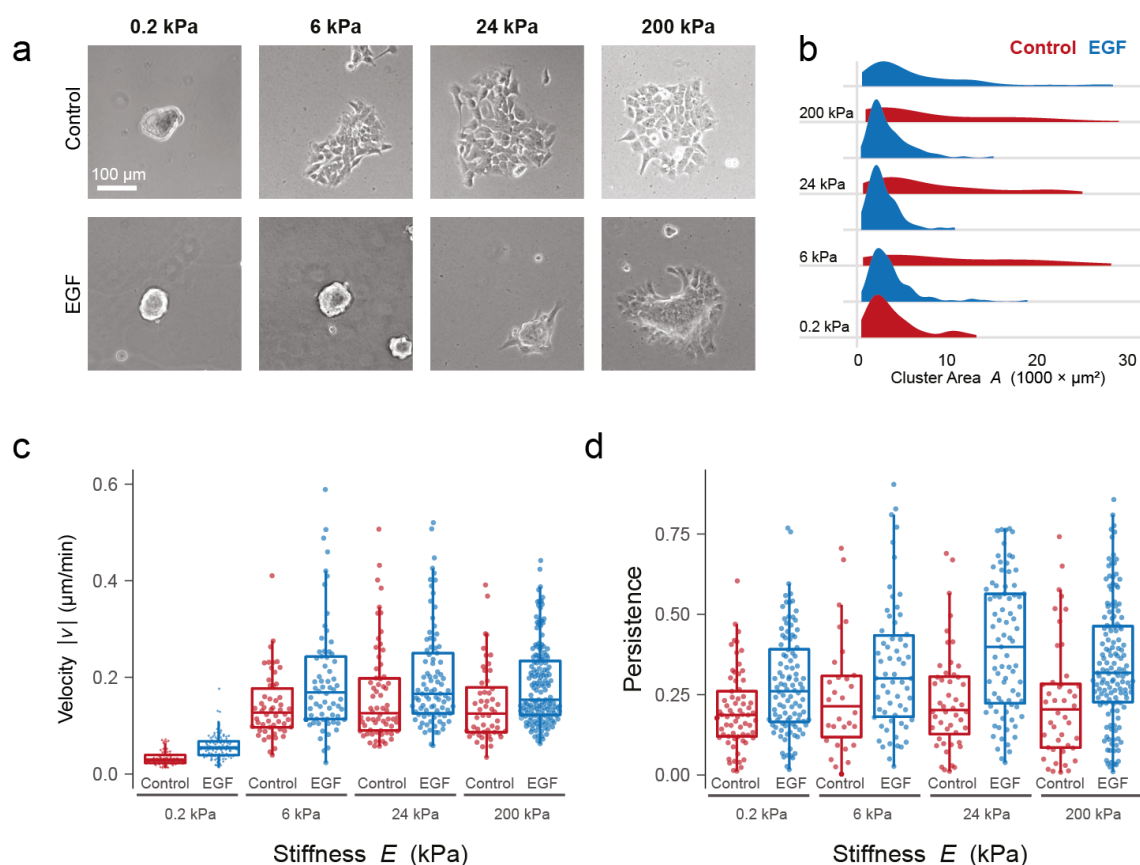
Figure 4-14. A431 clusters challenged with EGF on fibronectin-coated uniform stiffness substrates display similar wetting state, velocity and persistence profiles as A431 cell clusters seeded on E-cadherin-coated uniform stiffness substrates. *(a) Representative phase contrast images of control and EGF-treated clusters seeded on uniform stiffness gels coated with fibronectin. (b) Area distribution for controls (red) and A431 cell clusters treated with EGF (blue) on uniform stiffness gels coated with fibronectin. (c) Speed profiles of controls (red) and A431 cell clusters treated with EGF (blue) on uniform stiffness gels coated with fibronectin. (d) Persistence profiles of controls (red) and A431 cell clusters treated with EGF (blue) on uniform stiffness gels coated with fibronectin. Each dot in (c) and (d) represents 1 cluster. n ≥ 68 clusters.*

We then studied whether EGF-treated clusters display durotaxis on gradient substrates coated with fibronectin. In order to test this hypothesis, we seeded A431 cell clusters on stiffness gradients coated with fibronectin and treated them with EGF (Figure 4-15 a, Supplementary video 9).
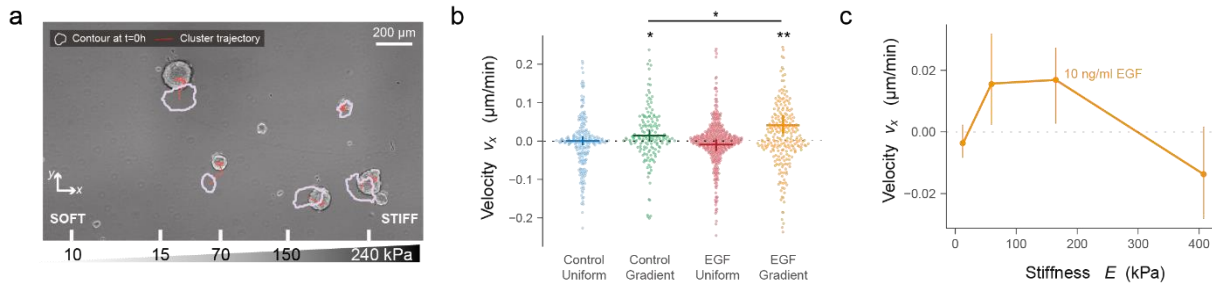
Figure 4-15. A431 cell clusters treated with EGF undergo a wetting transition concomitant with he onset of durotactic migration on fibronectin-coated stiffness gradients. (a) Representative phase contrast image of EGF-treated A431 cell clusters migrating on a fibronectin-coated gradient of stiffness. Image was taken at t = 10 h. Original position (time = 0 h) of each cluster is represented by a purple outline. The red line represents the migratory trajectory obtained by time-lapse microscopy. Bottom scale indicates the local stiffness at each point of the image. (b) Velocity within the x-axis of controls and EGF-treated A431 cell clusters on uniform stiffness gels (pooled data from 0.2, 6, 24 and 200 kPa gels) and stiffness gradients. Horizontal and vertical bars represent mean ± 95% CI, respectively. Each dot represents the mean of a cluster. n ≥ 128 clusters. Velocity towards stiffer regions is significantly larger than 0 in A431 cell clusters seeded on gradients (bootstrapping t-test, p < 0.001). Conversely, migration of A431 cell clusters on uniform stiffness was random. EGF-treated clusters seeded on gradients showed an enhanced durotactic migration compared to untreated clusters. (c) Analysis of individual displacements of EGF-treated clusters seeded on fibronectin-coated stiffness gradients display a durotactic peak in the 30-200 kPa bin (median ± 95% confidence interval estimated by bootstrapping; n ≥ 222 cluster displacements).

Whereas neither controls nor EGF-treated A431 cell clusters migrated following a preferential direction on uniform stiffness gels coated with fibronectin, both controls and EGF-treated A431 cell clusters durotaxed on gradients of stiffness coated with fibronectin (Figure 4-15 b). Remarkably, cluster durotaxis was higher in EGF-treated clusters compared to controls (Figure 4-15 b).

Together with the biphasic dependence of cluster durotaxis with stiffness (Figure 4-15 c), these results indicate that the proximity to an active wetting transition provides epithelial cell clusters with an enhanced durotactic migration. Thus, a wetting state close to the vicinity of an active wetting transition provides epithelial cell clusters with enhanced mechanosensing and migratory outcomes regardless of the underlying substrate composition proteins.

6. Catastrophic detachments of protrusions give rise to durotactic hops

Finally, we studied the statistics of cluster migration. To this aim, we computed the probability density of the displacements ρ undergone by migrating clusters on E-cadherin-coated gradients of stiffness (see inset in Figure 4-16 a). We found that most displacements were well described by an exponential distribution (Figure 4-16 a, dark line). However, this distribution failed to capture displacements > 25 µm, which were much more frequent than captured by the exponential fit. This fat tail in the distribution (which accounted for 0.4% of the total displacements), corresponded to hops that followed from sudden retraction of cluster protrusions (Figure 4-16 b, Supplementary video 10). Strikingly, we found that these large hops were more durotactic than smaller displacements (Figure 4-16 c,d).
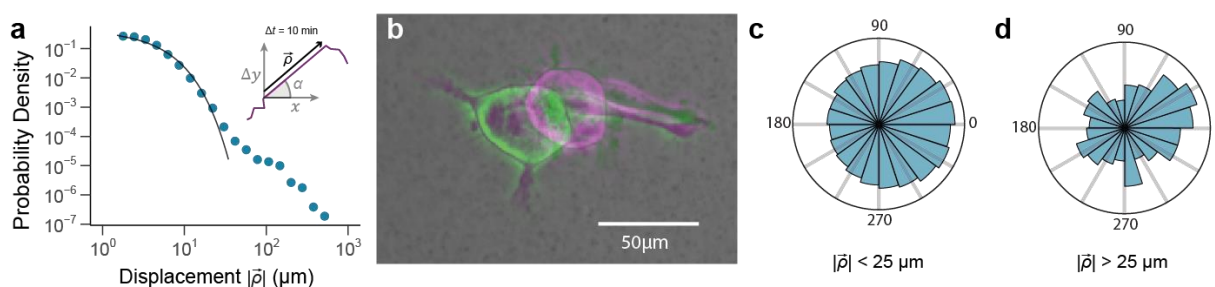
Figure 4-16. Catastrophic detachments of filopodia-like protrusions give rise to fast migratory events. *(a) Probability density of the radial displacements (ρ) undergone by migrating clusters on stiffness gradient gels (see inset). Dark line is an exponential fit. Around displacements of 25 µm, probability density deviates from the exponential fit. Therefore, catastrophes were defined as those displacements ρ > 25 µm. (b) Example of sudden detachments of filopodia-like structures that trigger a catastrophe. The initial cluster image is represented in green, whereas magenta shows the same cluster after 10 min. Distribution of the angle α between the instantaneous velocity vector and the x-axis (see inset panel a) for non-catastrophic (c) and catastrophic (d) events.*

Previous research showed that the cell cytoskeleton undergoes sudden reconfiguration events, highly resembling the dynamics of earthquakes in the Earth's crust[184]. Our results show that epithelial clusters in the vicinity of an active wetting transition also feature these dynamics, resulting in the emergence of rare but fast migratory events.

5. Discussion

1. General discussion

Recent research studies indicate that E-cadherin could mediate migratory events in contexts depleted of ECM[50,53,161,185]. Due to the mechanosensory properties of the E-cadherin/α-catenin complex[107], we hypothesized that cells might be able to direct their migration by following mechanical cues through E-cadherin-based interactions. To test this hypothesis, we adapted a protocol to coat polyacrylamide gels with oriented E-cadherin (Figure 4-1). Since gradient sensing is generally enhanced in collectives of cells compared to single cells[39], we generated cohesive clusters of epithelial A431 cells and seeded them on E-cadherin-coated polyacrylamide gels of uniform stiffness (Figure 4-5). We found that both velocity and persistence followed a biphasic dependence with stiffness, peaking at intermediate stiffness values (Figure 4-5, Supplementary video 1). Interestingly, we found a correlation between the wetting state of clusters and their migratory outcome: the closer the clusters were to an active wetting transition, the higher their velocity and persistence were (Figure 4-7, Supplementary video 2). We then seeded clusters of cells on gradients of stiffness coated with E-cadherin and found that they cohesively migrated from low to high stiffness (Figure 4-10, Supplementary video 5), exhibiting a migratory phenotype characterized by dynamic transitions in tissue morphology (Supplementary video 6). This finding constitutes the first evidence of cadherin-based migration and cadherin-based durotactic events. Our data showed that E-cadherin-mediated durotaxis increased with cluster size and stiffness slope (Figure 4-11, Figure 4-12). We also found that cluster durotaxis showed a biphasic relationship with stiffness, where durotaxis was optimal in intermediate stiffness (Figure 4-11), similarly to the observed dependence of cluster velocity with stiffness on uniform stiffness E-cadherin-coated polyacrylamide gels (Figure 4-5). Finally, partial inhibition of cell contractility resulted in a decreased durotactic outcome as well as a shift of the durotactic peak towards lower stiffness (Figure 4-12, Supplementary video 7).

We next adapted a previously published theoretical framework based in active matter[117] to describe cluster durotaxis by combining experimental data with theoretical approaches[70,117,145]. We propose that the equilibrium droplet shape, and hence its contact angle θ (Figure 4-7), are determined by a generalized Young-Dupré force balance between the active forces in the basal cell monolayer and the out-of-plane surface tension γ of the cell clusters (Figure 4-8). In summary, the model describes cluster durotaxis as a function of active cellular tractions, cell contractility, cluster size, monolayer viscosity, friction with the substrate and surface tension. Importantly, the addition of the surface tension γ parameter to the model constitutes the first active matter-based model to interpret the durotactic migration of clusters in a three-dimensional picture of active wetting. Previous works modelling cluster durotaxis in the framework of active matter did not account for the three-dimensional geometry of

85

clusters, as well as the biphasic dependence of durotaxis with stiffness[70,145]. The fact that a similar durotactic behavior was recapitulated in clusters close to an active wetting transition migrating on fibronectin-coated gradients of stiffness (Figure 4-14, Figure 4-15) suggests that cell clusters might be more responsive to mechanical cues when they are close to an active wetting transition. Therefore, our results suggest that mechanical cues could be key to directing the migration of collectives of cells in the vicinity of an active wetting transition during their *in vivo* migration. Since many developmental processes rely on the collective migration of cells displaying a three-dimensional shape resembling a droplet of water[50,52,53,88,159,161,185], we hereby propose that those clusters could be particularly responsive to mechanical cues to direct their migration.

Finally, we showed that most individual displacements of cell clusters whose wetting state was close to a wetting transition were well recapitulated by an exponential distribution, but a small fraction underwent rarely large migratory behaviors (Figure 4-15, Supplementary video 10). Cytoskeletal rearrangements were previously reported to feature sudden reconfiguration events, in analogy with the dynamics of earthquakes in geologic systems[184]. Our data suggests that these dynamics also take place in clusters whose wetting state is close to an active wetting transition, ultimately enabling the emergence of rare and fast migratory events.

2. Experimental set-up development and validation

During the last decade, the development of different techniques to coat substrates with E-cadherin enabled scientists to study the generation of traction forces at the cell-cell interface[108,125]. Importantly, unlike substrate functionalization with ECM proteins, substrate functionalization with E-cadherin needs to contemplate its orientation. Whereas most studies make use of a Fc tag contained in a chimeric EC1-5 peptide to achieve its orientation[119,124,127] (Fc-tagged EC1-5), a small number of research studies achieve orientation through a histidine tag fused to the extracellular domain of E-cadherin[121,128,172] (histidine-tagged EC1-5). Despite E-cadherin orientation being achieved in both approaches, the presence of an IgG-Fc tag mediating the binding of E-cadherin to the substrate in the first approach might hinder the readout of the generation of traction forces. That is because IgG domains adopt tertiary protein structures that unfold over a critical tension[186], thus diminishing the transmission of E-cadherin-mediated traction forces to the substrates. In contrast, histidine tags consist of 6 linear histidine residues that do not adopt a secondary or tertiary protein conformation. Therefore, force transmission on histidine-tagged E-cadherin-coated substrates does not trigger protein unfolding events and thus the readout of traction forces is more accurate. For this reason, we decided to adapt a previously published histidine-tagged E-cadherin-coating protocol from glass surfaces to polyacrylamide gels, as explained in the Materials and Methods and Results chapters (Figure 4-1).

As explained in the Results chapter, the A431 cell line was chosen from a cell line screening experiment based on paxillin immunostaining due to the apparent lack of FA-like structures on E-cadherin-coated gels (Figure 4-3). This cell line derives from a 85-year-old skin squamous cell carcinoma patient, and thus it constitutes a cancer epithelial cell line[187], tending to form monolayers when seeded at high cell density.

In order to assess the specificity of our experimental substrates, we performed controls employing genetic tools, DECMA (an E-cadherin blocking antibody) and immunostainings against paxillin to stain for the generation of FA complexes, combining the different approaches from previous research carried out on cadherin-coated substrates[119,121,128] (Figure 4-4). Firstly, we found that A431 cell count decreased upon the addition of DECMA antibody (Figure 4-4 a). Secondly, α-catenin KO A431 cells and double E/P-cadherin KO A431 cells seeded on E-cadherin-coated polyacrylamide gels displayed a rounder morphology than wild type A431 cells (Figure 4-4 a). Importantly, we used double E/P-cadherin KO A431 cells as the epidermoid carcinoma A431 cell line naturally expresses P, N and E-cadherin[109], possibly leading to the formation of heterotypic cadherin-based adhesions. Finally, A431

cells failed to form FA complexes on E-cadherin-coated polyacrylamide gels for up to 24 h (Figure 4-4 c).

Taken together, these results indicate that A431 cells make specific cadherin-based adhesions with our experimental E-cadherin-coated substrates. We hereby developed a robust protocol to coat polyacrylamide gels with E-cadherin enabling the study of mechanical processes driven by E-cadherin.

3. Spontaneous migration of epithelial cell clusters of different wetting states on E-cadherin-coated uniform stiffness substrates

In this thesis, we aimed to study how cell clusters migrating via E-cadherin respond to mechanical cues. Therefore, we seeded clusters of A431 cells on E-cadherin-coated polyacrylamide gels of 0.2, 6, 24 and 200 kPa. A custom-made semi-automatic tracking algorithm enabled us to study the dynamics of A431 cell clusters seeded on the E-cadherin-coated polyacrylamide gels. Cluster velocity and persistence followed a biphasic dependence with substrate stiffness, with those parameters peaking at intermediate stiffness values (24 kPa) (Figure 4-5). Next, the acquisition of high-resolution images of mCherry-Lifeact A431 cell clusters seeded on E-cadherin-coated polyacrylamide gels revealed that they dewetted soft gels, wetted stiff gels and presented a seeming wetting transition on intermediate stiffness gels (Figure 4-6, Figure 4-7). Therefore, we provided a direct correlation between the wetting state of clusters and their dynamics, with cell clusters in the vicinity of a wetting transition displaying higher velocity and persistence (Figure 4-5, Figure 4-7). Our results are consistent with previous literature, where cluster velocity was optimal at the proximity to a wetting transition understood within the framework of active wetting[143].

We then studied the generation of traction forces by A431 cell clusters seeded on 1 kPa and 6 kPa E-cadherin-coated polyacrylamide gels. As previously reported by Pérez-González et al.[117], we found that clusters exerted radial traction forces systematically decreasing from the cluster edge to the cluster core (Figure 4-8). In line with previous findings[108,125], we also found that clusters exerted higher traction forces on stiffer E-cadherin-coated substrates (Figure 4-8).

In the study by Douezan et al.[188], the spreading parameter S predicted the wetting state of clusters and depended on the cell-substrate and cell-cell adhesion energy per unit area (W_{CS} and W_{CC}, respectively). As commented in the introduction of this thesis, a precursor film of cells wetting the substrates formed when S>0 (and thus $W_{CS} > W_{CC}$). In our work, only clusters seeded on 200 kPa E-cadherin-coated polyacrylamide gels displayed a precursor film-like structure, whereas clusters seeded on 6 and 24 kPa E-cadherin-coated polyacrylamide gels exhibited membrane protrusions in the z axis forming acute angles with the substrates (Figure 4-6, Figure 4-7). 3D traction force microscopy experiments revealed that clusters actively exerted upwards pulling forces in the sites where membrane protrusions adhered to the substrates, balanced by the generation of pressure in the centre of clusters measured in the form of negative traction forces (Figure 4-8). Therefore, the measured traction forces in the z axis shifted from positive to negative from the cluster edge to the cluster centre, and their magnitude increased with substrate stiffness (Figure 4-8). The fact that partial inhibition of cell contractility resulted in clusters wetting the polyacrylamide gradients at lower

stiffness suggests that membrane protrusions forming acute angles with the substrates contributed to increasing the wetting state of clusters in a tight interplay with cell contractility (Figure 4-12, Supplmentary video 7).

Taken together, these results suggest that E-cadherin-coated polyacrylamide gels constitute an experimental framework challenging epithelial cell clusters with an unstable regime characterized by highly dynamic active wetting transitions. We think that this phenomenology arises from the low cell-substrate adhesion strength: traction forces exerted by single cells on cadherin-coated substrates are generally lower than those reported for ECM-coated substrates[22,108,125]. Additionally, the limited availability of E-cadherin at the cell-substrate interface in epithelial clusters due to the competence between cell-cell junctions and cell-substrate adhesions for the recruitment of membranal E-cadherin might result in the generation of even lower traction forces. Nevertheless, we propose that the reported increase in traction forces with increasing substrate stiffness drives the observed durotactic migration of A431 cell clusters on E-cadherin-coated gradients of stiffness (Figure 4-10, Supplementary video 5).

4. Durotaxis is enhanced in the vicinity of an active wetting transition

The study of collective durotaxis has been hindered by the high wetting state displayed by groups of cells seeded on ECM-coated gradients of stiffness. In fact, the first evidence of collective durotaxis consisted on a preferential expansion of an epithelial cell monolayer towards stiffer regions when plated on a gradient of stiffness coated with fibronectin[39], rather than a net translocation of the bulk of the monolayer. In our study, we showed that three-dimensional clusters exhibit robust durotaxis, constituting the first evidence of cadherin-on-cadherin durotactic migration. Remarkably, both cluster edges moved in favour of the direction of the gradient of stiffness, thus resulting in net translocations of clusters often larger than their respective size (Figure 4-10, Supplementary video 5, Supplementary video 6). This phenomenology is enabled by the partial wetting state of cell clusters seeded on relatively stiff E-cadherin-coated substrates: clusters seeded on fibronectin-coated substrates fully wetted at a stiffness range comprised between 0.2 and 6 kPa (Figure 4-14), whereas they kept a partial wetting state when seeded on E-cadherin-coated substrates of 24 kPa and above. On those substrates, clusters presented dynamic assembly and disassembly events of membrane protrusions (Supplementary video 3, Supplementary video 6) that mediated the generation of traction forces and contributed to increasing the wetting state of clusters in a tight interplay with contractile cellular forces and friction with the substrate.

Due to the observed spherical cap shape of clusters on E-cadherin-coated substrates (suggesting that clusters displayed a partial wetting state) (Figure 4-7) and their active generation of traction forces (Figure 4-8), we interpreted cluster durotaxis within the framework of active wetting. We adapted a previously published theoretical framework that explained cluster spreading as a function of cluster size, traction forces, contractility and friction[117] to successfully describe the durotactic migration of three-dimensional cell clusters. For this, we added the out-of-plane contribution of the surface tension γ, whose component on the substrate plane and normal to the edge of clusters plane was encoded in the 2D active polar fluid model ultimately accounting for the three-dimensional geometry of clusters.

Below, I will discuss on the contribution of the different model parameters on cluster durotaxis, combining both theory and experimental results.

Consistent with previous studies[117,143], we found that the contact angle θ formed between the E-cadherin-coated substrates and the line tangent to the edge of clusters decreased with stiffness, and thus the wettability of clusters increased with stiffness (Figure 4-7). Interestingly, we reported that clusters seeded on intermediate stiffness were close to an active wetting transition ($\theta \simeq 90^\circ$) and displayed enhanced motility (Figure 4-5) and durotaxis (Figure 4-10). In contrast, clusters seeded on lower stiffness displayed a more dewet state, and their durotactic migration increased with increasing

stiffness up to the peak in durotaxis observed on intermediate stiffness substrates (Figure 4-11, Figure 4-12). Remarkably, this phenomenology could not be accounted for by the 2D force balance only[70,145]. Conversely, the observed increase in z tractions (modelled as pressure) with increasing stiffness indicated that clusters' surface tension was mechanosensitive (Figure 4-8), which led us to hypothesize that the increase in durotaxis with increasing stiffness in dewetted clusters arose from the wettability of clusters. Therefore, we included this effect in the model by means of an active surface tension parameter γ, which enabled us to explain the observed increase in durotaxis with increasing stiffness in dewetted clusters ($\theta > 90º$).

Following previous studies[70,77,144,177–179,181], the saturation of tractions together with the high friction experienced by clusters on high stiffness explained the experimentally reported decay in durotaxis on high stiffness (Figure 4-11, Figure Appendix 2-5 a).

The fact that large clusters were more durotactic than small clusters (Figure 4-11) is explained by the means of a higher contact radius R with the substrate for larger clusters with the concomitant generation of larger traction forces, ultimately increasing the v_x and therefore the durotactic outcome of large clusters. The experimental observation of the durotactic peak in large clusters shifting to higher stiffness was not recapitulated by the model, as it predicted that small clusters would experience a wetting transition at higher stiffness and hence their durotactic peak would be shifted in this direction (Figure Appendix 2-5 a). This discrepancy with the model's predictions and the experimental measurements can be explained using two different approaches. Firstly, the model assumed that clusters exert the same pressure P on a fixed substrate stiffness regardless of cluster size, therefore assuming that the surface tension parameter γ is increased in big clusters (extracted from the Young-Laplace equation $P = 2\gamma/ R_{sphere}$). In contrast, assuming that clusters exhibit a constant surface tension γ on a fixed stiffness substrate would imply that the pressure exerted by clusters decreases with cluster size. With this hypothesis, the peak of durotaxis for large clusters would be probably shifted towards higher stiffness (Figure 4-13 d) compared to small clusters, ultimately explaining our experimental results (Figure 4-11). The second approach that could be adopted to better capture our experimental results implies tuning the contractility parameter $-\zeta$. This matter will be addressed after discussing the role of contractility on cluster durotaxis.

Regarding intercellular contractility $-\zeta$, we reported that the durotactic peak shifted to lower stiffness upon the partial inhibition of contractility (Figure 4-12). This phenomenology was recapitulated by the model, but not the magnitude of the durotaxis: whereas the model predicted that clusters would display a more durotactic behaviour upon the partial inhibition of cell contractility, control clusters durotaxed more efficiently. A plausible explanation for this discrepancy is that the ROCK inhibitor used

to partially inhibit cell contractility might not only affect the contractility parameter of the model, but also the other active components that are related to actomyosin activity. For example, previous research indicates that inhibition of ROCK and MLCK decreases traction forces[20,170,189–191], and so the model should contemplate a reduced parameter ζ_i in those experiments. Concomitantly, surface tension mechanosensitivity might be reduced, which could also be included in the model. Therefore, to capture our experimental results upon Y-27632 addition, the model should probably contemplate a reduction in all the active components.

Remarkably, the model's predictions were made assuming a constant value of contractility -ζ. However, changes in cell contractility might occur for different cluster sizes and stiffness due to the nature of E-cadherin-based adhesions: RhoA concentrates at the cell-cell junctions in an E-cadherin-dependent manner, where it activates myosinIIA and myosinIIB resulting in the generation of contractile forces near the junctions[116,192]. Therefore, larger clusters exhibiting increased overall junctional E-cadherin might present a higher activation of RhoA and thus an increased intercellular contractility. Besides, myosin VI was recently identified as a force sensor, whose association with E-cadherin was enhanced with increasing junctional tension within a cell monolayer[193,194]. In this scenario, myosin-IV promotes the recruitment of the heterotrimeric Gα12 protein to E-cadherin, where it signals for p114 RhoGEF to activate RhoA ultimately increasing cell contractility to protect epithelia against rupture upon acute tensile stress[194]. This finding, together with the fact that the E-cadherin/α-catenin complex is mechanosensitive and thus traction forces generated at E-cadherin-based junctions increase with stiffness[101,107,108,125], suggests that cell contractility follows a similar trend: through the establishment of E-cadherin-dependent adhesions with substrates, clusters on stiff substrates might present an enhanced activation of cell-substrate-localized RhoA and thus present an increased contractility. This could be assessed experimentally by the quantification of junctional RhoA in cell clusters seeded on E-cadherin-coated substrates of different stiffness, but it represents a technical challenge due to the weak adhesions made by clusters on those substrates. In all, these findings suggest that an increase of cell contractility with cluster size and stiffness could be contemplated in the model. In this picture, larger clusters would probably display a durotactic peak shifted towards higher stiffness due to a size-dependent and a stiffness-dependent increase in cell contractility, ultimately providing clusters with a higher range of the critical stiffness at which a wetting transition occurs.

Finally, the increase in durotaxis with stiffness slope E' (Figure 4-12) was recapitulated by the model (Figure Appendix 2-5 c), which is consistent with previous research showing and predicting that durotaxis increases with increasing stiffness slopes[39,64,65,145].

Interestingly, the model predicted that clusters in the vicinity of an active wetting transition would present an enhanced mechanosensitivity and thus an increased durotaxis on stiffness gradients regardless of the coating of the underlying substrate. To test this hypothesis, clusters were seeded on fibronectin-coated gradients of stiffness (which present a higher friction than E-cadherin-coated gradients due to the higher adhesiveness) and treated with EGF to promote contractility and thus push the wetting transition towards stiffer regions (Figure 4-14, Supplementary video 9). As predicted by the model (Figure Appendix 2-5 b, Figure 4-13 c), we found that the active wetting transition of clusters was shifted to stiffer regions upon EGF addition, concomitant with a decrease in durotaxis and a shift of the durotactic peak towards higher stiffness (Figure 4-15). This finding suggests that our proposed 3D active wetting theory is not only valid for E-cadherin-coated substrates, but it can also be generalized to clusters migrating on ECM whose interplay between cellular traction, intercellular contractile stresses, friction, surface tension and viscosity position their wetting state in the vicinity of an active wetting transition.

Finally, it is important to highlight that our observations and predictions are consistent with those from the only research study recently demonstrating that durotaxis occurs *in vivo*, specifically during *Xenopus laevis* neural crest migration[52]. As explained in this thesis, the study of durotaxis has been hindered by the high wettability of tissues on relatively low stiffness; consequently, the first observation of collective durotaxis relied on an asymmetric expansion of a cell monolayer on a stiffness gradient rather than a net translocation[195]. In the study by Shellard and Mayor, mechanical and chemotactic gradients synergistically drive the net translocation of neural crest clusters on a fine layer of fibronectin presented on the surface of adjacent placoidal tissue[52]. Even though the authors avoid making an analogy of the neural crest shape within the framework of wetting, their data shows that neural crest clusters retain a spherical-capped shape reminiscent of the phenomenology observed in A431 cell clusters seeded on E-cadherin-coated gels (Supplementary video 6). Remarkably, the ablation of cortical actin cables in the rear of neural crest clusters resulted in an impaired migratory outcome. This finding evidences the important role of cell contractility in positioning cell clusters in the vicinity of an active wetting transition, potentially providing them with the ability to undergo net translocations. Taken together, these data suggest that our study could bridge the theoretical gap between Sunyer et al.[39] and Mayor and Shellard[52] works, with active wetting as the main candidate to induce the durotactic migration of cellular clusters.

Summing up, in this thesis we propose a novel theoretical framework to explain cluster durotaxis as a function of cellular tractions ζ_i, intercellular contractility $-\zeta$, surface tension γ, monolayer viscosity η, stiffness slope E' and friction ξ in a 3D picture of active wetting. Remarkably, through the addition of

an active surface tension parameter γ, our conceived model constitutes the first active matter-based model to describe the durotactic migration of clusters in a three-dimensional picture of active wetting.

During development and cancer metastasis, tissues experience drastic morphology changes which are usually encompassed with the onset of cell migration[50,53,67,159,185,196]. Interestingly, some migratory events during embryogenesis such as the epiboly can be studied within the theoretical framework of active wetting[197]. However, the underlying mechanisms of many developmental processes remain largely unknown due to the complexity in the environments of developing embryos as well as the rarity of the migratory events leading to cancer metastasis[198]. In our work, we showed that through the establishment of weak E-cadherin-dependent adhesions in a context depleted of ECM, viscosity tends to dominate over friction resulting in the hydrodynamical coupling of both migrating leading and trailing cluster edges. Besides, the fact that the expression of different proteins of the cadherin family can be detected at very early developmental stages[162,199–201], together with the enhanced abilities of E-cadherin-expressing CTC in generating metastasis[85,103], suggests that E-cadherin could be the driver of the migration in those processes. In this picture, the interplay between the aforementioned parameters could potentially position the migrating cell clusters in the vicinity of an active wetting transition, resulting in the maximization of cell migration.

With our model, we can also provide hypotheses for the mechanisms regulating cell migration in the context of cancer metastasis: bone metastases are much more common than primary bone cancers[202,203]. Due to the high Young's modulus of bones, veins and capillaries irradiating the bones could constitute stiffness gradients, with the inner and the outer part of the capillaries representing the low and high stiffness regions, respectively. Spherical CTCs within the bloodstream could use the proposed gradients in stiffness potentially presented in veins irradiating bone structures to initiate an extravasation process (in cooperation with a myriad of other effector proteins such as metalloproteases) ultimately metastasizing into the bones, where the migration would stop due to a critical increase in the friction experienced by cancer cell clusters. Even though cancer metastasis constitutes a very complex matter involving the cooperative effect of different cellular processes, our hypothesis could be tested experimentally by combining microfluidics and imaging techniques, where CTCs would be injected into porous channels adjacent to substrates of different stiffness simulating the different Young's modulus within the different tissues of our bodies.

Further work needs to be carried out on further characterizing the mechanical contexts of migrating cell clusters and their dynamics in order to fully comprehend the complex process collective cell migration represents. In this line, the model we hereby propose could shed some light on this matter.

6. Conclusions

1. A431 cells seeded on polyacrylamide gels coated with histidine-tagged E-cadherin form specific cadherin-based adhesions with the substrates

2. A431 cell cluster velocity and persistence on E-cadherin-coated polyacrylamide gels show a biphasic dependence with substrate stiffness

3. The contact angle θ formed between E-cadherin-coated substrates and the line tangent to A431 cluster edges decreases with stiffness

4. A431 cell clusters seeded on E-cadherin-coated polyacrylamide gels undergo a wetting transition at intermediate gel stiffness (6-24 kPa)

5. A431 cell clusters seeded on E-cadherin-coated polyacrylamide gels exert radial tractions in the xy plane that systematically decrease from the edge of clusters to their core

6. A431 cell clusters seeded on E-cadherin-coated polyacrylamide gels extend membrane protrusions in the z axis that actively generate traction forces

7. A431 cell clusters seeded on E-cadherin-coated polyacrylamide gels exert positive normal tractions in the z direction close to the cluster edge that are balanced with negative tractions in the z direction at the centre of clusters

8. A431 cell clusters respond to E-cadherin-coated polyacrylamide gradients of stiffness by systematically migrating from low to high stiffness regions, constituting the first reported evidence of cadherin-mediated durotaxis

9. E-cadherin mediated durotaxis of A431 cell clusters shows a biphasic dependence with stiffness, peaking at intermediate stiffness and correlating with an active wetting transition

10. E-cadherin mediated durotaxis increases with cluster size and the durotactic peak is shifted to higher stiffness in larger clusters

11. E-cadherin mediated durotaxis decreases upon partial inhibition of cell contractility, peaking at lower stiffness

12. E-cadherin mediated durotaxis increases with stiffness gradient

13. A model within the framework of active 3D wetting explains E-cadherin-based cluster durotaxis as the interplay between cellular traction forces, cell contractility, friction, stiffness slope and surface tension

14. The incorporation of a surface tension parameter to the model successfully recapitulates the dynamics and the shape of migrating A431 cell clusters

15. The model used to describe E-cadherin mediated durotaxis can also we applied when adhesion is mediated by other ligands, such as fibronectin

16. The critical stiffness for the wetting transition of A431 clusters migrating on fibronectin substrates shifts towards stiffer regions upon increasing the contractility with EGF

17. A431 cell clusters close to an active wetting transition migrate by undergoing simultaneous wetting and dewetting events on both cluster edges

18. The proximity to an active wetting transition provides epithelial cell clusters with an enhanced durotactic behaviour and thus higher mechanosensitivity

7. Appendices

Appendix 1. On the polyacrylamide gel functionalization with EC1-5

1. EDC/NHS chemistry basis

Carbodiimide (EDC/NHS) reactions rely on a nucleophilic attack exerted by an amino group (-NH$_2$). This is possible because amino groups, when unprotonated (-NH$_2$), have an unpaired pair of electrons which can exert a nucleophilic attack towards a more electrophilic atom (Figure Appendix 1-1).
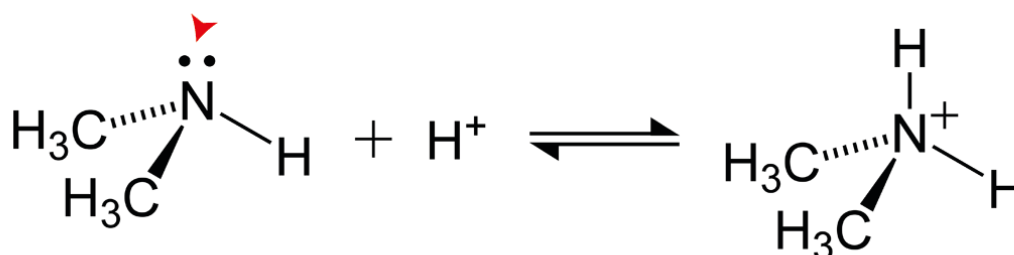
*Figure Appendix 1-1. **Amino groups have no nucleophilic power when positively charged**. (left) unprotonated amino group exhibiting a pair of unpaired electrons (red arrowhead). (right) protonated (and thus positively charged) amino group with no free electrons. Both molecules coexist in an equilibrium dependent on the pH.*

The aim of EDC/NHS reactions is to covalently bind two molecules through an amide bond. The reagents are two molecules, one displaying an amino group (-NH$_2$) and the other one presenting a carboxyl group (-COOH). Generally, the molecule containing the carboxyl group is attached to a bigger structure (e.g. polyacrylamide gel, carboxylated surfaces), and is the one desired to functionalize with the molecule containing the amino group. This appendix describes how to functionalize a carboxylated polyacrylamide gel with oriented cadherins.

Important considerations:

Since EDC/NHS reactions depend on the nucleophilic power of a molecule, ensuring that this molecule is nucleophilic is key to succeeding at using EDC/NHS technique for coating surfaces. In our case, the nucleophilic molecule is an amino group, and therefore it is vital to ensure that such group is not positively charged.

The isoelectric point of a protein (pI) is the pH at which this protein presents no net charge (Q = 0). At a pH>pI, proteins will be negatively charged, and amino groups will be -NH$_2$. At a pH<pI, proteins will be positively charged, and thus amino groups will be in the form of -NH$_3^+$ (Figure Appendix 1-2).

Amino groups are positively charged at a pH below the isoelectric point (pI) of a protein. Therefore, working at a pH higher than the pI is of paramount importance when coating a substrate using an EDC/NHS-based protocol.
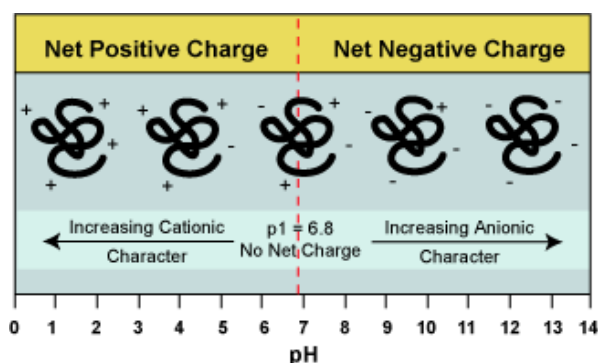
Figure Appendix 1-2. Proteins' charge depends on pH. Amino and carboxyl groups are the groups responsible for a protein's charge; therefore, controlling the pH is crucial when controlling a protein's charge. (Left): at a pH<pI, proteins are positively charged. (Centre): at a pH=pI, proteins have a net charge equal to zero. (Right): at a pH<pI, proteins are negatively charged, and thus carbodiimide reactions should take place at a pH > pI.

2. Functionalization of carboxylated polyacrylamide gels with oriented cadherins

N-alpha,N-alpha-Bis(Carboxymethil)-L-Lysine (NTA-NH$_2$) is a molecule needed for cadherin orientation. It contains three carboxyl groups and one amino group. Carboxyl groups are oriented in a way which permits the chelation of bivalent ions such as Copper (Cu^{2+}) or Nickel (Ni^{2+}) (Figure Appendix 1-3).
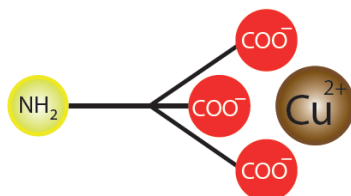
Figure Appendix 1-3. NTA-NH$_2$ chelates bivalent metal ions. Carboxyl groups belonging to NTA-NH$_2$ electrostatically attract copper ions.

NTA-NH$_2$ was incubated with CuSO$_4$ at pH= 8.0 at a concentration of 20mM and 25mM, respectively, aiming to form NTA-NH$_2$\Cu^{2+} complexes. Once all the carboxyl residues of the NTA-NH$_2$ were saturated with copper ions, pH was raised to 10.0, resulting in the precipitation of the non-chelated copper ions and thus forming CuSO$_4$. The supernatant contained exclusively copper ions chelated by NTA-NH$_2$ (in the form of NTA-NH$_2$\Cu^{2+}) and thus was recovered and used to functionalize the polyacrylamide gels.

Polyacrylamide gels were polymerized as previously described[39]. However, since polyacrylamide gels naturally lack carboxyl groups, acrylic acid was added to the gel premix prior to gel polymerization, resulting in the polymerization of gels containing carboxyl groups.

Polyacrylamide gels were incubated with 100mM EDC, 200mM NHS and 20mM Hepes at pH=7.0 for 20 minutes at 37ºC. Such an incubation results in the formation of an unstable reactive o-acylisourea ester, which is later substituted by an amine-reactive NHS-ester in the carbon atom belonging to the carboxyl group. Therefore, this incubation with such a high concentration of the reagents EDC/NHS leads to an extensive activation of carboxyl groups, making them more electrophilic and thus more susceptible to be attacked by an unpaired pair of electrons belonging to a more nucleophilic molecule. Since the amine-reactive NHS-ester formed from the EDC/NHS activation is a relatively unstable group that spontaneously hydrolyzes, parameters such as pH and incubation time need to be accurately controlled specially during the following steps.

After the EDC/NHS activation, polyacrylamide gels were incubated with the previously conjugated NTA-NH$_2$/Cu^{2+} for 45 min at pH=7.0 and 37ºC, resulting in the generation of a covalent amide bond between the carboxyl groups presented by the polyacrylamide gel and the amino group belonging to the NTA-NH$_2$/Cu^{2+} complex (Figure 4-1, step 1).

The used E-cadherin extracellular domains (EC1-5) presents a histidine tag in the c-terminal consisting of 6 histidine residues. Since histidine has an imidazole group, the histidine tag enables for an electrostatic chelation of bivalent metal ions. Therefore, histidine-tagged EC1-5 would spontaneously orient on a surface presenting NTA-NH$_2$/Cu^{2+}.

Polyacrylamide gels functionalized with NTA-NH$_2$/Cu^{2+} were incubated with his-tagged EC1-5 at a concentration of 0.1mg/mL (diluted in PBS) for 60 minutes at room temperature, and because of the aforementioned properties of His-tags, EC1-5 spontaneously orientated (Figure 4-1, step 2). Sodium chloride was added aiming to mask positively and negatively charged residues and thus avoid electrostatic interactions between cadherins and the functionalized surfaces in an undesired manner (non-oriented).

After cadherin orientation, polyacrylamide gels were incubated with 50mM EDC, 75mM NHS and 20mM hepes at pH= 7.0 and at 37ºC aiming to covalently bind carboxyl groups belonging to the NTA to amino groups belonging to the histidine tag of EC1-5 (Figure 4-1, step 3). Therefore, most of EC1-5 covalently bound to the gels, but a few remained covalently unbound, although electrostatically bound to the NTA-NH2/Cu^{2+} and thus chelating copper ions.

Aiming to get rid of non-covalently bound cadherins and copper ions, polyacrylamide gels were rinsed with imidazole and 1M (Figure 4-1, step 4), which because of its small size, is much more efficient at chelating bivalent metal ions than a histidine tag. This resulted in the elution of imidazole-chelated copper ions and non-covalently bound cadherins, and thus the polyacrylamide gels contained only and specifically covalently bound cadherins to NTA-NH$_2$.

Finally, in order to avoid unspecific binding between cells and polyacrylamide gels, PLL-gPEG was used to block carboxyl groups (Figure 4-1, step 5).

Appendix 2. Supplementary note for the active polar fluid model to describe tissue durotaxis

The model described in this section and in the Results chapter was developed by Irina Pi Jaumà, Jaume Casademunt Viader and Ricard Alert Zenón. This appendix was written by Irina Pi Jaumà, Jaume Casademunt Viader and Ricard Alert Zenón for the submission of our results to a scientific journal.

An active wetting transition enables optimal collective durotaxis

Our aim here is to present a theoretical framework to explain collective durotaxis of cell clusters in terms of a continuum mechanical model of the tissue, described as an active fluid droplet that partially wets the substrate. To this aim we first develop a theory of 3D active wetting for a uniform substrate, that builds upon a previous 2D description of cell monolayers. In this framework the contact angle of the droplet arises as a balance of contractile stresses, traction forces and surface tension. We then apply this effective theory to describe the durotactic response of a partially wetting cell droplet in the presence of a stiffness gradient of the substrate. We explain the generic nonmonotonic dependence of the durotactic velocity to substrate stiffness observed in experiments, in connection to the presence of a wetting transition, and predict how the durotactic response varies with different parameters. We finally use this approach to predict the evolution of cell clusters in time for a variety of situations.

1.   *Theory of 3D active wetting*

1.1 Rationale for a mechanical model of an active droplet

We describe the cell cluster in contact with a substrate as a liquid droplet that partially wets a solid surface with a contact angle θ. The droplet has a surface tension γ with the fluid environment, so that it is shaped as a spherical cap of radius R. This regular shape is assumed to average out the shape fluctuations of the tissue and capture the mean effect of active forces located at the tissue surface in the form of an effective surface tension, which in general we will assume to change as a mechanosensitive response to variations of the substrate stiffness. The liquid inside the droplet is assumed to be a static, incompressible fluid, which passively transmits the Young-Laplace pressure associated to curvature of the droplet, in particular to the solid substrate, where it can be directly measured. We further assume that the dynamics of the droplet is solely determined by the forces that are present at the basal monolayer, which will then be modelled as a 2D active polar fluid extending previous work in[117] to include the effect of the droplet surface tension. With this new ingredient, a finite contact angle for the droplet will be determined by the appropriate balance of active forces.

1.2 2D model of the basal cell monolayer

The basal monolayer is modelled as a 2D active fluid following the model studied in[70,117,145]. This is a continuum model for two fields, cell polarity $p(r,t)$ and velocity $v(r,t)$. The polarity field is assumed to follow a purely relaxational dynamics, since the timescale of repolarization through contact inhibition of locomotion $(\tau_{CIL}\sim 10min)$[204,205] is much smaller than flows in the monolayer $(\tau_{CIL}\sim 109min)$[176]. Thus, $\partial_t p_\alpha \propto -\delta F/\delta p_\alpha$, where the tendency of cells to align with their neighbors is enforced in the effective free energy

$$F = \int \left[\frac{a}{2}p_\alpha p_\alpha + \frac{K}{2}(\partial_\alpha p_\beta)(\partial_\alpha p_\beta)\right]\mathrm{d}^2r,$$

Equation 1

being K the Frank constant that defines the energetic cost of the polarity gradients[206], and $a > 0$ a restoring coefficient that favours the unpolarized state $p = 0$ in the bulk. We further assume a quasistatic evolution of the polarity $\partial_t p_\alpha = 0$, hence

$$L_c^2\nabla^2 p_\alpha = p_\alpha,$$

Equation 2

where $L_c \equiv \sqrt{K/a}$ is the nematic length that defines the thickness of a polarization boundary layer at the periphery of the monolayer. Since cells at the edge are polarized normally where they present maximal traction forces, we will solve 2, with the condition $p_\alpha = n_\alpha$, where n_α is the outward normal vector. The modulus of the polarity decays from one at the edge to zero in the bulk with a characteristic length L_c.

We describe tissue flow based on the force balance equation

$$\partial_\beta \sigma_{\alpha\beta} + f_\alpha = 0,$$

Equation 3

where $\sigma_{\alpha\beta}$ is the stress tensor and f_α the external force density originated at the tissue-substrate interface. Note that $\sigma_{\alpha\beta}h$ and $T_\alpha \equiv -f_\alpha h$ are the experimentally measured tension and traction, being h the height of the monolayer. In Equation 3 we have neglected inertia, consistently with the small values of Reynolds number, and contributions from pressure gradients. The latter is consistent with the assumption of high compressibility of the 2D fluid, which results from the fact that in-plane

compression or expansion is naturally accommodated in the real tissue by local changes in the monolayer thickness, without significant changes in pressure.

For the characteristic time scales of observation of the tissue dynamics, we may neglect elastic effects and assume the constitutive equations for the stress tensor as that of a compressible active viscous polar fluid[150,151,207]. This includes two main contributions: active contractile stresses originated in cell-cell pulling forces and quantified by the contractility parameter $\zeta < 0$, and viscous stresses that result from passive cell-cell adhesion forces and are weighted by an effective viscosity η.

Similarly, we consider that f_α has two main contributions: an active traction force due to cell-substrate pulling, proportional to polarity and with a maximum value ζ_i, and a friction coefficient ξ as a result to passive cell-substrate adhesion forces. While both ζ and η are intrinsic properties of the tissue, for a given set of conditions, the contact force parameters of friction ξ and active traction ζ_i should depend on substrate properties. The force balance equation (Equation 3) is thus made explicit by substitution of

$$\sigma_{\alpha\beta} = \eta(\partial_\alpha v_\beta + \partial_\beta v_\alpha) - \zeta p_\alpha p_{\beta,}$$

Equation 4

$$f_\alpha = -\xi v_\alpha + \zeta_i p_\alpha,$$

Equation 5[117]

To complete the model we need to specify the boundary conditions for the stress. This is the point where the effect of the 3D shape of cell cluster will be incorporated, so we defer this discussion to section 1.4.

1.3 The 2D active wetting transition for cell monolayers

It was shown in[117] that the above model predicts the existence of an active wetting transition in cell monolayers. This transition has no analogue in classical theory of wetting, and results from the competition between active traction that favours the spreading and contractile stresses of the tissue, which favour its retraction. We may define a characteristic active length of polar tissues as the ratio $L_p \propto |\zeta|/\zeta_i$. Then, the wetting transition identifies a critical value L_p^* such that for $L_p < L_p^*$ the tissue spreads and for $L_p > L_p^*$ it retracts.

In the literature of active matter[208] it is customary to define two limiting situations, characterized by the so-called screening length $\lambda \propto \sqrt{\eta/\xi}$, which defines an effective range of hydrodynamic

interactions. The limit $\lambda \gg R$, where R is the scale of observation, is referred to as the "wet" limit, for which hydrodynamic interactions are long-ranged, and the limit $\lambda \ll R$ as the "dry" limit, for which hydrodynamic interactions are screened out. The study of 2D active wetting in[117] was applied to situations in the "wet" limit. In that case, it was shown that $L_p^* \sim R$, with R being the radius of a circular monolayer, so the wetting transition defined a critical radius R^*, such that $R > R^*$ implied spreading (wetting) and $R < R^*$ implied retraction (dewetting). The existence of a critical radius illustrates the non-local character of the "wet" limit, in the sense that, in contrast to classical wetting theory, the advance or recession of the front is not determined locally, but by the system as a whole. More recently, in[145], it has been shown that, in the "dry" limit, when friction forces are dominant over viscosity, then $L_p^* \sim \lambda$. In this case, there is no critical size for the wetting/dewetting transition. In this limit the advance or recession of the front is determined by the local conditions, irrespective of what happens in other parts of the tissue. For intermediate situations between the two limits, the prediction of the model is more complicated and must be found numerically, since an explicit analytical expression is usually unavailable. More details on analytical predictions and numerical solutions for a variety of situations can be found in[70,117,145].

The 2D problem with radial symmetry (a circular monolayer), for which the fields depend on the radial coordinate only, is physically very similar to a 2D problem with translational invariance in one direction, which depends on one cartesian coordinate only. We refer to this semi-infinite case the as the 1D reduction of the problem. The physics of the wetting transition is indeed the same in this 1D formulation, at least when the radius R of the circular monolayer is not too small, and predictions differ typically on geometrical factors. The analysis of the 1D reduced problem, however, is much simpler in particular to study situations driven by external gradients, either chemical or mechanical, such as in the study of durotaxis. This rectangular geometry was studied experimentally[195], and analytically in the context of monolayer durotaxis in[70,195], and has been systematically exploited to obtain explicit approximations and numerical results in a variety of situations in[145]. All our numerical and analytical calculations in the present work have also been carried out for simplicity in this 1D effective reduction of the radially symmetric 2D problem.

In the 1D formulation along the x-direction, Equations 3-5 reduce to

$$2\eta \partial_x^2 v = 2\zeta p \partial_x p + \xi v - \zeta_i p,$$

Equation 6

where

$$p(x) = \frac{\sinh\big((x - X)/L_c\big)}{\sinh(R/L_c)}$$

Equation 7

with X being the instantaneous position of the center-of-mass position. To obtain the full spatial velocity profile $v(x)$ we need to solve Equation 6 assuming appropriate boundary conditions for the stress tensor. For cell monolayers one may assume stress-free boundary conditions, but to account for the out-of-plane contribution of surface tension in the case of 3D cell clusters (see Equation 11) we will modify this condition, as explained in section 1.4. With the two edges of the monolayer at positions x_+ and x_-, the instantaneous center-of-mass will be given by $X \equiv (x_+ + x_-)/2$ and its radius by $R \equiv (x_+ - x_-)/2$. With the solution of the velocity profile $v(x)$ at a given time, the velocity of the center-of-mass v_X and the spreading velocity v_S are simply

$$v_X \equiv \dot{X} = \frac{v(x_+) + v(x_-)}{2}, \quad v_S \equiv \dot{R} = \frac{v(x_+) - v(x_-)}{2}.$$

Equation 8

In the absence of an external gradient we have $v_X = 0$. However, v_S may be positive, when the monolayer is spreading (wetting), or negative when it is retracting (dewetting). The 2D wetting transition is thus defined by $v_S = 0$.

It is particularly informative to express the solution of v_S obtained in the 1D reduced case in both wet and dry limits, assuming $L_c \ll R$,. With the specific definitions $L_p = |\zeta|/(2\zeta_i)$ and $\lambda = \sqrt{2\eta/\xi}$, the spreading velocity in the absence of an external gradient (for stress-free boundary conditions), reads, in the two corresponding limits[145],

$$v_S^{wet} \approx \frac{L_c \zeta_i}{2\eta}(R - L_P)$$

Equation 9

$$v_S^{dry} \approx \frac{L_c \zeta_i}{2\eta}(\lambda - L_P)$$

Equation 10

(general exact expressions can be found in Appendix A in[145].

1.4 Generalized Young-Dupré equilibrium condition

In the present model we extend the theory of active wetting to 3D cell clusters, modelled as liquid droplets with surface tension γ and shaped as spherical caps. We have seen that, for stress-free boundary conditions, the basal monolayer either retracts or spreads indefinitely. However, for 3D droplets, the surface tension γ introduces an additional force, tangent to the liquid free surface. As a consequence, an additional horizontal force component must enter the balance between contractility and traction, and this additional contribution will favour spreading or retraction depending on the contact angle θ. For $\theta > 90°$ the tension will favour spreading/wetting, while for $\theta < 90°$ the tension will favour retraction/dewetting. Consequently, for sufficiently large surface tension, we may expect that a stable equilibrium will be reached for a finite contact angle θ, for which all active forces are balanced. In classical wetting theory, the equilibrium contact angle is determined by the Young-Dupré condition, which establishes the balance of the three surface tension forces tangent to the three surfaces at the contact line. In the context of cell aggregates, a similarly energetic approach has been proposed to define the wetting conditions in terms of the balance of the different adhesion energies at play[157,188].

In our approach here, following[117], the contributions from equilibrium properties of the interfaces are assumed to be negligible in front of the active contributions. In this context, we propose a generalized Young-Dupré condition defined by a balance of the active forces. Note that in our case both contractile stresses and traction forces are distributed in the polarized layer of thickness L_c, and this balance is, in general, non-local, as described in our 2D model for the basal monolayer. However, the additional contribution from surface tension enters as a local force at the contact line, and consequently, we can include it in our non-local force balance in the form of a boundary condition. In place of the stress-free boundary condition, we then impose,

$$\sigma_{\alpha\beta} n_\beta = -\frac{\gamma}{R} \cos\theta = \pm \frac{\gamma}{R} \sqrt{1 - \left(\frac{R}{R_{\text{sphere}}}\right)^2},$$

Equation 11

where n_β is the unit normal vector at the monolayer edge and the $+$ and $-$ are the conditions for $\theta > 90°$ and $\theta < 90°$ respectively. In turn, the vertical component of the surface tension is balanced by the Young-Laplace pressure $P = 2\gamma/R_{\text{sphere}}$ as a normal force exerted by the substrate on the liquid droplet. Consequently, we may infer the value of γ by measurements of vertical traction forces (Figure 4-8), which provide a direct measurement of P (Figure Appendix 2-4 d).

The equilibrium contact angle will be determined by the condition $v_S = 0$ when the equations are solved with the boundary condition Equation 11 (Figure 4-13 a). In situations where the 2D active wetting transition predicts dewetting, an equilibrium contact angle $\theta^* > 90°$ will be reached, a situation that is referred to classically as *low wettability*. On the contrary, whenever the 2D model would predict spreading of basal monolayer, the equilibrium contact angle $\theta^* < 90°$ will correspond to the *high wettability* case. From this analysis we see that the active wetting transition of the 2D problem defines the situation with contact angle $\theta = 90°$, for which $v_S = 0$ with no horizontal component of the tension γ. Therefore, we may refer to the point with $\theta^* = 90°$ in the 3D problem as the location of the wetting transition, in the sense that it corresponds to the location of the active wetting transition in the associated 2D problem. Accordingly, the passing through the $\theta^* = 90°$ does not imply an equivalent dynamical transition in 3D.

Similarly, the equilibrium contact radius R^*, will satisfy $\theta^* = 180 - \arcsin(R^*/R_{\mathrm{sphere}}) > 90°$ for low-wettability clusters or $\theta^* = \arcsin(R^*/R_{\mathrm{sphere}}) < 90°$ for high-wettability clusters. Clusters with a contact radius $R < R^*$ will be dewetting whereas if $R > R^*$ they will be wetting the substrate. An approximate expression of the equilibrium contact radius for low-wettability (in the absence of external gradients) taking the limits $R \leq L_c \leq$ and $R \leq R_{\mathrm{sphere}}$, takes the form

$$R^* \approx \frac{R_{\mathrm{sphere}}^2}{2\zeta_i R_{\mathrm{sphere}}^2 - 3\gamma}\left(|\zeta| - \sqrt{\zeta^2 - \frac{6\gamma}{R_{sphere}^2}\left(2\zeta_i R_{sphere}^2 - 3\gamma\right)}\right),$$

Equation 12

which increases for an increasing ζ_i, upon reaching $R^* = R_{\mathrm{sphere}}$ for a right angle cluster. Therefore, the equilibrium contact angle decreases with the traction value. The above expression is just an analytical approximation for certain parameter ranges. The exact value must be found numerically and it is shown for instance in Figure 4-13 c as a function of the stiffness of the substrate. For more complex traction and friction dependencies with stiffness see section 2. For initial conditions that are not at the equilibrium, our model predicts the evolution towards the equilibrium contact angle. In Figure Appendix 2-1 we show the evolution of the contact angle and for a variety of situations.

The determination of the contact radius R and the radius of the spherical surface R_{sphere} from experimental data differs depending on the wettability conditions. From the projection of the phase-contrast image of the cluster on the surface, one can measure the apparent cluster radius R_{proj} (Figure 4-13 a). Simple geometrical considerations imply that, for high-wettability clusters ($\theta < 90°$) we have $R = R_{\mathrm{proj}} < R_{\mathrm{sphere}}$ whereas, for low-wettability clusters ($\theta > 90°$), we have $R < R_{\mathrm{proj}} = R_{\mathrm{sphere}}$.

Therefore, either R_{sphere} ($\theta < 90°$) or R (for $\theta > 90°$) must be inferred or estimated from additional considerations. For instance, a good estimation of R in the second case may be given by the equilibrium value R^*.
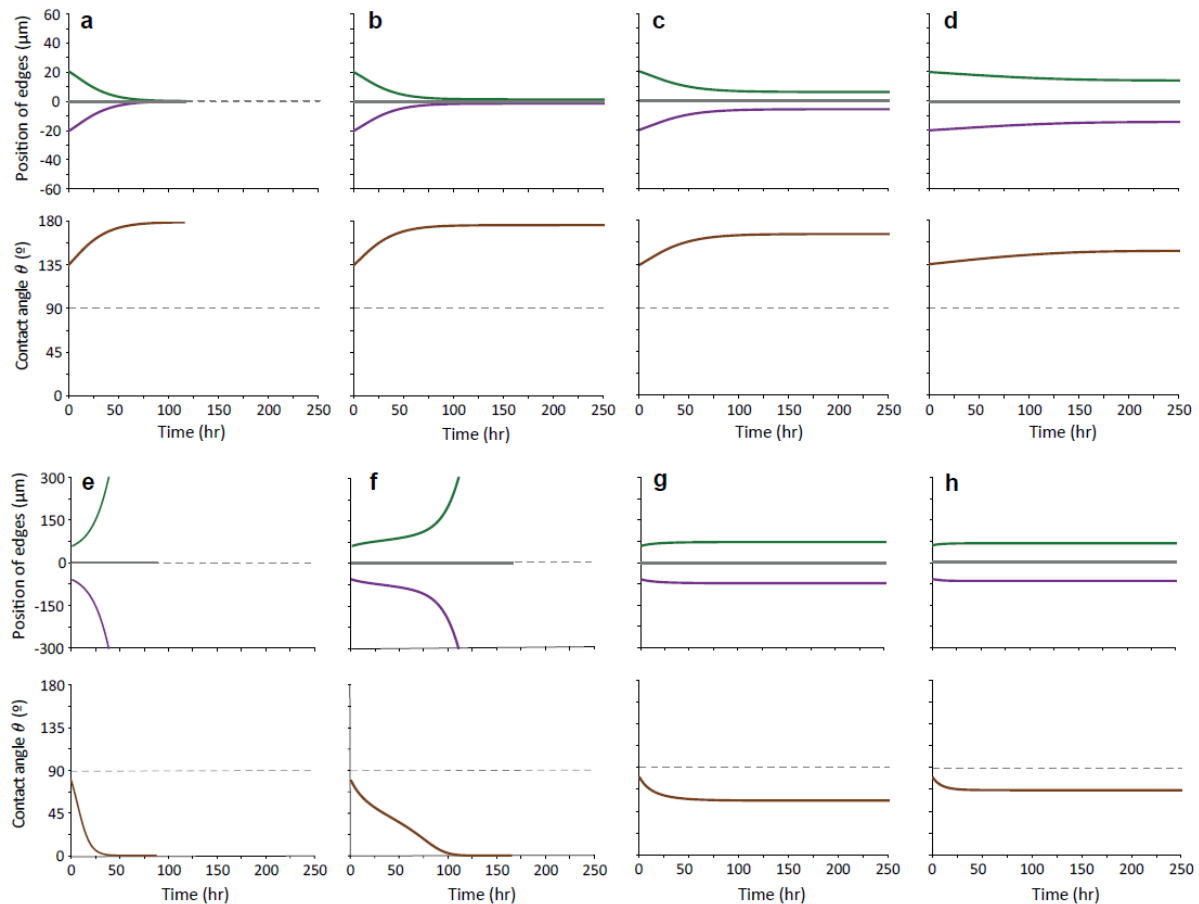

Figure Appendix 2-1. A stable equilibrium is reached for a sufficiently large surface tension γ. Evolution of the position of the edges (green for right and purple for left) and the contact angle of a cluster on a mono-stiffness substrate (computed with the analytical results for the cluster's velocity from[145]). Cluster's volume is constant, and the parameters are those from Table Appendix 2-1 except for $\zeta = -2$, a constant $\zeta_i = 0.05\ kPa/\mu m$ and friction $\xi = 0.2222\ kPa·s/\mu m^2$. Simulation time is $T = 500$ hours, and $\Delta t = 360s$. In a-d, initial conditions are $R(t = 0) = 20\ \mu m$ and $H(t = 0) = 50\ \mu m$, giving an initial contact angle $\theta(t = 0) = 136.4°$ (low-wettability). For $\gamma = 0\ mN/m$ (a), the cluster does a full dewetting (defined as such that reaches a contact radius $R \leq 0.1\ \mu m$) after 114.6 hours. Increasing the surface tension values to $\gamma = 0.8,3,6\ mN/m$, the cluster reaches a finite size $R^* = 1.41,5.91,14.20\ \mu m$ and angle $\theta^* = 177.16,168.03,150.24$ (b,c,d respectively). Similarly, in e-h the initial conditions are $R(t = 0) = 60\ \mu m$ and $H(t = 0) = 50\ \mu m$, giving an initial contact angle $\theta(t = 0) = 79.6°$. For $\gamma = 0\ mN/m$ (e), it evolves to a full wetting (defined as such that reaches a height $H \leq 0.1\ \mu m$) after 87 hours. Increasing the surface tension values to $\gamma = 40,50,60\ mN/m$ (f,g,h respectively), the cluster reaches a finite size only if γ is enough strong, with $R^* = 72.55,66.36\ \mu m$ and angle $\theta^* = 55.91,67.0$ (in g and h). In f), it reaches the full wetting state at 164 hours. For larger γ, larger R^* if the equilibrium relaxes to a low-wettability cluster ($\theta > 90°$), whereas smaller R^* if it relaxes to a high-wettability cluster ($\theta < 90°$).

2. Collective durotaxis of 3D clusters

2.1 Stiffness gradient and durotaxis for 2D monolayers

	Description	Typical value
h	monolayer height	5 μm
L_c	nematic length	15 μm
η	viscosity	20 MPa·s
ζ	contractility	-5 kPa
λ	hydrodynamic length	424.266 μm
E_0	substrate's softest stiffness	0.5 kPa (Fig. 2a)
E'	stiffness gradient	0.0332 kPa/μm (Fig. 2a)
E^*	characteristic stiffness of saturation	140 kPa
ζ_i^∞	traction saturation value	0.2 kPa/μm
ξ^∞	friction saturation value	0.2 kPa·s/μm^2
ξ_0	friction at $E \to 0$	0.2222 kPa·s/μm^2
P_0	bare pressure	$4.2 \cdot 10^{-3}$ kPa
P'	pressure gradient	$1.5 \cdot 10^{-3}$ kPa/μm

Table Appendix 2-1. Symbols and typical values of model parameters.

We now consider the presence of a stiffness gradient in the substrate to model collective durotaxis of cell clusters. Parameters that encode tissue-substrate interactions will generically depend on the local stiffness of the substrate, and their actual relationship must be determined independently of the hydrodynamic model. Following previous work, we assume that both friction and traction parameters saturate to maximal values at large stiffness due to biological limitations of the cells[77,177–181], so one may consider profiles of the generic form

$$\zeta_i(E) = \zeta_i^\infty \frac{E}{E + E^*}, \quad \xi(E) = \xi^\infty \frac{E}{E + E^*} + \xi_0$$

Equation 13

where ζ_i^∞ and ξ^∞ are saturation values, and E^* is a characteristic stiffness of force saturation. The ξ_0 value is only added in some cases, when we are at very low stiffness values, to avoid the strict "wet" limit $\lambda \to \infty$ ($\xi \to 0$), which is ill-defined for the case of a nonzero traction gradient, since global force balance cannot be satisfied in the absence of friction. In our experimental measurements, not only radial in-plane tractions increase with substrate stiffness but also out-of-plane tractions (Figure 4-8). Due to a lack of other experimental evidence of out-of-plane tractions with stiffness, we assume a linear increasing function of the pressure -and hence surface tension- with E,

$$P(E) = P_0 + s_p E,$$

Equation 14

$$\gamma(E) = \frac{R_{\text{sphere}}}{2} P(E) = \gamma_0 + \ell_\gamma E,$$

Equation 15

where $\gamma_0 = P_0 R_{\text{sphere}}/2$ is the bare surface tension, and $\ell_\gamma = s_P R_{\text{sphere}}/2$ is the stiffness response length of a surface tension. Note that in cases where the radius of the spherical cap is not constant (either for constant volume V or constant projected radius $R_{\text{proj.}}$ plots), γ_0 and ℓ_γ are not constant. Since P is the quantity directly measured in experiments, we will usually parametrize variations of other quantities in terms of P. For simplicity, we will always assume a linear stiffness profile with the position on the gel $E(x) = E_0 + E'x$, being E_0 and E' the stiffness offset and gradient, respectively. Then,

$$P(x) = P_{0,x} + P'x = \left(P_0 + s_p E_0\right) + s_p E'x$$

Equation 16

$$\gamma(x) = \gamma_{0,x} + \gamma'x = (\gamma_0 + \ell_\gamma E_0) + \ell_\gamma E'x.$$

Equation 17

In some cases, to reduce the number of parameters and gain physical insight, it is convenient to consider traction and friction as linear increasing functions with stiffness, or equivalently, with the position on the gel:

$$\zeta_i(x) = \zeta_i^0 + \zeta_i'x, \quad \xi(x) = \xi_0 + \xi'x.$$

Equation 18

Analytical solutions for the velocity field were obtained in[145] in the simplest situation, that is solving Equation 6 with a constant traction gradient $\zeta_i' > 0$ and with constant friction ($\xi' = 0$). In the dry and wet limits, and assuming $L_c \ll R$, the center-of-mass velocity does not depend on the boundary conditions of the stress-tensor and gives

$$v_s^{dry} \approx \frac{L_c\lambda}{2\eta}R\zeta_i' = \frac{L_c\lambda}{4\eta}(\zeta_i^+ - \zeta_i^-),$$

Equation 19

$$v_s^{wet} \approx \frac{L_c\zeta_i}{2\eta}(\lambda^2 + \frac{R^2}{3}) \approx \frac{L_c\lambda^2}{2\eta}\zeta_i',$$

Equation 20

where $\zeta_i^{\pm}$ are the local values of the traction at the respective edges. In both cases, the spreading velocity is the same that in the mono-stiffness situations, $v_S^{dry/wet} = v_S^{u,dry/wet}(\zeta_i(X))$, with $\zeta_i(X)$ the traction at the center-of-mass X. In the dry limit, the spreading dynamics is local in the sense that the two edges behave independently from the other, and the traction difference then directly drives tissue durotaxis. However, in the wet limit the velocity depends on the system size R and the traction gradient ζ_i', which illustrates that the two edges are hydrodynamically coupled. As a reference for the discussion of the following sections, it is important to remark that for a constant traction gradient and for constant friction, the durotactic velocity of a 2D monolayer does not depend on the traction offset (and hence the local stiffness)[145]. As we will see in the following sections, the contribution from the out-of-plane surface tension will produce the increase of v_X with the stiffness offset, and both the introduction of a gradient of the friction coefficient $\xi' > 0$ and the saturation of traction with stiffness will both contribute to the decrease of v_X at larger stiffness.

2.2 Non-monotonic behaviour of durotaxis for 3D clusters

The presence of a stiffness gradient generically produces a durotactic response, with v_X being the durotactic velocity[70,145] ($v_X > 0$, directed to stiffer regions of the substrate). Consistent with the experimental results (Figure 4-10, Figure 4-11), and for more realistic traction and friction dependencies with stiffness than those assumed for deriving Equation 19 and Equation 20, we observe a non-monotonic behaviour of v_X with the stiffness of the substrate, for clusters of the same experimentally measured size $R_{proj.}$. This is understood as a competition between two mechanisms, which make the velocity either increase or decrease, determining an optimal velocity of durotactic migration in an intermediate stiffness.

Focusing on the results for the 2D monolayer without introducing the out-of-plane surface tension ($\gamma = 0$), the effect of changes in tissue size R and active traction difference between the stiff and soft edges $\Delta\zeta_i$ are illustrated in Figure Appendix 2-2. Importantly, v_X increases both with R (Figure Appendix 2-2 a,d, and Figures 6 and 7a in[145] for the analytical results), and with $\Delta\zeta_i$ (Figure Appendix

2-2 b). In fact, an increase in size brings to an increase in the active traction difference, although not in a linear relationship with the stiffness since it depends on the position or local stiffness value, and so the velocity increases. However, for the same $\Delta\zeta_i$, we can see that v_X is larger for smaller tissues (Figure Appendix 2-2 b). This is because with a saturated active traction increase with stiffness, if $R_1 < R_2$ and $\Delta\zeta_i(R_1, E_1) = \Delta\zeta_i(R_2, E_2)$, necessarily the stiffness offsets obey $E_1 < E_2$ (Figure Appendix 2-2 c), and so the local traction gradient is larger for the smaller tissue. Since v_X increases with local traction gradient (Figure 7d in[145] and Equation 9 for the analytical results), this corresponds to a velocity increase.

All in all, the decrease in velocity v_X with stiffness offset is explained irregardless of the wettability of the 3D droplet (Figure Appendix 2-2 a,d), due to both a decrease in traction difference and local traction gradient with E (Figure Appendix 2-2 c), and a friction increase. In Figure Appendix 2-3 a and Figure Appendix 2-4 b, we can see how this decrease is controlled by the friction increase and the characteristic stiffness of force saturation E^*, respectively. For simplicity in the interpretation of results, the active traction and friction are linear functions of E in Figure Appendix 2-3, but qualitatively, the tendencies are equal than those assuming saturated profiles, with the obvious effect of saturation which brings the system asymptotically to the uniform case, that is, with vanishing v_X due to a symmetric behaviour of both edges of the basal monolayer, and hence no durotaxis.

On the other hand, the increase in velocity must be deciphered making use of our 3D active wetting theory. Low stiffness corresponds to low-wettability clusters, with $\theta > 90°$ (Figure 4-13 c, is consistent with experimental measurements in Figure 4-8). Thus, the equilibrium contact radius R^* is small, and from what we argued before, this implies a small velocity. Increasing the stiffness, the contact angle decreases and so R^* increases (Figure Appendix 2-4 c,f), yielding to faster durotaxis. As it affects the contact angle, surface tension γ (and thus pressure P) controls the velocity increase, as we see in Figure Appendix 2-3 b and Figure Appendix 2-4 e.
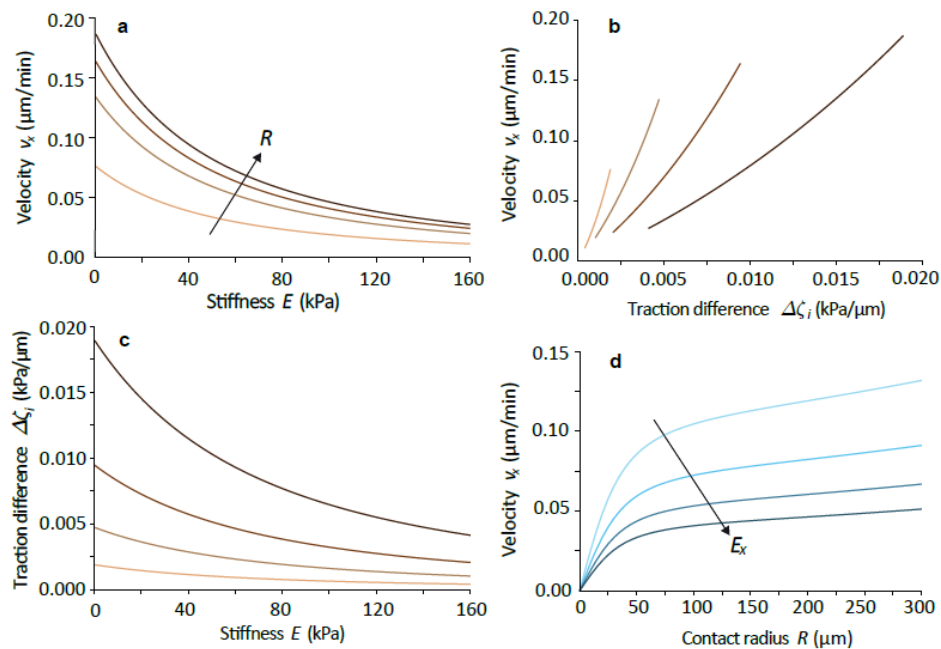
Figure Appendix 2-2. The durotactic velocity increases with contact radius R and traction difference $\Delta\zeta_i$ and decreases with stiffness, irrespective of the wettability of the 3D droplet. *(a,b) v_X versus stiffness E (a) or active traction difference $\Delta\zeta_i$ (b), for a fixed contact radius in each curve, with values $R = 20,50,100,200$ μm, from lighter to darker brown. (c) $\Delta\zeta_i$ decreases as the stiffness offset increases, since we are reaching the saturation zone, and the difference is larger for larger sizes. (d) v_X versus contact radius R, for a fixed stiffness offset in each curve with values $E_X = 25,50,75,100$ kPa, from lighter to darker blue. Saturated active traction and friction profiles with stiffness are assumed, $\gamma = 0$, and the other model parameters are in Table Appendix 2-1.*
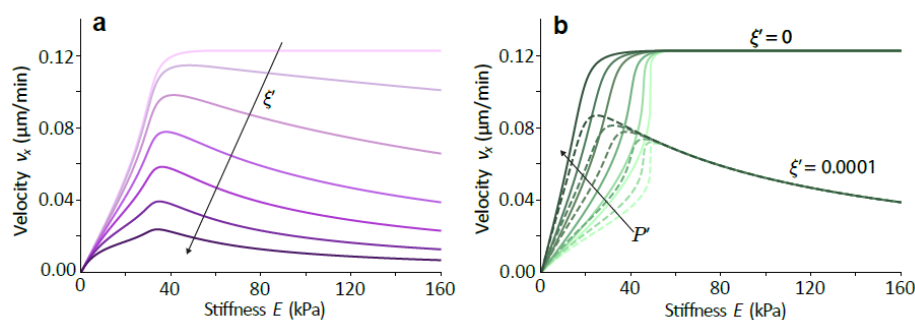

Figure Appendix 2-3. Non-monotonic behaviour of the durotactic velocity, assuming linear active traction and friction functions with stiffness. *v_X versus stiffness E, for a cluster with a fixed $R_{proj.} = 45$ μm, assuming linear traction, friction and pressure (hence surface tension) profiles. (a) Effect of an increasing friction gradient $\xi' = (0,1,4,8,10,20,40,80) \cdot 10^{-5}$ kPa·s/μm² (from lighter to darker purple). Effect of an increasing pressure gradient $P' = (7,8,10,15,20,25,30) \cdot 10^{-4}$ kPa/μm (from lighter to darker green), either with a constant friction (continuous lines, not presenting a decrease in v_X) or with a friction gradient of $\xi' = 0.0001$ kPa·s/ μm² (dashed lines). Model parameters are those in Table Appendix 2-1.*
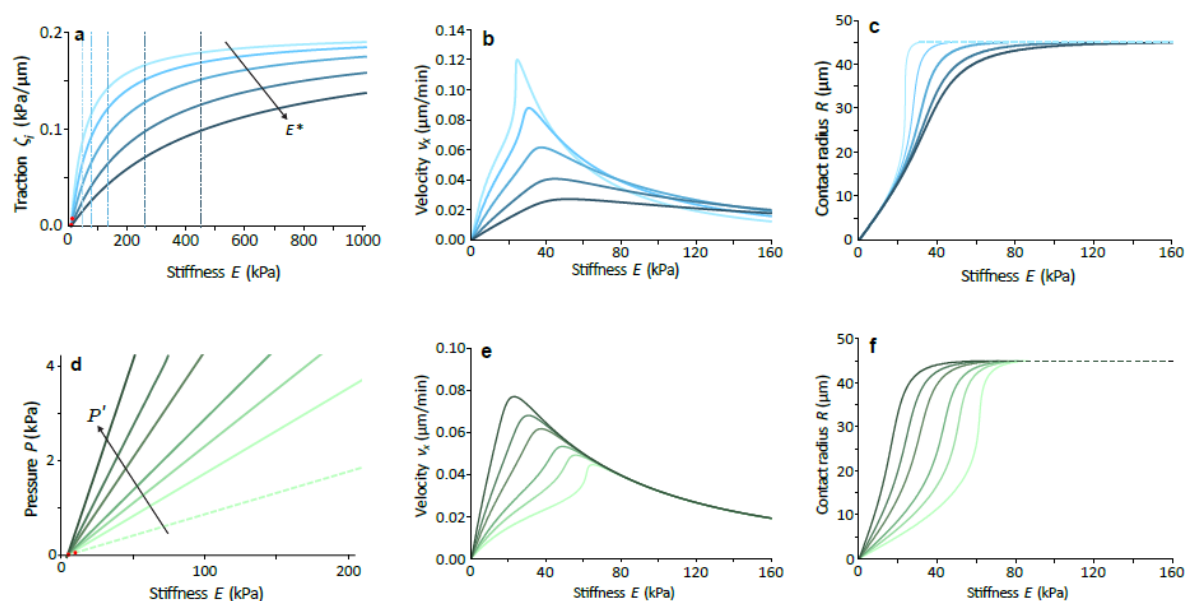
Figure Appendix 2-4. Non-monotonic behaviour of the durotactic velocity, assuming saturated active traction and friction functions with stiffness. *(a,d)Traction and pressure profiles with stiffness, changing the saturation crossover stiffness $E^* = 50,80,140,260,450\ kPa$ (form lighter to darker blue) in (a) and the increase of pressure slope $P' = (6,8,10,15,20,25,30) \cdot 10^{-4}kPa/\mu m$ (from lighter to darker greens) in (d). The two red points correspond to the average of the experimental values from Figure 4-8. (b, e) v_X versus stiffness E, for a cluster presenting a fixed $R_{proj.} = 45\ \mu m$, with saturated profiles for traction and friction (a) and linear pressure (and hence surface tension) (d). The saturation of cellular forces at high stiffness is characteristic of the v_X decrease, whereas the effect of three-dimensional active wetting, controlled by the pressure (equivalently surface tension), is characteristic of the v_X increase. (c,f) Corresponding stable contact radius R for each case. The point where the continuous and the dashed line of the same colour meet represents the critical 2D active wetting transition ($R = R_{proj.}$ and so $\theta = 90°$). Other model parameters are those in Table Appendix 2-1.*

2.3 Interplay of model parameters on the durotactic velocity

As seen in our experimental results (Figure 4-8), durotaxis depends on other variables such as cluster size, cell contractility and stiffness gradient. In our model, those parameters play an important role in determining the wetting transition and thus the stable contact radius R at each stiffness offset, and so they affect the durotactic migration of the clusters. The interplay of the cluster size, contractility and stiffness gradient in the model is shown in Figure Appendix 2-5.

An increasing projected size of the clusters increases the velocity magnitude (Figure Appendix 2-5 a,d), consistent with our experimental results (Figure 4-11), in spite of the displacement of the peak of the velocity. Experimentally, we find that this peak is localized towards higher stiffness offsets for clusters bigger than than 60 µm in diameter, in comparison to smaller clusters. According to the model this peak is displaced towards softer offsets since the wetting transition takes places sooner for larger clusters.

Decreasing (or inhibiting) the contractility $|\zeta|$, we predict a displacement to lower stiffness offsets of the peak of the velocity (Figure Appendix 2-5 b,e), consistent with our experimental results (Figure 4-12). However, the magnitude is increased in the model whereas decreased in experiments. A plausible explanation for this discrepancy is that the ROCK inhibitor used to partially inhibit cell contractility might be reducing traction forces as well, and so the model should contemplate a reduced parameter ζ_i, which would lower the velocity. Another reason could be the sampling window that is looked at in the experiments. At 6 kPa with a fibronectin coated substrate, many clusters are already wetting the substrate and so the fraction of clusters near the wetting transition or dewetting it are just a few. Thus, when doing the average (taking into account all the wet clusters as well), the magnitude of the velocity is lowered. However, when increasing contractility with EGF, there are many more dewetting clusters or at least closer to the transition, which makes the velocity to increase.
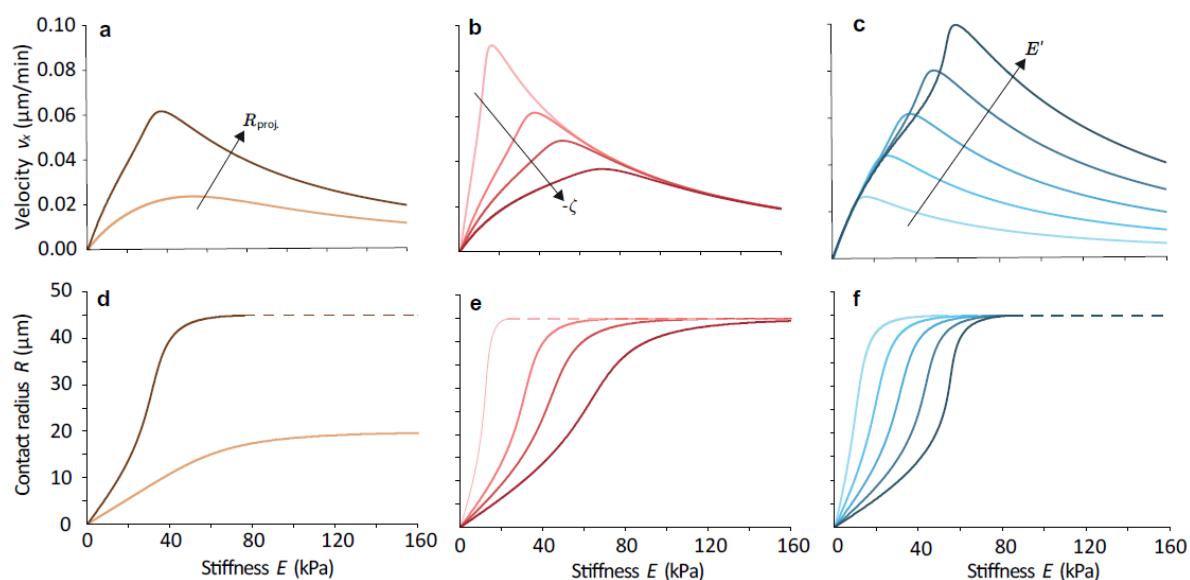

Figure Appendix 2-5. The durotactic velocity depends on cluster size, cell contractility and stiffness gradient. v_X and corresponding stable contact radius R against stiffness offset E, for a cluster with fixed $R_{proj.}$, assuming saturated profiles for traction and friction and a linear pressure. The point where the continuous and the dashed line of the same colour meet (in d-f) represents the critical 2D active wetting transition $R = R_{proj.}$ and so $\theta = 90°$). In (a,d), the projected radius is $R_{proj.}$ = 20,45 µm, and so velocity is larger for bigger clusters. In (b,e), contractility values are $\zeta = -2,-5,-7,-10$ kPa, and so velocity is smaller for more contractile clusters, having the peak displaced towards stiffer offsets. In (c,f), stiffness gradients are $E' = 0.01,0.02,0.03,0.05,0.07$ kPa/µm, yielding to an increase of velocity and displacement of its peak towards stiffer offsets for larger stiffness gradients. The constant model parameters in each case are those in Table Appendix 2-1.

Finally, the stiffness gradient of the gel affects both the traction and friction offset but in a nontrivial way. In the experiments it is seen how a larger stiffness slope increases the magnitude of the durotactic velocity (Figure 4-12). According to our model, not only this is true but also the peak of durotaxis is displaced towards stiffer offsets (Figure Appendix 2-5 c,f). Even if the wetting transition occurs at the same offset, a larger difference of stiffness at both edges yields to a lower contact radius R in the low-wettability region. However, this is compensated with the fact that we have larger

traction values, and so the velocity is not decreased in these regions for larger stiffness gradients. Once the wetting state is reached, then the latter effect is the only one important, and so the durotactic velocity is larger for larger stiffness gradients.

2.4 Dynamics of migrating clusters

Our model explains the non-monotonic durotactic behaviour of tissues placed at different stiffness, but we can also use it to predict the evolution of a migrating cluster towards stiffer regions. Through time-integration of the velocity, we obtain the dynamics and shape over time of a cluster with a constant volume. Apart from the typical evolution (Figure 4-13 e,f which corresponds to Figure Appendix 2-6 d), we show the effect of changing other model parameters in the dynamics, such as the initial stiffness offset (Figure Appendix 2-6), the contractility (Figure Appendix 2-7 a,b), the pressure offset (Figure Appendix 2-7 c,d) or the pressure gradient (Figure Appendix 2-8).

The non-monotonic behaviour of the durotactic velocity for these migrating clusters is understood in a similar way as we argued for static plots of clusters with constant $R_{\mathrm{proj.}}$ (Figure Appendix 2-3-5): a cluster which starts with a low wettability at a soft region of the substrate, advances towards stiffer regions increasing its wettability (lowering the contact angle θ) and so expanding the contact radius R, hence increasing its durotactic velocity. It slows down when it reaches a high wettability on stiff substrates, where the relative importance of friction increase is higher.

However, in many cases, we can see an initial decrease of the velocity, corresponding to a decrease of the contact radius R. This happens when in the initial stages of the evolution, the cluster (which both in Figure Appendix 2-6, Figure Appendix 2-7 and Figure Appendix 2-8 starts in a low-wettability configuration with $\theta = 136.4°$), is under conditions of contraction of its basal radius, that is, presenting a negative spreading velocity $v_S < 0$. In a softer initial position (Figure Appendix 2-6), with higher contractility (Figure Appendix 2-7 a,b) or with smaller values of the pressure and thus the surface tension (Figure Appendix 2-7 c,d and Figure Appendix 2-8), this effect is accentuated, since all those parameters favour the "dewetting" of the cluster. Instead, a larger pressure minimizes this effect because it favours the expansion of R instead of its contraction at the initial stages and when $\theta > 90°$.

Finally, if the pressure does not increase with stiffness (Figure Appendix 2-7 c,d), it does not difficult that much the expansion of the cluster once in a high-wettability state ($\theta < 90°$), and the contact size keeps increasing (note that v_S is not exactly zero in those cases). Nevertheless, the decrease of durotactic velocity is still present due to the increase of friction forces.

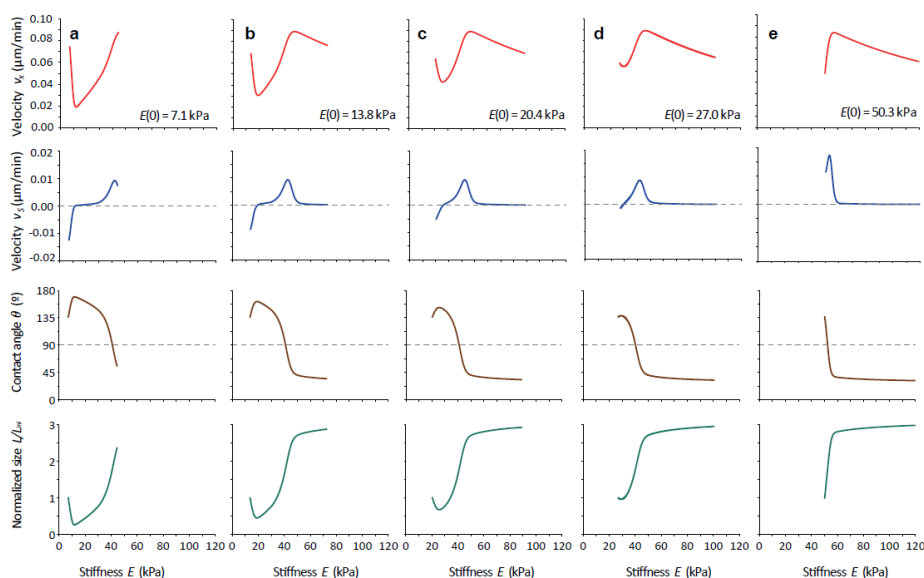Observing and characterizing this full dynamical evolution in experiments remains a challenge for future work.

Figure Appendix 2-6. Dynamics of a migrating cluster when varying the initial stiffness offset. *Evolution assuming a linear traction, friction and pressure profiles, with $\zeta_i^0 = 0.00068 kPa/\mu m$, $\zeta_i' = 0.00005 kPa/\mu m^2$, $\xi^0 = 0.2222\ kPa·s/\ \mu m^2$, $\xi' = 0.0001 kPa·s\ \mu m^3$, $P_0 = 0.0042\ kPa$ and $P' = 0.0006\ kPa/\mu m$. Simulation time is $T = 500\ hours$ and $\Delta t = 360\ s$. The other values are the same as in Table Appendix 2-1, except for $\zeta = -2$. Initial conditions are $R(t = 0) = 20\ \mu m$ and $H(t = 0) = 50\ \mu m$, giving a low-wettability state with $\theta(t = 0) = 136.4°$, and the initial stiffness offset changes to $E_X(t = 0) = 7.1, 13.8, 20.4, 27.0$ and $50.3\ kPa$.*

Figure Appendix 2-7. Dynamics of a migrating cluster when varying the contractility and pressure. *Evolution assuming a linear traction, friction and pressure profiles, with $\zeta_i^0 = 0.00068\ kPa/\mu m$, $\zeta_i' = 0.00005\ kPa/\ \mu m^2$, $\xi^0 = 0.2222\ kPa·s/\ \mu m^2$ and $\xi' = 0.0001\ kPa·s/\ \mu m^3$. Simulation time is $T = 500\ hours$ and $\Delta t = 360\ s$. The other values are the same as in Table Appendix 2-1. Initial conditions are $R(t = 0) = 20\ \mu m$ and $H(t = 0) = 50\ \mu m$, giving a low-wettability state with $\theta(t = 0) = 136.4°$, and $E_X(t = 0) = 27.0\ kPa$. In (a-b), $P_0 = 0.0042\ kPa$ and $P' = 0.0006\ kPa/\mu m$ and the contractility is either $\zeta = -3$ or $-1\ kPa$ respectively. In (c-d), a constant pressure is assumed to be either $P = 0.55$ or $0.75\ kPa$, and the contractility is fixed to $\zeta = -2$. The plots can be compared as well with Figure Appendix 2-6 d.*
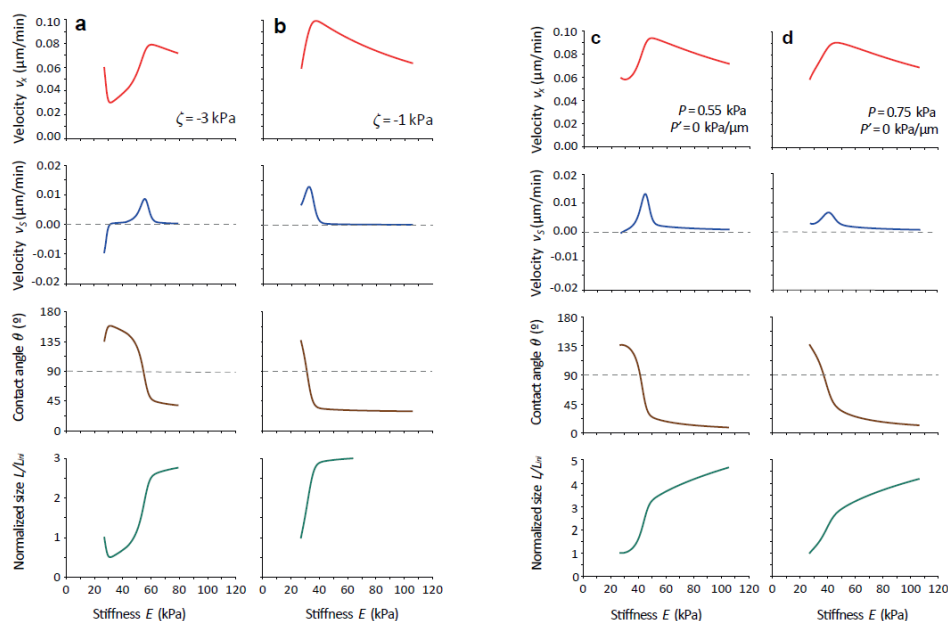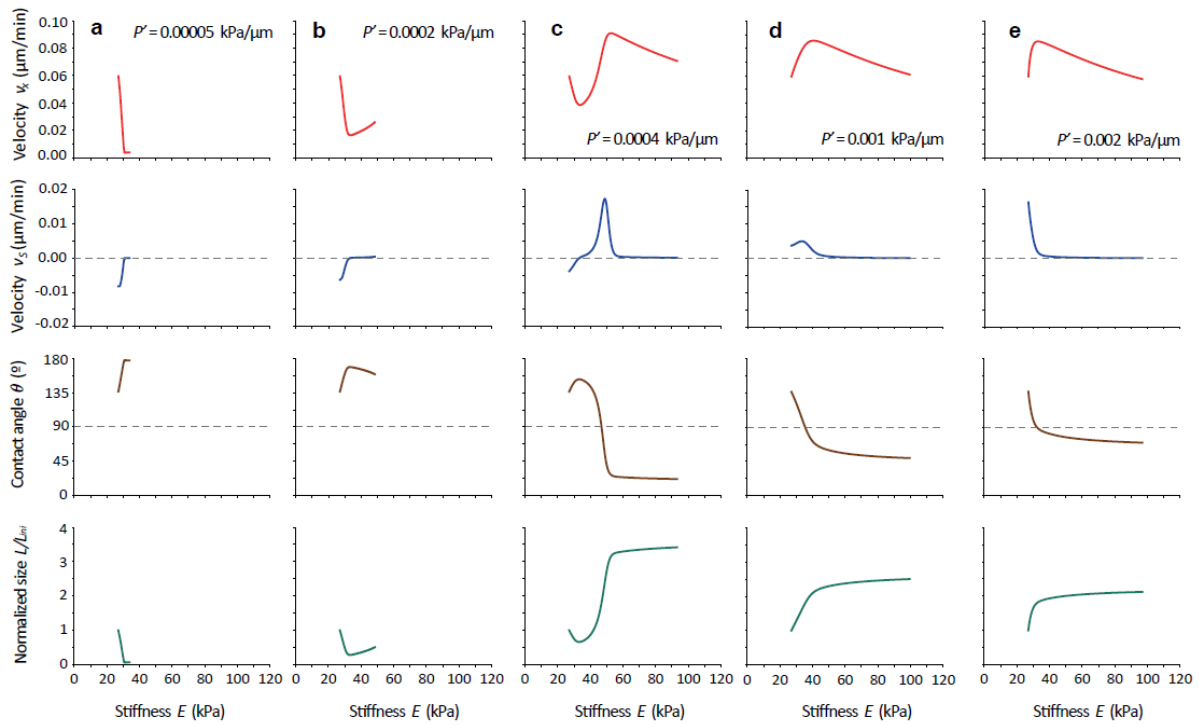
Figure Appendix 2-8. Dynamics of a migrating cluster when varying the pressure gradient. *Evolution assuming a linear traction, friction and pressure profiles, with $\zeta_i^0 = 0.00068$ kPa/μm, $\zeta_i' = 0.00005$ kPa/μm², $\xi^0 = 0.2222$ kPa·s/μm², $\xi' = 0.0001$ kPa·s/μm³, and $P_0 = 0.0042$ kPa. Simulation time is $T = 500$ hours and $\Delta t = 360$ s. The other values are the same as in Table Appendix 2-1, and $\zeta = -2$. Initial conditions are $R(t = 0) = 20$ μm and $H(t = 0) = 50$ μm, giving a low-wettability state with $\theta(t = 0) = 136.4°$. $E_X(t = 0) = 27.0$ kPa is fixed and the pressure gradient changes to $P' = (0.05, 0.2, 0.4, 1.0, 2.0) \cdot 10^{-3}$ kPa/μm. The plots can be compared as well with Figure Appendix 2-6 d.*

8. References

1.   DuChez, B. J., Doyle, A. D., Dimitriadis, E. K. & Yamada, K. M. Durotaxis by Human Cancer Cells. *Biophys J* 116, 670–683 (2019).

2.   Jin, T., Xu, X. & Hereld, D. Chemotaxis, chemokine receptors and human disease. *Cytokine* 44, 1–8 (2008).

3.   Prescott, T. P., Zhu, K., Zhao, M. & Baker, R. E. *Quantifying the impact of electric fields on single-cell motility*. bioRxiv 2021.01.22.427762 (2021).

4.   Alberts, B., et al. *Molecular Biology of the cell*. Sixth edition. ed. 2015, New York, NY: Garland Science, Taylor and Francis Group.

5.   Rafelski, S. M. & Theriot, J. A. Crawling toward a unified model of cell mobility: spatial and temporal regulation of actin dynamics. *Annu Rev Biochem* 73, 209–239 (2004).

6.   Petrie, R. J., Doyle, A. D. & Yamada, K. M. Random versus directionally persistent cell migration. *Nat Rev Mol Cell Biol* 10, 538–549 (2009).

7.   Bear, J. E. & Haugh, J. M. Directed migration of mesenchymal cells: where signaling and the cytoskeleton meet. *Curr Opin Cell Biol* 0, 74–82 (2014).

8.   Thüroff, F., Goychuk, A., Reiter, M. & Frey, E. Bridging the gap between single-cell migration and collective dynamics. *eLife* 8, e46842.

9.   Oberhofer, A. *et al.* Molecular underpinnings of cytoskeletal cross-talk. *PNAS* 117, 3944–3952 (2020).

10.   Uroz, M. *et al.* Traction forces at the cytokinetic ring regulate cell division and polyploidy in the migrating zebrafish epicardium. *Nat Mater* 18, 1015–1023 (2019).

11.   Fourriere, L., Jimenez, A. J., Perez, F. & Boncompain, G. The role of microtubules in secretory protein transport. *J Cell Sci* 133, jcs237016 (2020).

12.   Seetharaman, S. & Etienne-Manneville, S. Cytoskeletal Crosstalk in Cell Migration. *Trends Cell Biol* 30, 720–735 (2020).

13.   Garcin, C. & Straube, A. Microtubules in cell migration. *Essays Biochem* 63, 509–520 (2019).

14. Zhang, J., Guo, W.-H. & Wang, Y.-L. Microtubules stabilize cell polarity by localizing rear signals. *PNAS* 111, 16383–16388 (2014).

15. Tang, D. D. & Gerlach, B. D. The roles and regulation of the actin cytoskeleton, intermediate filaments and microtubules in smooth muscle cell migration. *Respir Res* 18, 54 (2017).

16. Sanghvi-Shah, R. & Weber, G. F. Intermediate Filaments at the Junction of Mechanotransduction, Migration, and Development. *Front Cell Dev Biol* 5, 81 (2017).

17. Blanchoin, L., Boujemaa-Paterski, R., Sykes, C. & Plastino, J. Actin dynamics, architecture, and mechanics in cell motility. *Physiol Rev* 94, 235–263 (2014).

18. Murrell, M., Oakes, P. W., Lenz, M. & Gardel, M. L. Forcing cells into shape: the mechanics of actomyosin contractility. *Nat Rev Mol Cell Biol* 16, 486–498 (2015).

19. Ananthakrishnan, R. & Ehrlicher, A. The forces behind cell movement. *Int J Biol Sci* 3, 303–317 (2007).

20. Oakes, P. W., Beckham, Y., Stricker, J. & Gardel, M. L. Tension is required but not sufficient for focal adhesion maturation without a stress fiber template. *J Cell Biol* 196, 363–374 (2012).

21. Humphries, J. D., Byron, A. & Humphries, M. J. Integrin ligands at a glance. *Journal of Cell Science* 119, 3901–3903 (2006).

22. Elosegui-Artola, A. *et al.* Mechanical regulation of a molecular clutch defines force transmission and transduction in response to matrix rigidity. *Nature Cell Biology* 18, 540–548 (2016).

23. Roca-Cusachs, P. *et al.* Integrin-dependent force transmission to the extracellular matrix by α-actinin triggers adhesion maturation. *PNAS* 110, E1361–E1370 (2013).

24. Hoffman, L., Jensen, C. C., Yoshigi, M. & Beckerle, M. Mechanical signals activate p38 MAPK pathway-dependent reinforcement of actin via mechanosensitive HspB1. *Mol Biol Cell* 28, 2661–2675 (2017).

25. López-Colomé, A. M., Lee-Rivera, I., Benavides-Hidalgo, R. & López, E. Paxillin: a crossroad in pathological cell migration. *Journal of Hematology & Oncology* 10, 50 (2017).

26. Schaller, M. D. & Parsons, J. T. pp125FAK-dependent tyrosine phosphorylation of paxillin creates a high-affinity binding site for Crk. *Mol Cell Biol* 15, 2635–2645 (1995).

27. Orr, A. W., Helmke, B. P., Blackman, B. R. & Schwartz, M. A. Mechanisms of Mechanotransduction. *Developmental Cell* 10, 11–20 (2006).

28. Kanchanawong, P. *et al.* Nanoscale architecture of integrin-based cell adhesions. *Nature* 468, 580–584 (2010).

29. Dumbauld, D. W. *et al.* How vinculin regulates force transmission. *PNAS* 110, 9788–9793 (2013).

30. Hoffman, L. M., Jensen, C. C., Chaturvedi, A., Yoshigi, M. & Beckerle, M. C. Stretch-induced actin remodeling requires targeting of zyxin to stress fibers and recruitment of actin regulators. *Mol Biol Cell* 23, 1846–1859 (2012).

31. Colombelli, J. *et al.* Mechanosensing in actin stress fibers revealed by a close correlation between force and protein localization. *Journal of Cell Science* 122, 1665–1679 (2009).

32. Sawada, Y. *et al.* Force sensing by mechanical extension of the Src family kinase substrate p130Cas. *Cell* 127, 1015–1026 (2006).

33. Oria, R. *et al.* Force loading explains spatial sensing of ligands by cells. *Nature* 552, 219–224 (2017).

34. Müller, C. & Pompe, T. Distinct impacts of substrate elasticity and ligand affinity on traction force evolution. *Soft Matter* 12, 272–280 (2016).

35. Elosegui-Artola, A., Trepat, X. & Roca-Cusachs, P. Control of Mechanotransduction by Molecular Clutch Dynamics. *Trends Cell Biol* 28, 356–367 (2018).

36. Kong, F., García, A. J., Mould, A. P., Humphries, M. J. & Zhu, C. Demonstration of catch bonds between an integrin and its ligand. *Journal of Cell Biology* 185, 1275–1284 (2009).

37. Elosegui-Artola, A. *et al.* Force Triggers YAP Nuclear Entry by Regulating Transport across Nuclear Pores. *Cell* 171, 1397-1410.e14 (2017).

38. Escribano, J. *et al.* A hybrid computational model for collective cell durotaxis. in *Biomech. model. mechanobiol.* (2018). doi:10.1007/s10237-018-1010-2.

39. Sunyer, R. *et al.* Collective cell durotaxis emerges from long-range intercellular force transmission. *Science* 353, 1157 (2016).

40. Lange, J. R. & Fabry, B. Cell and tissue mechanics in cell migration. *Experimental Cell Research* 319, 2418–2423 (2013).

41. Engler, A. J., Sen, S., Sweeney, H. L. & Discher, D. E. Matrix Elasticity Directs Stem Cell Lineage Specification. *Cell* 126, 677–689 (2006).

42. Butcher, D. T., Alliston, T. & Weaver, V. M. A tense situation: forcing tumour progression. *Nature Reviews Cancer* 9, 108–122 (2009).

43. Smith, L. R., Cho, S. & Discher, D. E. Stem Cell Differentiation is Regulated by Extracellular Matrix Mechanics. *Physiology (Bethesda)* 33, 16–25 (2018).

44. Even-Ram, S., Artym, V. & Yamada, K. M. Matrix Control of Stem Cell Fate. *Cell* 126, 645–647 (2006).

45. Gardel, M. L., Schneider, I. C., Aratyn-Schaus, Y. & Waterman, C. M. Mechanical Integration of Actin and Adhesion Dynamics in Cell Migration. *Annu Rev Cell Dev Biol* 26, 315–333 (2010).

46. Parsons, J. T., Horwitz, A. R. & Schwartz, M. A. Cell adhesion: integrating cytoskeletal dynamics and cellular tension. *Nat Rev Mol Cell Biol* 11, 633–643 (2010).

47. Gardel, M. L. *et al.* Traction stress in focal adhesions correlates biphasically with actin retrograde flow speed. *J Cell Biol* 183, 999–1005 (2008).

48. Mazur, A. J. *et al.* Modulation of actin filament dynamics by actin-binding proteins residing in lamellipodia. *Eur J Cell Biol* 89, 402–413 (2010).

49. Liu, Z. *et al.* Blebbistatin inhibits contraction and accelerates migration in mouse hepatic stellate cells. *Br J Pharmacol* 159, 304–315 (2010).

50. Cai, D. *et al.* Mechanical feedback through E-cadherin promotes direction sensing during collective cell migration. *Cell* 157, 1146–1159 (2014).

51. Mayor, R. & Theveneau, E. The role of the non-canonical Wnt–planar cell polarity pathway in neural crest migration. *Biochemical Journal* 457, 19–26 (2013).

52. Shellard, A. & Mayor, R. Collective durotaxis along a self-generated stiffness gradient in vivo. *Nature* (2021) doi:10.1038/s41586-021-04210-x.

53. Carvalho, L. & Heisenberg, C.-P. The yolk syncytial layer in early zebrafish development. *Trends in Cell Biology* 20, 586–592 (2010).

54. Fenteany, G., Janmey, P. A. & Stossel, T. P. Signaling pathways and cell mechanics involved in wound closure by epithelial cell sheets. *Current Biology* 10, 831–838 (2000).

55. Vassilev, V., Platek, A., Hiver, S., Enomoto, H. & Takeichi, M. Catenins Steer Cell Migration via Stabilization of Front-Rear Polarity. *Developmental Cell* 43, 463-479.e5 (2017).

56. Ladoux, B., Mège, R.-M. & Trepat, X. Front-Rear Polarization by Mechanical Cues: From Single Cells to Tissues. *Trends Cell Biol* 26, 420–433 (2016).

57. Wong, M. & Gilmour, D. Going your own way: Self-guidance mechanisms in cell migration. *Current Opinion in Cell Biology* 72, 116–123 (2021).

58. Gorelik, R. & Gautreau, A. Quantitative and unbiased analysis of directional persistence in cell migration. *Nat Protoc* 9, 1931–1943 (2014).

59. Ricoult, S. G., Kennedy, T. E. & Juncker, D. Substrate-Bound Protein Gradients to Study Haptotaxis. *Front Bioeng Biotechnol* 3, 40 (2015).

60. Espina, J. A., Marchant, C. L. & Barriga, E. H. Durotaxis: the mechanical control of directed cell migration. *The FEBS Journal* n/a,.

61. Lo, C. M., Wang, H. B., Dembo, M. & Wang, Y. L. Cell movement is guided by the rigidity of the substrate. *Biophys J* 79, 144–152 (2000).

62. Bray, D. Axonal growth in response to experimentally applied mechanical tension. *Dev Biol* 102, 379–389 (1984).

63. Yu, G., Feng, J., Man, H. & Levine, H. Phenomenological modeling of durotaxis. *Phys. Rev. E* 96, 010402 (2017).

64. Isenberg, B. C., Dimilla, P. A., Walker, M., Kim, S. & Wong, J. Y. Vascular smooth muscle cell durotaxis depends on substrate stiffness gradient strength. *Biophys J* 97, 1313–1322 (2009).

65. Vincent, L. G., Choi, Y. S., Alonso-Latorre, B., del Álamo, J. C. & Engler, A. J. Mesenchymal stem cell durotaxis depends on substrate stiffness gradient strength. *Biotechnol J* 8, 472–484 (2013).

66. Flanagan, L. A., Ju, Y.-E., Marg, B., Osterfield, M. & Janmey, P. A. Neurite branching on deformable substrates. *Neuroreport* 13, 2411–2415 (2002).

67. Zhu, M. *et al.* Spatial mapping of tissue properties in vivo reveals a 3D stiffness gradient in the mouse limb bud. *PNAS* 117, 4781–4791 (2020).

68. Liu, F. *et al.* Feedback amplification of fibrosis through matrix stiffening and COX-2 suppression. *J Cell Biol* 190, 693–706 (2010).

69. Ulrich, T. A., de Juan Pardo, E. M. & Kumar, S. The Mechanical Rigidity of the Extracellular Matrix Regulates the Structure, Motility, and Proliferation of Glioma Cells. *Cancer Res* 69, 4167 (2009).

70. Alert, R. & Casademunt, J. Role of Substrate Stiffness in Tissue Spreading: Wetting Transition and Tissue Durotaxis. *Langmuir* 35, 7571–7577 (2019).

71. Lavrentieva, A. *et al.* Fabrication of Stiffness Gradients of GelMA Hydrogels Using a 3D Printed Micromixer. *Macromolecular Bioscience* 20, 2000107 (2020).

72. Novikova, E. A., Raab, M., Discher, D. E. & Storm, C. Persistence-driven durotaxis: Generic, directed motility in rigidity gradients. *Phys Rev Lett* 118, 078103 (2017).

73. Hadden, W. J. *et al.* Stem cell migration and mechanotransduction on linear stiffness gradient hydrogels. *PNAS* 114, 5647–5652 (2017).

74. Yu, Y., Ren, L.-J., Liu, X.-Y., Gong, X.-B. & Yao, W. Effects of substrate stiffness on mast cell migration. *Eur J Cell Biol* 100, 151178 (2021).

75. Balcioglu, H. E. *et al.* A subtle relationship between substrate stiffness and collective migration of cell clusters. *Soft Matter* 16, 1825–1839 (2020).

76. Saxena, N. *et al.* Matrix elasticity regulates mesenchymal stem cell chemotaxis. *Journal of Cell Science* jcs.211391 (2018) doi:10.1242/jcs.211391.

77. Gupta, M. *et al.* Adaptive rheology and ordering of cell cytoskeleton govern matrix rigidity sensing. *Nat Commun* 6, 7525 (2015).

78. Missirlis, D. & Spatz, J. P. Combined effects of PEG hydrogel elasticity and cell-adhesive coating on fibroblast adhesion and persistent migration. *Biomacromolecules* 15, 195–205 (2014).

79. Zhu, K. *et al.* Electric Fields at Breast Cancer and Cancer Cell Collective Galvanotaxis. *Sci Rep* 10, 8712 (2020).

80. Theveneau, E. *et al.* Collective Chemotaxis Requires Contact-Dependent Cell Polarity. *Developmental Cell* 19, 39–53 (2010).

81. Brugués, A. *et al.* Forces driving epithelial wound healing. *Nat Phys* 10, 683–690 (2014).

82. Etienne-Manneville, S. In vitro assay of primary astrocyte migration as a tool to study Rho GTPase function in cell polarization. *Methods Enzymol* 406, 565–578 (2006).

83. Zavyalova, M. V. *et al.* Intravasation as a Key Step in Cancer Metastasis. *Biochemistry (Mosc)* 84, 762–772 (2019).

84. Aceto, N. *et al.* Circulating tumor cell clusters are oligoclonal precursors of breast cancer metastasis. *Cell* 158, 1110–1122 (2014).

85. Cheung, K. J. & Ewald, A. J. A collective route to metastasis: Seeding by tumor cell clusters. *Science* 352, 167–169 (2016).

86. Bourré, L. Recapitulating Clinical Metastatic Events in Preclinical Mouse Models. *CrownBioscience; Metastasis* https://blog.crownbio.com/tumor-metastasis-models (2019).

87. Ewald, A. J., Brenot, A., Duong, M., Chan, B. S. & Werb, Z. Collective Epithelial Migration and Cell Rearrangements Drive Mammary Branching Morphogenesis. *Dev Cell* 14, 570–581 (2008).

88. Nogare, D. D. *et al.* In toto imaging of the migrating Zebrafish lateral line primordium at single cell resolution. *Dev Biol* 422, 14–23 (2017).

89. Colak-Champollion, T. Moving in concert: How lateral line primordium cells coordinate to migrate. *The Node: the community site for and by developmental and stem cell biologists* https://thenode.biologists.com/moving-in-concert-how-lateral-line-primordium-cells-coordinate-to-migrate/research/ (2019).

90. Trepat, X. *et al.* Physical forces during collective cell migration. *Nature Physics* 5, 426–430 (2009).

91. Hulpiau, P., Gul, I. S. & van Roy, F. New insights into the evolution of metazoan cadherins and catenins. *Prog Mol Biol Transl Sci* 116, 71–94 (2013).

92. Hulpiau, P. & van Roy, F. Molecular evolution of the cadherin superfamily. *Int J Biochem Cell Biol* 41, 349–369 (2009).

93. Zihni, C., Mills, C., Matter, K. & Balda, M. S. Tight junctions: from simple barriers to multifunctional molecular gates. *Nat Rev Mol Cell Biol* 17, 564–580 (2016).

94. Nielsen, M. S. *et al.* Gap Junctions. *Compr Physiol* 2, 10.1002/cphy.c110051 (2012).

95. Delva, E., Tucker, D. K. & Kowalczyk, A. P. The Desmosome. *Cold Spring Harb Perspect Biol* 1, a002543 (2009).

96. Ravasio, A. *et al.* Nanoscale architecture of cadherin-based cell adhesions. *Nature Cell Biology* 19, 28 (2016).

97. Niessen, C. M., Leckband, D. & Yap, A. S. Tissue organization by cadherin adhesion molecules: dynamic molecular and cellular mechanisms of morphogenetic regulation. *Physiol Rev* 91, 691–731 (2011).

98. Huveneers, S. *et al.* Vinculin associates with endothelial VE-cadherin junctions to control force-dependent remodeling. *J Cell Biol* 196, 641–652 (2012).

99. Huveneers, S. & de Rooij, J. Mechanosensitive systems at the cadherin–F-actin interface. *Journal of Cell Science* jcs.109447 (2013) doi:10.1242/jcs.109447.

100. Smutny, M. *et al.* Myosin II isoforms identify distinct functional modules that support integrity of the epithelial zonula adherens. *Nat Cell Biol* 12, 696–702 (2010).

101. le Duc, Q. *et al.* Vinculin potentiates E-cadherin mechanosensing and is recruited to actin-anchored sites within adherens junctions in a myosin II–dependent manner. *Journal of Cell Biology* 189, 1107–1115 (2010).

102. Yao, M. *et al.* Force-dependent conformational switch of α-catenin controls vinculin binding. *Nat Commun* 5, 4525 (2014).

103. Padmanaban, V. *et al.* E-cadherin is required for metastasis in multiple models of breast cancer. *Nature* 573, 439–444 (2019).

104. Lecuit, T. & Yap, A. S. E-cadherin junctions as active mechanical integrators in tissue dynamics. *Nat Cell Biol* 17, 533–539 (2015).

105. Zaidel-Bar, R. Cadherin adhesome at a glance. *Journal of Cell Science* 126, 373–378 (2013).

106. van Roy, F. & Berx, G. The cell-cell adhesion molecule E-cadherin. *Cell Mol Life Sci* 65, 3756–3788 (2008).

107. Buckley, C. D. *et al.* The minimal cadherin-catenin complex binds to actin filaments under force. *Science* 346, 1254211 (2014).

108. Barry, A. K. *et al.* α-Catenin cytomechanics – role in cadherin-dependent adhesion and mechanotransduction. *J Cell Sci* 127, 1779–1791 (2014).

109. Labernadie, A. *et al.* A mechanically active heterotypic E-cadherin/N-cadherin adhesion enables fibroblasts to drive cancer cell invasion. *Nat Cell Biol* 19, 224–237 (2017).

110. Prakasam, A. K., Maruthamuthu, V. & Leckband, D. E. Similarities between heterophilic and homophilic cadherin adhesion. *PNAS* 103, 15434–15439 (2006).

111. Sivasankar, S. Tuning the kinetics of cadherin adhesion. *J Invest Dermatol* 133, 2318–2323 (2013).

112. Rakshit, S., Zhang, Y., Manibog, K., Shafraz, O. & Sivasankar, S. Ideal, catch, and slip bonds in cadherin adhesion. *PNAS* 109, 18815–18820 (2012).

113. Fichtner, D. *et al.* Covalent and Density-Controlled Surface Immobilization of E-Cadherin for Adhesion Force Spectroscopy. *PLoS ONE* 9, e93123 (2014).

114. Kourtidis, A., Ngok, S. P. & Anastasiadis, P. Z. p120 catenin: an essential regulator of cadherin stability, adhesion-induced signaling, and cancer progression. *Prog Mol Biol Transl Sci* 116, 409–432 (2013).

115. Matsuzawa, K., Himoto, T., Mochizuki, Y. & Ikenouchi, J. α-Catenin Controls the Anisotropy of Force Distribution at Cell-Cell Junctions during Collective Cell Migration. *Cell Rep* 23, 3447–3456 (2018).

116. Am, S. *et al.* Myosin 2 is a key Rho kinase target necessary for the local concentration of E-cadherin at cell-cell contacts. *Molecular biology of the cell* 16, (2005).

117. Pérez-González, C. *et al.* Active wetting of epithelial tissues. *Nat Phys* 15, 79–88 (2019).

118. Borghi, N. *et al.* E-cadherin is under constitutive actomyosin-generated tension that is increased at cell–cell contacts upon externally applied stretch. *PNAS* 109, 12568–12573 (2012).

119. Collins, C., Denisin, A. K., Pruitt, B. L. & Nelson, W. J. Changes in E-cadherin rigidity sensing regulate cell adhesion. *PNAS* 114, E5835–E5844 (2017).

120. Rangarajan, E. S. & Izard, T. The Cytoskeletal Protein α-Catenin Unfurls upon Binding to Vinculin. *Journal of Biological Chemistry* 287, 18492–18499 (2012).

121. Di Russo, J., Young, J. L., Balakrishnan, A., Benk, A. S. & Spatz, J. P. NTA-Co3+-His6 versus NTA-Ni2+-His6 mediated E-Cadherin surface immobilization enhances cellular traction. *Biomaterials* 192, 171–178 (2019).

122. Chevalier, S. *et al.* Creating Biomimetic Surfaces through Covalent and Oriented Binding of Proteins. *Langmuir* 26, 14707–14715 (2010).

123. Lambert, M., Padilla, F. & Mege, R. M. Immobilized dimers of N-cadherin-Fc chimera mimic cadherin-mediated cell contact formation: contribution of both outside-in and inside-out signals. *J Cell Sci* 113, 2207–2219 (2000).

124. Vega L, J. C. M. *et al.* Recapitulating cell-cell adhesion using N-cadherin biologically tethered to substrates. *Biomacromolecules* 15, 2172–2179 (2014).

125. Tabdili, H. *et al.* Cadherin-dependent mechanotransduction depends on ligand identity but not affinity. *J Cell Sci* 125, 4362–4371 (2012).

126. Schulze, K. D. *et al.* Elastic modulus and hydraulic permeability of MDCK monolayers. *Journal of Biomechanics* 53, 210–213 (2017).

127. Ganz, A. *et al.* Traction forces exerted through N-cadherin contacts. *Biology of the Cell* 98, 721–730 (2006).

128. Amschler, K. *et al.* Morphological Plasticity of Human Melanoma Cells Is Determined by Nanoscopic Patterns of E- and N-Cadherin Interactions. *J Invest Dermatol* 139, 562–572 (2019).

129. Bays, J. L. & DeMali, K. A. Vinculin in cell–cell and cell–matrix adhesions. *Cell Mol Life Sci* 74, 2999–3009 (2017).

130. Maruthamuthu, V., Sabass, B., Schwarz, U. S. & Gardel, M. L. Cell-ECM traction force modulates endogenous tension at cell–cell contacts. *PNAS* 108, 4708–4713 (2011).

131. Ng, M. R., Besser, A., Danuser, G. & Brugge, J. S. Substrate stiffness regulates cadherin-dependent collective migration through myosin-II contractility. *J Cell Biol* 199, 545–563 (2012).

132. Mayor, R. & Etienne-Manneville, S. The front and rear of collective cell migration. *Nat Rev Mol Cell Biol* 17, 97–109 (2016).

133. Guan, L.-Y., Lv, J.-Q., Zhang, D.-Q. & Li, B. Collective Polarization of Cancer Cells at the Monolayer Boundary. *Micromachines (Basel)* 12, 112 (2021).

134. Ozawa, M. *et al.* Adherens junction regulates cryptic lamellipodia formation for epithelial cell migration. *J Cell Biol* 219, e202006196 (2020).

135. Farooqui, R. & Fenteany, G. Multiple rows of cells behind an epithelial wound edge extend cryptic lamellipodia to collectively drive cell-sheet movement. *J Cell Sci* 118, 51–63 (2005).

136. Lin, B. *et al.* Synthetic spatially graded Rac activation drives cell polarization and movement. *PNAS* (2012) doi:10.1073/pnas.1210295109.

137. Shellard, A. & Mayor, R. Supracellular migration – beyond collective cell migration. *Journal of Cell Science* 132, jcs226142 (2019).

138. Wang, H., Guo, X., Wang, X., Wang, X. & Chen, J. Supracellular Actomyosin Mediates Cell-Cell Communication and Shapes Collective Migratory Morphology. *iScience* 23, 101204 (2020).

139. Hoj, J. P. *et al.* Cellular contractility changes are sufficient to drive epithelial scattering. *Experimental Cell Research* 326, 187–200 (2014).

140. Malet-Engra, G. *et al.* Collective cell motility promotes chemotactic prowess and resistance to chemorepulsion. *Curr Biol* 25, 242–250 (2015).

141. Barriga, E. H., Franze, K., Charras, G. & Mayor, R. Tissue stiffening coordinates morphogenesis by triggering collective cell migration *in vivo*. *Nature* (2018) doi:10.1038/nature25742.

142. Morita, H. *et al.* The Physical Basis of Coordinated Tissue Spreading in Zebrafish Gastrulation. *Dev Cell* 40, 354-366.e4 (2017).

143. Beaune, G. *et al.* Spontaneous migration of cellular aggregates from giant keratocytes to running spheroids. *Proc Natl Acad Sci U S A* 115, 12926–12931 (2018).

144. Alert, R. & Trepat, X. Physical Models of Collective Cell Migration. *Annual Review of Condensed Matter Physics* 11, 77–101 (2020).

145. Pi-Jaumà, I., Alert, R. & Casademunt, J. Collective durotaxis of cohesive cell clusters on a stiffness gradient. *arXiv:2110.14316 [cond-mat, physics:physics, q-bio]* (2021).

146. Earl H. Herrick. Mechanism of movement of epidermis, especially its melanophores, in wound healing, and behavior of skin grafts in frog tadpoles. *Biol. Bull.* 63:271-286 (1932).

147. S. J. Holmes. Literature for 1913 on the behavior of the lower invertebrates. *Journal of Animal Behavior* 4, 17:281-295 (1914).

148. Cavagna, A. & Giardina, I. Bird Flocks as Condensed Matter. *Annual Review of Condensed Matter Physics* 5, 183–207 (2014).

149. Mizuno, D., Tardin, C., Schmidt, C. F. & Mackintosh, F. C. Nonequilibrium mechanics of active cytoskeletal networks. *Science* 315, 370–373 (2007).

150. Kruse, K., Joanny, J. F., Jülicher, F., Prost, J. & Sekimoto, K. Generic theory of active polar gels: a paradigm for cytoskeletal dynamics. *Eur Phys J E Soft Matter* 16, 5–16 (2005).

151. Julicher, F., Kruse, K., Prost, J. & Joanny, J. Active behavior of the Cytoskeleton. *Physics Reports* 449, 3–28 (2007).

152. Joanny, J.-F. & Prost, J. Active gels as a description of the actin-myosin cytoskeleton. *HFSP J* 3, 94–104 (2009).

153. Ladoux, B. & Mège, R.-M. Mechanobiology of collective cell behaviours. *Nat Rev Mol Cell Biol* 18, 743–757 (2017).

154. Zorn, M. L., Marel, A.-K., Segerer, F. J. & Rädler, J. O. Phenomenological approaches to collective behavior in epithelial cell migration. *Biochim Biophys Acta* 1853, 3143–3152 (2015).

155. Angelini, T. E. *et al.* Glass-like dynamics of collective cell migration. *Proc Natl Acad Sci U S A* 108, 4714–4719 (2011).

156. P. L. Townes, J. Holfreter. *Directed movements and selective adhesion of embryonic amphibian cells*. (1955).

157. Douezan, S. *et al.* Spreading dynamics and wetting transition of cellular aggregates. *Proceedings of the National Academy of Sciences of the United States of America* 108, 7315–7320 (2011).

158. Douezan, S., Dumond, J. & Brochard-Wyart, F. Wetting transitions of cellular aggregates induced by substrate rigidity. *Soft Matter* 8, 4578–4583 (2012).

159. Cousin, H. Cadherins function during the collective cell migration of Xenopus Cranial Neural Crest cells: revisiting the role of E-cadherin. *Mech Dev* 148, 79–88 (2017).

160. Aalto, A., Olguin-Olguin, A., Raz, E. Zebrafish Primordial Germ Cell Migration. *Front Cell Dev Biol.* 2021; 9: 684460 (2021).

161. Dai, W. *et al.* Tissue topography steers migrating Drosophila border cells. *Science* 370, 987–990 (2020).

162. Babb, S. G. & Marrs, J. A. E-cadherin regulates cell movements and tissue formation in early zebrafish embryos. *Dev Dyn* 230, 263–277 (2004).

163. Shimizu, T. *et al.* E-cadherin is required for gastrulation cell movements in zebrafish. *Mech Dev* 122, 747–763 (2005).

164. Duguay, D., Foty, R. A. & Steinberg, M. S. Cadherin-mediated cell adhesion and tissue segregation: qualitative and quantitative determinants. *Dev Biol* 253, 309–323 (2003).

165. Na, T.-Y., Schecterson, L., Mendonsa, A. M. & Gumbiner, B. M. The functional activity of E-cadherin controls tumor cell metastasis at multiple steps. *PNAS* 117, 5931–5937 (2020).

166. Bedard, P. L., Hansen, A. R., Ratain, M. J. & Siu, L. L. Tumour heterogeneity in the clinic. *Nature* 501, 355–364 (2013).

167. Chardès, C., Clement, R., Blanc, O. & Lenne, P.-F. Probing Cell Mechanics with Bead-Free Optical Tweezers in the Drosophila Embryo. *J Vis Exp* (2018) doi:10.3791/57900.

168. Tiscornia, G., Singer, O. & Verma, I. M. Production and purification of lentiviral vectors. *Nature Protocols* 1, 241–245 (2006).

169. Gräslund, S. *et al.* Protein production and purification. *Nature Methods* 5, 135–146 (2008).

170. Sunyer, R. *et al.* Collective cell durotaxis emerges from long-range intercellular force transmission. *Science* 353, 1157 (2016).

171. Sunyer, R., Jin, A. J., Nossal, R. & Sackett, D. L. Fabrication of Hydrogels with Steep Stiffness Gradients for Studying Cell Mechanical Response. *PLoS ONE* 7, e46107 (2012).

172. Chevalier, S. *et al.* Creating Biomimetic Surfaces through Covalent and Oriented Binding of Proteins. *Langmuir* 26, 14707–14715 (2010).

173. Trepat, X. *et al.* Physical forces during collective cell migration. *Nature Physics* 5, 426–430 (2009).

174. Rico, F. *et al.* Probing mechanical properties of living cells by atomic force microscopy with blunted pyramidal cantilever tips. *Physical Review E* 72, 021914 (2005).

175. Alcaraz, J. *et al.* Microrheology of Human Lung Epithelial Cells Measured by Atomic Force Microscopy. *Biophysical Journal* 84, 2071–2079 (2003).

176. Blanch-Mercader, C. *et al.* Effective viscosity and dynamics of spreading epithelia: a solvable model. *Soft Matter* 13, 1235–1243 (2017).

177. Saez, A. *et al.* Traction forces exerted by epithelial cell sheets. *J Phys Condens Matter* 22, 194119 (2010).

178. Trichet, L. *et al.* Evidence of a large-scale mechanosensing mechanism for cellular adaptation to substrate stiffness. *PNAS* 109, 6933–6938 (2012).

179. Walcott, S. & Sun, S. X. A mechanical model of actin stress fiber formation and substrate elasticity sensing in adherent cells. *PNAS* 107, 7757–7762 (2010).

180. Sens, P. Rigidity sensing by stochastic sliding friction. *EPL* 104, 38003 (2013).

181. Marcq, P., Yoshinaga, N. & Prost, J. Rigidity sensing explained by active matter theory. *Biophys J* 101, L33-35 (2011).

182. Guevorkian, K., Colbert, M.-J., Durth, M., Dufour, S. & Brochard-Wyart, F. Aspiration of biological viscoelastic drops. *Phys Rev Lett* 104, 218101 (2010).

183. Guevorkian, K., Gonzalez-Rodriguez, D., Carlier, C., Dufour, S. & Brochard-Wyart, F. Mechanosensitive shivering of model tissues under controlled aspiration. *PNAS* 108, 13387–13392 (2011).

184. Alencar, A. M. *et al.* Non-Equilibrium Cytoquake Dynamics in Cytoskeletal Remodeling and Stabilization. *Soft Matter* 12, 8506–8511 (2016).

185. Richardson, B. E. & Lehmann, R. Mechanisms guiding primordial germ cell migration: strategies from different organisms. *Nat Rev Mol Cell Biol* 11, 37–49 (2010).

186. Vilhena, J. G., Ortega, M., Uhlig, M. R., Garcia, R. & Pérez, R. Practical Guide to Single-Protein AFM Nanomechanical Spectroscopy Mapping: Insights and Pitfalls As Unraveled by All-Atom MD Simulations on Immunoglobulin G. *ACS Sens.* 6, 553–564 (2021).

187. EMBL-EBI Ontology Search, EFO_0006268. (2021).

188. Douezan, S., Dumond, J. & Brochard-Wyart, F. Wetting transitions of cellular aggregates induced by substrate rigidity. (2012) doi:10.1039/C2SM07418D.

189. Al-Rekabi, Z. *et al.* Hyaluronan-CD44 interactions mediate contractility and migration in periodontal ligament cells. *Cell Adh Migr* 13, 138–150 (2019).

190. Gavara, N. *et al.* Thrombin-induced contraction in alveolar epithelial cells probed by traction microscopy. *J Appl Physiol (1985)* 101, 512–520 (2006).

191. Stricker, J., Beckham, Y., Davidson, M. W. & Gardel, M. L. Myosin II-mediated focal adhesion maturation is tension insensitive. *PLoS One* 8, e70652 (2013).

192. Yamada, S. & Nelson, W. J. Localized zones of Rho and Rac activities drive initiation and expansion of epithelial cell–cell adhesion. *The Journal of Cell Biology* 178, 517–527 (2007).

193. Gupta, S. *et al.* Enhanced RhoA signalling stabilizes E-cadherin in migrating epithelial monolayers. *J Cell Sci* 134, jcs258767 (2021).

194. Acharya, B. R. *et al.* A Mechanosensitive RhoA Pathway that Protects Epithelia against Acute Tensile Stress. *Dev Cell* 47, 439-452.e6 (2018).

195. Sunyer, R. *et al.* Collective cell durotaxis emerges from long-range intercellular force transmission. *Science* 353, 1157 (2016).

196. Friedl, P. & Gilmour, D. Collective cell migration in morphogenesis, regeneration and cancer. *Nat Rev Mol Cell Biol* 10, 445–457 (2009).

197. Wallmeyer, B., Trinschek, S., Yigit, S., Thiele, U. & Betz, T. Collective Cell Migration in Embryogenesis Follows the Laws of Wetting. *Biophys J* 114, 213–222 (2018).

198. Hynes, R. O. Metastatic Potential: Generic Predisposition of the Primary Tumor or Rare, Metastatic Variants—Or Both? *Cell* 113, 821–823 (2003).

199. D. Mutluay. Expression of e-cadherin in early mouse embryo development. *JOURNAL OF THE TURKISH VETERINARY MEDICAL SOCIETY* (2020) doi:10.33188/vetheder.579594.

200. Nose, A. & Takeichi, M. A novel cadherin cell adhesion molecule: its expression patterns associated with implantation and organogenesis of mouse embryos. *Journal of Cell Biology* 103, 2649–2658 (1986).

201. Kong, D. & Großhans, J. Planar Cell Polarity and E-Cadherin in Tissue-Scale Shape Changes in Drosophila Embryos. *Frontiers in Cell and Developmental Biology* 8, 1710 (2020).

202. Pullan, J. E. & Budh, D. P. Primary Bone Cancer. in *StatPearls* (StatPearls Publishing, 2021).

203. Macedo, F. *et al.* Bone Metastases: An Overview. *Oncol Rev* 11, 321 (2017).

204. Weber, G. F., Bjerke, M. A. & DeSimone, D. W. A mechanoresponsive cadherin-keratin complex directs polarized protrusive behavior and collective cell migration. *Dev Cell* 22, 104–115 (2012).

205. Smeets, B. *et al.* Emergent structures and dynamics of cell colonies by contact inhibition of locomotion. *PNAS* 113, 14621–14626 (2016).

206. P.-G. De Gennes and J. Prost. *The Physics of Liquid Crystals*. (Univ Press, 1993).

207. Prost, J., Jülicher, F. & Joanny, J.-F. Active gel physics. *Nature Phys* 11, 111–117 (2015).

208. Marchetti, M. C. *et al.* Hydrodynamics of soft active matter. *Rev. Mod. Phys.* 85, 1143–1189 (2013).